WAVE HINDCAST SENSITIVITY TO WIND FORCING

by

SANDRA LEELLA MARGARET HODGINS

B.A.Sc., University of Waterloo, 1970

A THESIS SUBMITTED IN PARTIAL FULFILLMENT OF

THE REQUIREMENTS FOR THE DEGREE OF

MASTER OF APPLIED SCIENCE

in

THE FACULTY OF GRADUATE STUDIES

DEPARTMENT OF CIVIL ENGINEERING

We accept this thesis as conforming

to the required standard

THE UNIVERSITY OF BRITISH COLUMBIA

October 1986

In presenting this thesis in partial fulfillment of the requirements of an advanced degree at THE UNIVERSITY OF BRITISH COLUMBIA, I agree that the Library shall make it freely available for reference and study. I further agree that permission for extensive copying of this thesis for scholarly purposes may be granted by the Head of my Department or by his or her representatives. It is understood that copying or publication of this thesis for financial gain shall not be allowed without my written permission.

Department of Civil Engineering

THE UNIVERSITY OF BRITISH COLUMBIA
2075 Wesbrook Place
Vancouver, Canada
V6T 1W5

Date: October 1986

Abstract

Efficient planning and safe operation of marine vessels and coastal structures
require good understanding of wave properties, usually expressed in
statistical terms. In the absence of very long direct measurement records,
spectral wave hindcasting is routinely used to derive design and operating
criteria. The method involves solution of a time-dependent energy balance
equation including spatial propagation, growth due to local wind, non-linear
transfers between frequency components and dissipation processes. The most
important source of errors in a careful hindcast is the input wind which is
normally derived from historical surface pressure data. Since spectral wave
models generate a sea-state that is almost in balance with local winds, wind
sea is largely independent of the preceding storm history. Swell energy, on
the other hand, propagates freely at off-wind angles perpetuating any errors
that occurred in its generation. Shallow water near-shore zones are usually
modelled with a small-area, nested subgrid that receives boundary data from
the surrounding large-area model. Since the wave energy solution within the
submodel can be dominated by the boundary conditions, errors in the large-area
model must be minimized.

The purpose of this study was to investigate the sensitivity of hindcast wave
fields to prescribed errors in the evolution of the wind patterns. Using a
radially symmetric model of surface pressure, five parameters were used to
define storm evolution: storm trajectory, minimum central low pressure, rate
of storm intensification, advection rate and storm size. Sensitivity analyses
of each parameter were used to obtain the likely maximum attributable
variation in the significant wave height field. On this basis, and
considering wind sea only, the three most important parameters are (1)
trajectory, (2) minimum central pressure and (3) advection rate. With careful
wind field re-construction, wave hindcasts of specific events can be performed
to acceptable engineering standards for extreme value analysis. However, for
the present, climatological (continuous multi-year) wave databases constructed
by spectral hindcasting will be too inaccurate to warrant their cost. The
most promising advance for wave hindcasting (and forecasting) is the
possibility of acquiring high-resolution wind and wave data with satellite
sensors to eliminate the need for inherently inaccurate surface pressure data.

Table of Contents

Table of Contents
(Continued)

List of Tables

List of Figures

List of Figures
(Continued)

List of Figures

(Continued)

List of Figures

(Continued)

List of Figures

(Continued)

List of Figures

(Continued)

Acknowledgement

1.0 INTRODUCTION

Every year between October and March the British Columbia coastline (Fig. 1.1) comes under the influence of one or more severe northeast Pacific Ocean storms (Lewis and Moran, 1985). Some of these low pressure systems move directly inland, typically within a broad band between northern Vancouver Island and the Queen Charlotte Islands. More commonly, the trajectory shifts to the north, well offshore, and enters the Gulf of Alaska. Each of these events has the potential to seriously impact on some aspect of marine activity along the coast: international shipping, fishing, barge traffic, log booming or offshore resource development schemes. Between 1957 and 1983, Lewis and Moran report that eight ships are known to have sunk with as many as 60 crew members aboard, and about the same number of vessels have suffered extensive damage in these storms. The rarer reports of coastal property damage are usually attributed directly to the winds, although occasionally wave damage has occurred as in February 1979 when a section of a floating bridge on Hood Canal (Washington) was washed away.

The severity of the local sea-state was highlighted again in October of 1984 when six fishing vessels and four crewmembers were lost off the northwest coast of Vancouver Island during a severe storm. This event led to a Commission of Enquiry (LeBlond, 1984) recommending improvements in weather and sea-state forecasting for B.C. coastal waters.

For engineering purposes, the data resources for sea-state specification on the west coast of Canada are very meagre. There is a semi-permanent non-directional wave measuring station at Tofino on the west coast of Vancouver Island (Fig. 1.1). A Waverider buoy has been positioned and maintained here since June 1970 by the Marine Environmental Data Service (MEDS) of the Department of Fisheries and Oceans. The utility of these data is quite limited since the buoy is located close to the coast in relatively shallow water (40 m), and prior to January 1981 these data were generally of poor quality (MEDS, 1984).

Between October 1982 and May 1984 MEDS sponsored a major wave climate study of the northern British Columbia coast (Seakem, 1985; Hodgins et al., 1985). Six wave buoys were deployed in Queen Charlotte Sound, Hecate Strait and Dixon Entrance at the locations shown in Fig 1.1. Reliable directional data were obtained only at the McInnes Island site. This program of data collection was continued through May 1985 under the support of the Environmental Studies Revolving Fund (ESRF) and will be reported by Dobrocky Seatech (1986).

GULF OF ALASKA

BRITISH
COLUMBIA

QUEEN
CHARLOTTE
ISLANDS

HECATE
STRAIT

McINNES
ISLAND

QUEEN
CHARLOTTE
SOUND

VANCOUVER
ISLAND

TOFINO

PACIFIC OCEAN

● Wave Monitoring
Stations

55

45

160

150

140

130

- 2 -
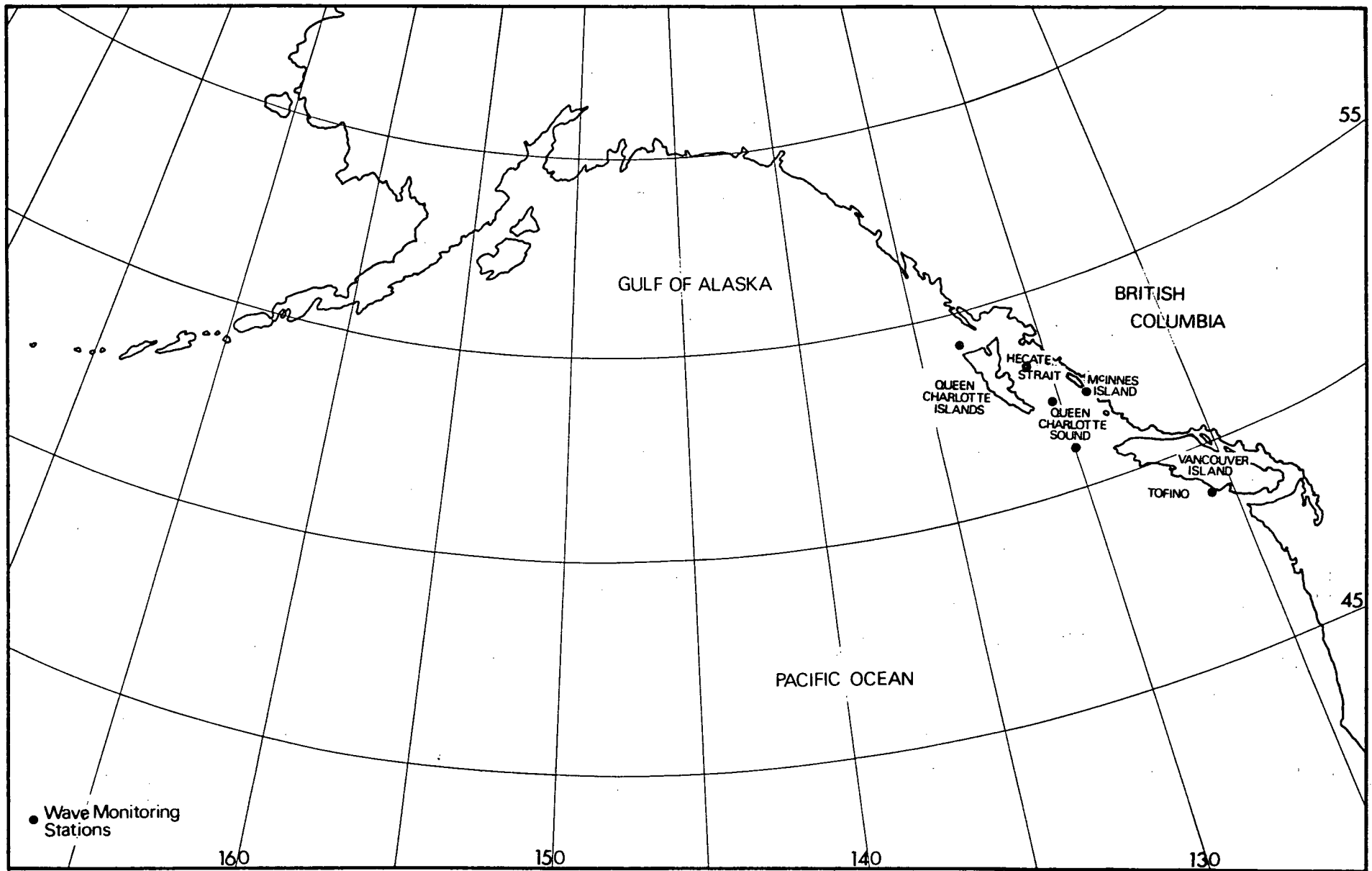
Fig. 1.1   The west coast of Canada showing the major landform
features as well as wave monitoring stations.

The wave climate at most of these sites is strongly influenced by adjacent landforms and by bathymetric relief. As a result, even the few months of data that are available have limited regional applicability to the designer of a particular coastal structure or harbour facility. This limitation is a common problem in most maritime locations that is traditionally overcome by wave hindcasting. This approach is possible because the data archives of winds (or surface pressure fields from which wind maps can be derived) extend for many years over large regions of the globe and because the physical mechanisms governing sea-state evolution by wind forcing are sufficiently well-known.

To gain an impression of how waves usually appear in the ocean, a contour plot of one stereo pair of aerial images is shown in Fig. 1.2. This plot, in which the white areas are wave crests and the dark areas troughs, was drawn from a regular 90 by 60 point grid of spot wave heights derived from the stereo images. The waves shown here were in the generation area with a mean over-water wind of 18 knots from 330°T at the time of the photographs. There is a discernible alignment of the crests implying a mean direction of propagation at about 30° to the right of the wind vector. Superimposed on this average pattern is a great deal of fine structure (down to about 20 m in length) which can be interpreted as the superposition of a large number of wave patterns of different wave lengths travelling at different angles to the wind.

If the range of angles associated with the individual wave patterns is wide, then the overall wave pattern appears disordered (as in Fig. 1.2), and the wind waves are short-crested with the length along a crest only a few times the dominant wave length. It is only after waves have propagated away from the active generation area that they become sorted out into long-crested swell waves.

The variability illustrated in Fig. 1.2 does not have any practical significance for most coastal engineering applications. The typical approach is to describe such an ensemble of waves by a single characteristic wave height (such as significant wave height, H_s), wave period and (if possible) direction; in this manner a reliable statistical representation of the sea-state is developed over time from which normal and extreme design conditions may be derived.

The vast majority of wave data collected are not spatial snapshots like Fig. 1.2, but are time-series of sea surface elevation (and perhaps tilt) at a fixed point. Such data are routinely and conveniently analyzed in the
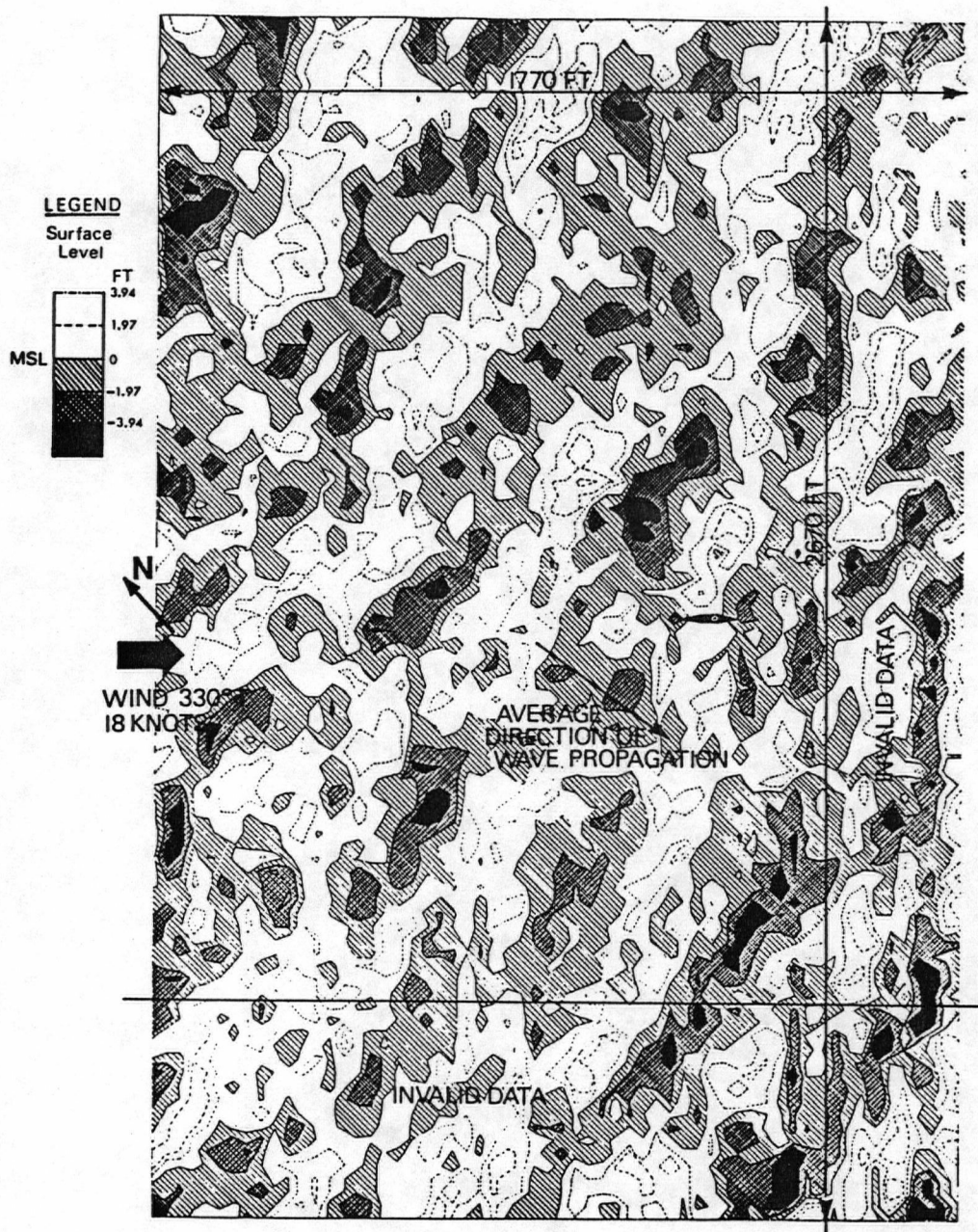
Fig. 1.2   Levelled contour analysis of the ocean surface. Contour
           interval 0.2 mm, where 0.1016 mm = 1 foot. Shaded areas
           are below mean sea level and clear areas are above sea
           level. (From Coté et al., 1960)

frequency domain by Fourier transforming the time domain signal. This results in a distribution of wave energy E as a function of frequency f which is called a variance (or energy or power) spectrum. Generally one spectrum can be calculated with confidence from about 20 min of data sampled at about 2 to 4 Hz. If tilt is also measured, a directional energy spectrum $F(f,\theta)$ can be calculated. A sample measured directional spectrum is shown in Fig. 1.3 as $F(f,\theta)$ and, by integrating over direction, as $E(f)$. This illustration shows a sea state dominated by waves with periods of 9 to 11 s. The wave frequency component with the peak energy content (f_p) is travelling to the north, and the mean direction at all frequencies is also to the north.

The primary product of wave hindcasting is a spatial and temporal array of energy spectra $F(f,\theta)$ (of which Fig. 1.3 is a typical single element). The most useful secondary product is the equivalent array of significant wave height which is readily obtained by integration of $F(f,\theta)$ over frequency and direction. Fig. 1.4 from a recent B.C. coastal hindcast study (Hodgins and Nikleva, 1986) shows a contour map of H_s which is a space plane of this secondary data array at a particular time. A time-series of such plots depicts the best estimate of regional sea-state evolution that can normally be obtained. Traditional time-series of H_s at particular points are readily extracted by spatial interpolation.

Such wave height fields contain errors, some of which may be inherent in the wave model: inaccurate calibration of wave growth coefficients, inadequate resolution of bathymetric and landform features, inaccurate wave propagation schemes, omission of important wave frequencies, omission of physical processes associated with wave-wave interactions and whitecaping. The effects of each of these potential problems can be minimized by careful problem definition and a thorough model calibration and verification stage prior to production hindcasting.

Nevertheless, the most serious source of error in hindcast wave fields will usually be in the forcing wind data, and several recent studies have begun to address the characteristics of these errors. Statistical assessments of wind fields produced by the operational numerical weather prediction (NWP) models of the Canadian Meteorological Centre (CMC) have been reported by Hodgins and Nikleva (1986), Hodgins and Hodgins (1986) and MacLaren Plansearch (1985). Cardone et al. (1980) have conducted a similar study of U.S. meteorological data.
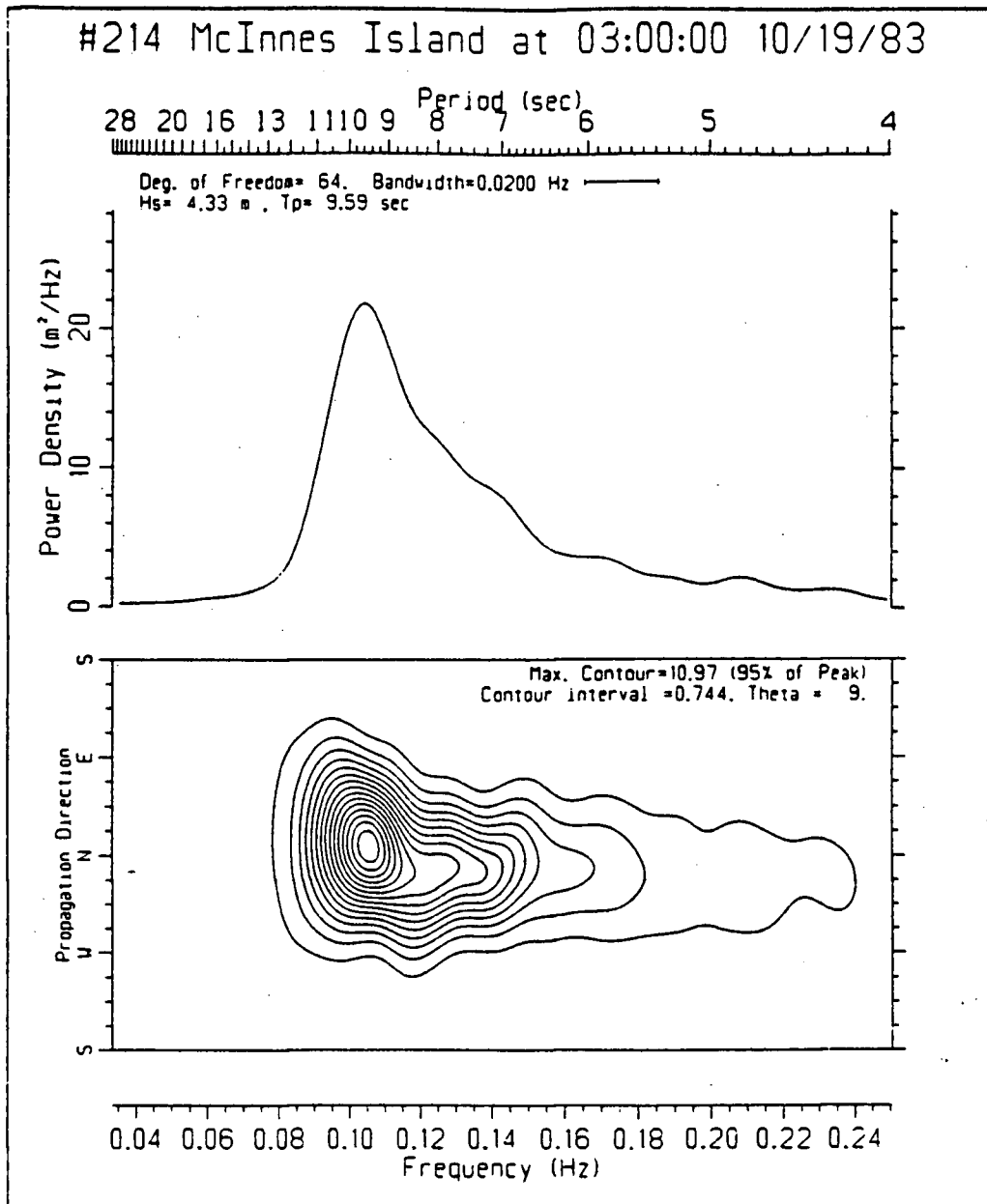
Fig. 1.3   A directional wave spectrum calculated from data
measured off the west coast of Canada. The presentation
is F(f,θ) in the lower panel and E(f) directly above on
the same frequency scale. (From Hodgins et al., 1985)
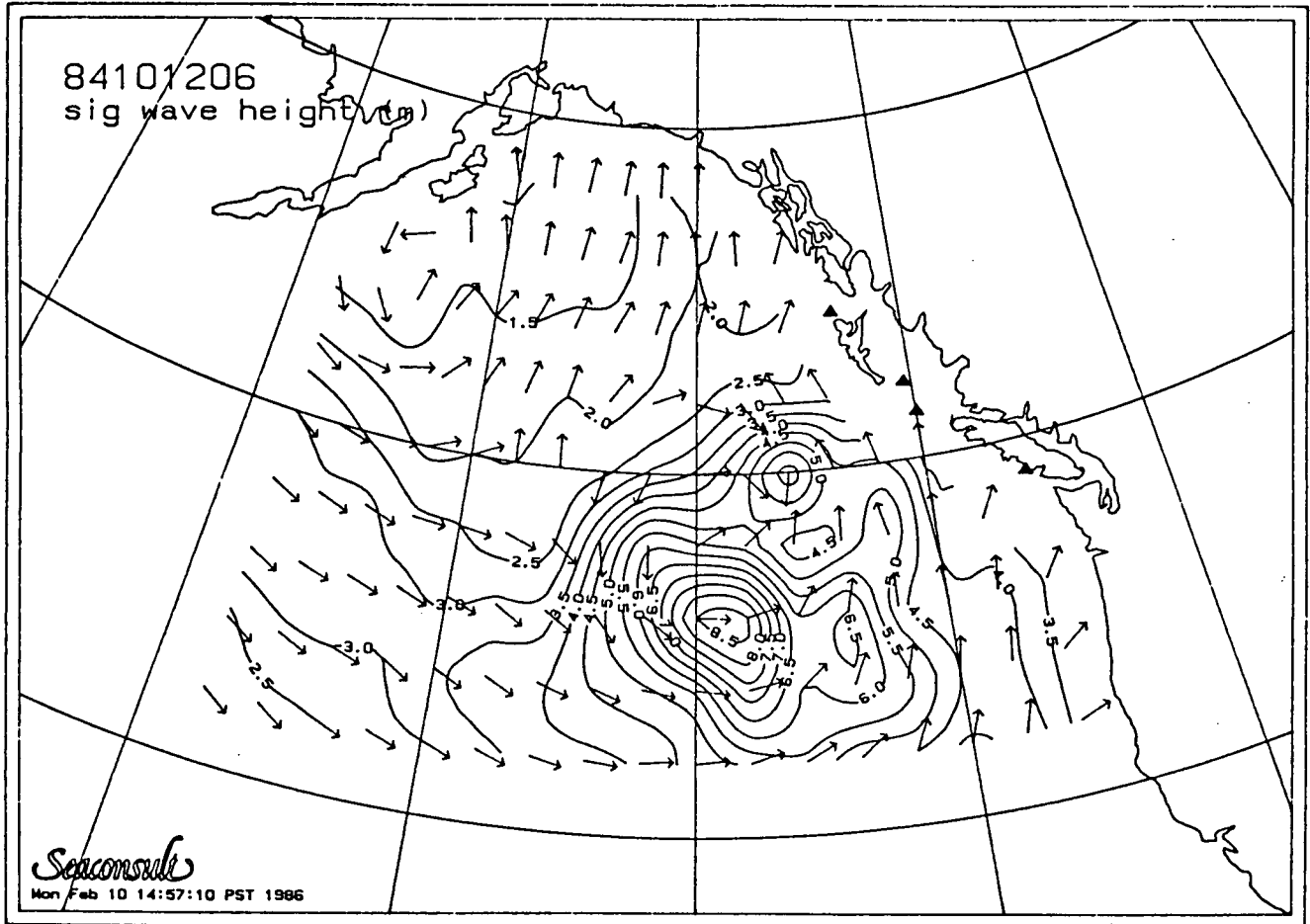
Fig. 1.4   A contour map of significant wave height as hindcast for
            the west coast of British Columbia. (From Hodgins and
            Nikleva, 1986).

Hodgins and Nikleva (1986) investigated the effects on error statistics in the northeast Pacific of the CMC analysis time ("now-cast") winds, of the west coast regional surface pressure re-analysis prepared by the Pacific Weather Centre (PWC) from which the authors derived a surface wind, and of wind field kinematic analysis in which numerical model wind fields are calibrated by hand to marine observations reported by ships at sea. On average, the NWP model wind fields are improved by human intervention, most of all by input of calibration data in the kinematic analysis and to a lesser extent by the analytical experience of the regional weather forecaster. For the kinematic winds exceeding 10 knots, the reported bias is 2 to 3 knots, root-mean-square (rms) speed error is 5 to 7 knots and rms direction error is 20° to 28°.

Cardone et al. (1980) also investigated error characteristics of NE Pacific winds generated by a NWP model and kinematic wind fields, but also included "objective" wind fields in which ship-reported winds were blended by computer with the NWP model winds. These researchers found that the kinematic wind fields had consistently lower bias and rms errors than the other wind types. Bias was less than 1 knot, rms wind speed error was about 6 knots and rms direction error was 30°, including all observations irrespective of wind speed.

All of these studies were limited to statistical intercomparison of a hindcast or forecast wind with a point wind measurement, and none of them has been able to relate the error parameters to consequences for the modelled sea-state. Other investigators such as Clancey et al. (1986), Janssen et al. (1984), Golding (1983), and most other wave forecasting and hindcasting groups in Europe and North America have published similar types of statistical analyses based on wave modelling results in which wave field error is largely attributed to known or suspected wind errors. Because these comparisons are made at isolated points within complex weather systems, the opportunity to identify more specific cause-and-effect connections is unlikely.

Wave models which are currently state-of-the-art can generally hindcast sea-states to within ± 1 m in height and ± 2 s in period given sufficiently accurate input winds. Of the several sources of wind field errors, some are systematic and others are random in space or time. The purpose of this investigation is to study the effects on wave model results of a set of common systematic errors in the forcing wind input, with the end objective of identifying which of these errors have serious effects on wave model performance. By carefully controlling the structure and evolution of the forcing wind fields, variations

in the time-series of the integrated energy field (H_s) have been directly linked to the causative factors in the wind history.

Reporting of this research has been divided into two essential elements: the theory of wave modelling and the experimental application of one particular model. Chapter 2 describes the elements of the physics of sea-state evolution that may be parameterized in wave hindcast models. The heart of this discussion is the energy balance equation including energy source and sink terms, propagation and the form of energy spectra. Important peripheral considerations that are included are swell energy propagation, shallow water effects and wind parameterization.

Chapter 3 is devoted to a more specific description of three wave models that illustrate three fairly distinct approaches to solution of the total problem, that is, wave generation, propagation and dissipation in generalized geographical and bathymetric configurations. Emphasis is placed on the ADWAVE model which was used exclusively in the experimental part of this research.

The experiment was comprised of a sensitivity analysis in which the effects of systematic variations in the input wind forcing function were quantified in terms of wave energy at discrete locations in the solution domain. These effects have been interpreted as input and output error characteristics to provide a preliminary indication of the range of acceptable wind parameter errors for tolerable uncertainty in sea-state statistics. The input winds and the wave model set-up configuration are described in detail in Chapter 4, followed by discussion of the output results in Chapter 5. The conclusions drawn from this analysis are reported in Chapter 6.

2.0 SEA-STATE DESCRIPTION: THE BASIS FOR WAVE MODELLING

Virtually all wave prediction models are based on equations describing the conservation of wave energy at specified locations. The solution of this system describes the time-space evolution of wave spectra $F(f,\theta)$, such as that illustrated in Fig. 1.3, at selected points. The spectra are statistically averaged representations that are assumed to be valid for some finite period of time (on the order of 1 to 3 h) and characteristic of sea-state conditions over a discrete area (up to 2.5° of latitude and longitude).

2.1 The Energy Balance Equation

The processes that must be considered are propagation of wave energy toward and away from the point, growth due to local winds, non-linear transfer processes that redistribute energy between frequency components, and dissipation due to whitecapping and bottom friction. The energy balance describing these processes is written as

$$\frac{\partial}{\partial t} F(f,\theta) - \vec{c_g}(f) \cdot \nabla F(f,\theta) = S(f, \theta) \qquad (2.1)$$

where F is wave energy as a function of frequency (f) and direction (θ)

$\vec{c_g}$ is the wave group velocity as a function of frequency

∇ is the gradient operator $\left(\dfrac{\partial}{\partial x}, \dfrac{\partial}{\partial y}\right)$ and

S is the net energy source function.

Understanding of the physics governing the process embodied in $S(f,\theta)$ and the parameterization of it in wave models has evolved as a direct result of wave measurement experiments. The two most important studies, both started in 1968, are the Ocean Data Gathering Program (ODGP) and the Joint North Sea Wave Project (JONSWAP). ODGP was a joint oil industry program conducted between 1968 and 1971 at six locations in the Gulf of Mexico to collect oceanographic and meteorological data with emphasis on severe conditions in hurricanes. JONSWAP was an international undertaking between cooperating research institutes to determine the structure of the source terms in the energy balance equation. The latter experiment lasted 10 weeks in 1968 and 1969 with comprehensive data collection at up to 13 locations in the North Sea. The objective was to record during steady offshore winds to facilitate studying the evolution of the wave energy spectrum and thereby elucidate the physical mechanisms responsible for that evolution.

Although ODGP and JONSWAP were so different in purpose, the eventual outcome of each was an important, but again very different, advance in wind-wave

modelling. The ODGP data set allowed, for the first time, the development of a _verified_ wave model--the ODGP model by Cardone et al. (1975) which has become the basis of virtually all commercial wave forecasting in the United States. The JONSWAP experiment highlighted the importance of non-linear energy transfer processes between wave frequencies (wave-wave interaction), which are omitted from the ODGP model and its successors. Many of the European operational forecasting wave models, in addition to Hasselmann's research models (Hasselmann et al., 1976; Günther et al., 1979a,b) and Resio's (1981, 1982) hindcast model, utilize the JONSWAP results.

2.2 **Wave Model Parameterizations**

2.2.1 **Wave Directionality**

In many models equation (2.1) is integrated with respect to θ to yield the energy equation, written here in one spatial dimension (Hasselmann et al., 1976) as

$$\frac{\partial}{\partial t} E(f) + c_g(f).\frac{\partial E(f)}{\partial x} = S(f) \tag{2.2}$$

$F(f, \theta)$ can then be obtained by applying a spreading function $G(f,\theta)$ to the solution of (2.2) such that

$$F(f,\theta) = E(f).G(f,\theta) \tag{2.3}$$

where G must satisfy

$$\int_{-\pi}^{\pi} G(f, \theta)d = 1 \tag{2.4}$$

The most widely used functional forms of G are the cosine-squared (St. Denis and Pierson, 1953):

$$G(\theta) = \begin{cases} \frac{2}{\pi}\cos^2\theta, & |\theta| \leq \pi/2 \\ 0 & , \text{ otherwise} \end{cases} \tag{2.5}$$

where G is independent of wave frequency; and the cosine-power (Longuet-Higgins et al., 1961)

$$G(\theta) = C(s) \cos^{2s}\left(\frac{\theta - \bar{\theta}}{2}\right) \tag{2.6}$$

where $C(s)$ is the normalizing factor needed to ensure that (2.4) is satisfied, s is a function of frequency, and $\bar{\theta}$ is the mean wave direction. The cosine-power spreading function is shown in Fig. 2.1 for values of s between 1 and 10 and as a function of frequency. This figure shows that the largest values of
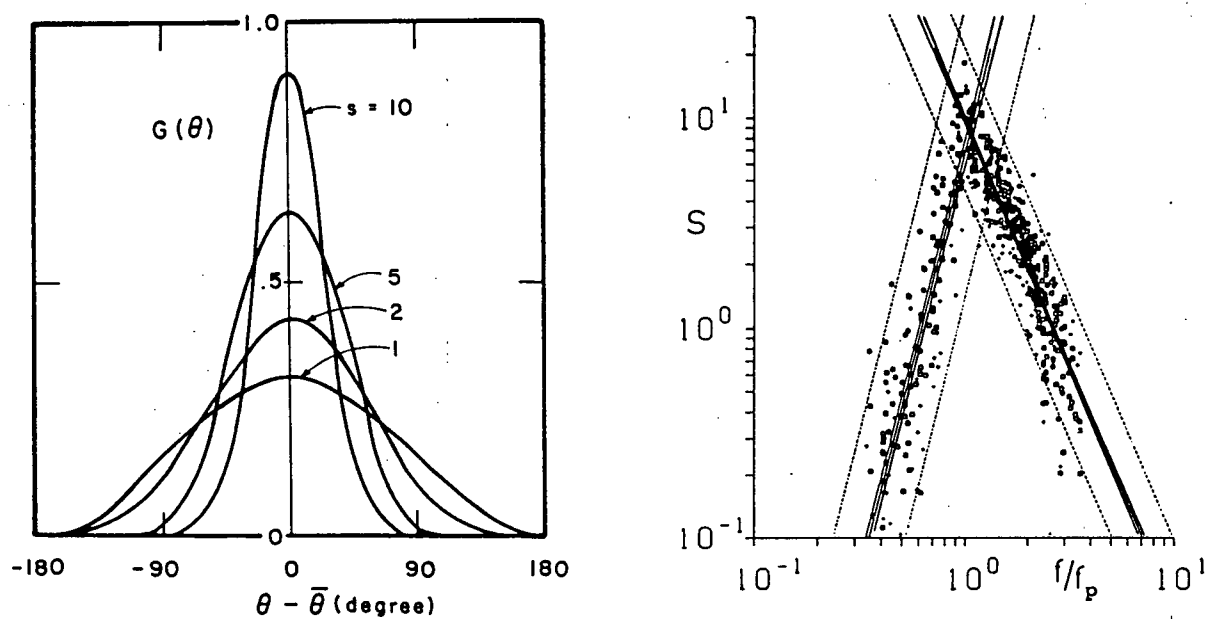
Fig. 2.1   The cosine-power spreading function. The left panel
illustrates the shape variation with s (from Sarpkaya
and Isaacson, 1981); the right panel shows the
distribution of s as a function of frequency (from
Hasselmann et al., 1980).

s, which are about 10, occur at the peak frequency and that the wave energy is well-focussed along the mean wave direction (within about $\pm 45^\circ$). At other wave frequencies the energy is more spread out around the mean direction of wave propagation.

2.2.2 The Energy Source Function

The net energy source function S which governs the input of energy to the wave field was described by Hasselmann et al. (1973) in terms of three processes:

$$S = S_{in} + S_{nl} + S_{ds} \qquad (2.7)$$

with the following meanings:

S_{in} = the input of energy from the wind

S_{nl} = the non-linear energy transfer process

S_{ds} = the energy dissipation process (whitecapping)

These processes are shown schematically in Fig. 2.2, together with the resultant net transfer curve as a function of frequency. This figure emphasizes the importance of S_{nl} which is the dominant energy input mechanism at frequencies lower than f_p. Near and just below f_p, S_{nl} and S_{in} are about balanced, but at higher frequencies S_{nl} removes more energy than S_{in} contributes. Only at very high frequencies does S_{ds} contribute to the energy balance. The net redistribution of energy is therefore from frequencies above f_p to those below on the forward face of the wave spectrum.

Of these energy source terms, only S_{nl} at present has an analytic formulation (known as the Boltzmann integral). Although this functional form of S_{nl} can be evaluated analytically, the computations are too complex to be routinely included in wave models.

In JONSWAP, the S_{nl} term was evaluated for individual test cases and combined with the data for S to examine the remaining two terms $S_{in} + S_{ds}$. The latter was assumed to account for all dissipation mechanisms, primarily whitecapping, but also for energy transfers between spectral components such as the attenuation of long waves by damped short waves (Hasselmann et al., 1973). Assuming that S_{in} has a similar distribution to the spectrum itself, in accordance with linear wave growth theories, the process model shown in Fig. 2.2 can be inferred. The partition of energy between S_{in} and S_{ds} could not, however, be derived directly from the JONSWAP data.

ENERGY BALANCE

S_{in} = Input from Atmosphere

S_{nl} = Non-linear Wave-Wave Transfer

S_{ds} = Dissipation

$E(f) \rightarrow$

S_{in}

$f \longrightarrow$

S_{ds}

S_{nl}

Net Transfer $S = S_{in} + S_{nl} + S_{ds}$

$f \longrightarrow$
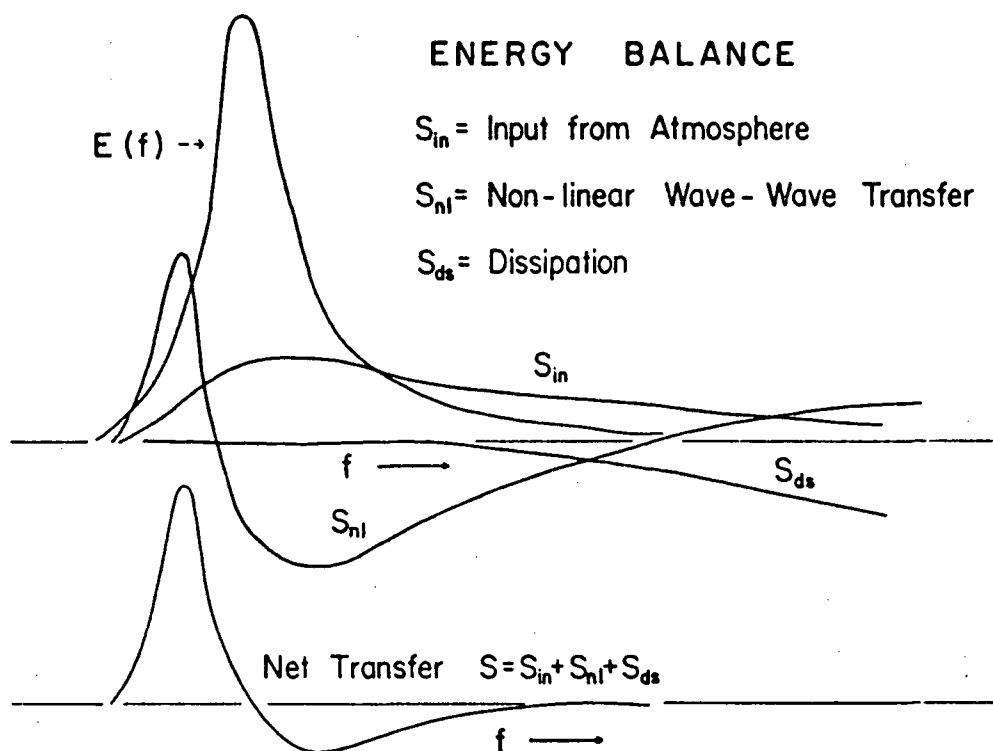
Fig. 2.2   A schematic illustration of the three energy source terms that together are responsible for the redistribution of wave energy as a function of frequency. (From Hasselmann et al., 1973)

2.2.3 The Energy Spectrum

Parametric Forms

There are two general approaches to the solution of the energy balance equation (2.1). The first method assumes that every spectrum $E(f)$ can be approximated by a universal parametric spectrum $\hat{E}(f, a_i)$. The governing parameters a_i are usually related to wind speed, peak spectral frequency, and spectral shape functions, all of which must be readily determined from data or from empirical laws.

The best-known forms of $\hat{E}$ are the Pierson-Moskowitz (PM) spectrum (Pierson and Moskowitz, 1964) for fully-developed wind seas and the JONSWAP spectrum (Hasselmann et al., 1973) which was developed by analysis of fetch-limited growing wind-sea spectra.

The PM spectrum is given by

$$\hat{E}(f) = \alpha g^2 (2\pi)^{-4} f^{-5} \exp\left[-0.74 \left(\frac{g}{2\pi U}\right)^4 / f^4\right] \tag{2.8}$$

in which α is Phillips' constant (=0.0081) and U is wind speed.

The JONSWAP parametric spectral equation is

$$\hat{E}(f) = \alpha g^2 (2\pi)^{-4} f^{-5} \exp\left(\frac{-5}{4}\left[\frac{f}{f_p}\right]^{-4}\right) \cdot \gamma^{c(f)} \tag{2.9}$$

where α = the Phillips' scaling parameter, now a function of f_p rather than a constant

    f_p = frequency at the point of maximum energy

    $\gamma^{c(f)}$ = the peak enhancement factor

    $c(f) = \exp([-(f-f_p)^2] / [2\sigma^2 f_p^2])$

    σ = the spectral shape parameter defined by σ_a (if $f < f_p$) and σ_b (if $f > f_p$)

The peak enhancement factor, which largely accounts for the difference between PM and JONSWAP forms, heightens and sharpens the spectral peak in fetch-limited seas to model the "overshoot" effect measured in JONSWAP. The term overshoot describes the observation that under steady wind conditions, the energy at and near f_p in developing seas can exceed the eventual equilibrium energy level attained at those frequencies. For $\gamma=1$, the JONSWAP equation reduces to the PM spectrum which imposes $f_p=0.14(g/U)$ and $\alpha=0.0081$. For $\gamma>1$, the maximum effect is at $f=f_p$ (since $c(f)=1$) and diminishes exponentially with increasing $|f-f_p|$. Hasselmann et al. (1976) report that most wind-sea spectra

adhere to the JONSWAP form with average parameter values of $\gamma=3.3$, $\sigma_a=0.07$ and $\sigma_b=0.09$, independent of fetch. This form of $\hat{E}$ is called the mean JONSWAP spectrum.

Discrete Forms

The second general solution technique involves the discretization of $F(f,\theta)$. The directional dependence is always divided into a number of equal sectors such that $M\Delta\theta = 2\pi$ and typical values of M are 12, 16, or 24 to give corresponding resolutions of 30°, 22.5^o, and 15°. Discretization of frequency is often done in a similar way: $N\Delta f = (f_{max}-f_{min})$, in which case f_{min} is typically 0.05 Hz (T=20 s), f_{max} is 0.2 Hz (T=5 s), and $\Delta f=0.01$ Hz. The disadvantage of this method is that the resolution of the spectrum is coarsest in the lower frequencies. In moderate and severe sea-states, most of the spectral energy will be in this poorly defined part of the spectrum. A logical alternative is to impose equal period elements: $N\Delta T = (T_{max}-T_{min})$. For the same frequency (period) limits and the same number of discrete elements, the low frequency resolution can be greatly improved as illustrated in Fig. 2.3. This means that spectral resolution can, and should, be tailored to more precisely specify the shape and peak of the spectrum in those sea-states of most importance for the modelling application.

2.3 Other Considerations

2.3.1 Wind-Sea and Swell

One important consideration in building a model of the energy balance equation (2.1) is the parameterization of locally generated wind-sea and of swell energy that propagates into the area of interest from afar. In the modelling context, a swell wave may be defined as any sea component whose phase velocity exceeds that of the local wind, since it is assumed that no atmospheric input can be absorbed under these conditions. Because these are freely propagating waves, the energy conservation equation is reduced to only an advection equation with energy source terms set to zero.

Since there is no parametric model of swell, the solution technique chosen is either a finite differencing approach (to high-order accuracy to control numerical dispersion) or the method of characteristics. Frequently the latter scheme, which is a ray tracing technique, is employed because shallow water refractive effects are readily incorporated.
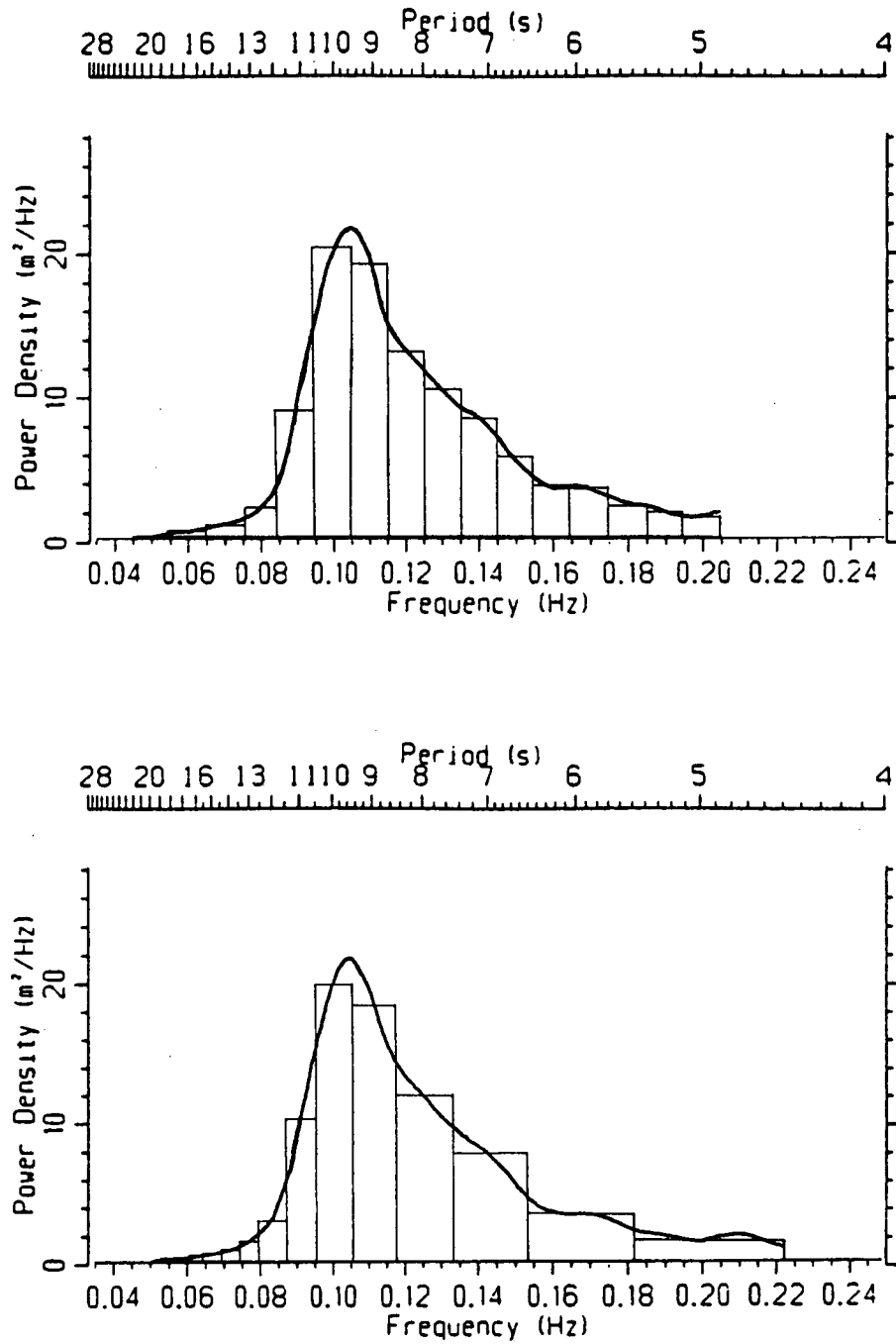
Fig. 2.3   A comparison of spectral frequency discretization in equal frequency and equal period increments for N=15, f_{min}=0.05 Hz and f_{max}=0.2 Hz.

In principle, swell energy could be input as a function of time along the wave model boundaries, but the information to do so, $F_{swell}(f,\theta)$, is not generally available. This represents a restriction on limited-area wave modelling (as contrasted with hemispheric or global ocean basin applications) since swell that would be generated by other storm systems outside the model's physical domain cannot be accounted for. In some cases this omission may cause significant errors in wave hindcast results.

The frequency of swell waves is generally low. On both the east and west coasts of Canada wave measurements can contain significant energy in the T=20 to 30 s range that is associated with the passage of intense storm systems. It is important, therefore, to resolve this frequency range if such meteorological events are to be accurately modelled. The advantage of the equal period spectral discretization (Fig. 2.3) is evident in this case.

2.3.2 Shallow Water Effects

In the interests of computational efficiency, most wave hindcasts are run as deep water approximations unless accurate near-shore sea-state conditions are required. In that event, the usual approach is to solve the deep water equations on a coarse grid whose primary domain is the deep ocean and to use these results as boundary conditions for a nested, fine-grid shallow water solution domain. An example of a nested grid arrangement is shown in Fig. 2.4 for the west coast hindcast by Seaconsult (Hodgins and Nikleva, 1986).

Physical mechanisms that may be accounted for in shallow water models are bathymetric refraction, wave shoaling, energy dissipation by bottom friction and shallow water wave breaking. Spectral refraction and shoaling models describe the evolution of wave energy along characteristic rays orthogonal to wave crests. Wave breaking is modelled by imposition of a depth-limited saturated spectral form.

A secondary beneficial effect of a fine-grid nested model is improved landform resolution to give better modelling of sheltering conditions. This can be a critical consideration in hindcasting near-shore sea-states in areas like Queen Charlotte Sound or Hecate Strait.

2.3.3 Wind Input

All wave growth models expect wind input as a time-series of near-surface speed and direction (or vector components). These winds may be derived from surface pressure data, or they may be generated by a numerical weather prediction model, and either of these may incorporate direct measurements.
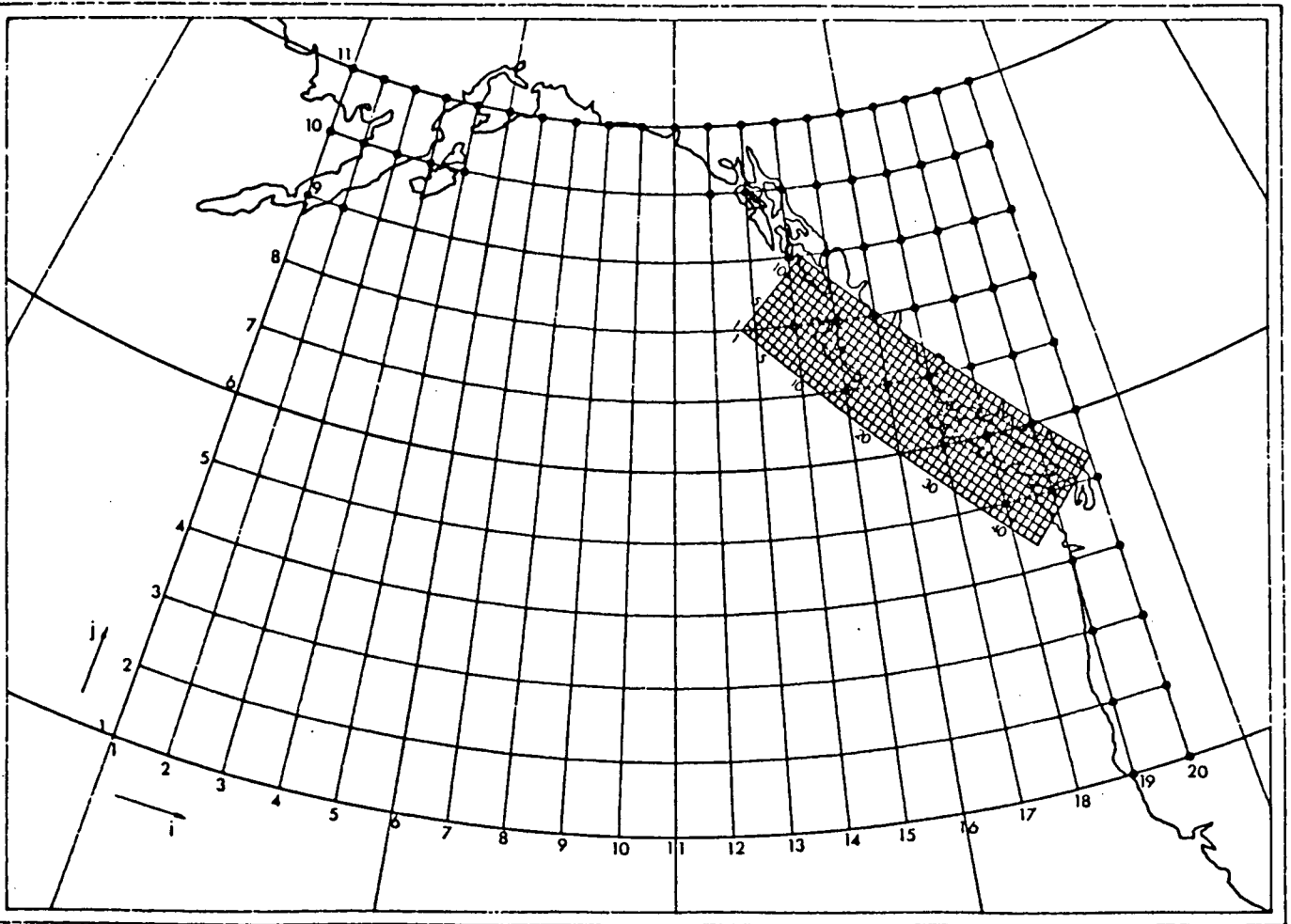
Fig. 2.4   A coarse deep water hindcast grid with a nested shallow
           water model grid as used for a hindcast of waves on the
           west coast of British Columbia.   (From Hodgins and
           Nikleva, 1986).

There are two key aspects to specification of the wind forcing term: scales of resolution (both temporal and spatial) and the actual parameterization of wind force.

Generally hindcast winds are derived from 6-hourly surface pressure charts as a gradient wind that is then reduced to a near-surface vector. This time interval implies an interpolation down to the model integration time step which is typically of the order of one hour. In the time domain, vectorial interpolation of the wind vector U is common, but may not be very accurate in rapidly turning wind fields. If pressure charts are digitized in length increments that are much less than the model grid scale and with fairly fine isobar spacing (1 to 4 mb), then spatial interpolation of the wind fields will be reasonably accurate. Attempts to use historical gridded wind fields as archived from a NWP model are usually very unsuccessful because the typically coarse spatial resolution (of the order of 400 km) is inadequate to embody the actual gradients in wind speed (and possibly direction).

Since the energy input term S_{in} is normally formulated in terms of the friction velocity at the sea surface u_*, the input wind U must be converted by the wave model to u_* as

$$u_*^2 = C_D U^2 \tag{2.10}$$

where the drag coefficient C_D is a function of U. Garratt (1977) found a general dependence of the drag coefficient on wind speed of the form

$$C_D = 0.51 \times 10^{-3} U^{0.46} \tag{2.11}$$

Thus u_* with this formulation is proportional to approximately $U^{5/4}$. There are several other formulations with different dependencies on U such as the one published by Large and Pond (1981):

$$C_D = (0.49 + 0.065U) * 10^{-3} \tag{2.12}$$

where U is the wind speed at 10 m elevation and is defined in the range $11 \leqslant U \leqslant 25$ m/s. Recently a number of these formulae have been compared by Hsu (1986) and his findings are illustrated in Fig. 2.5.

Prior to about 1970, wave model formulations may have assumed that C_D was a constant. If such a model were well-calibrated for low and moderate wind speeds, it would increasingly under-estimate wave growth as winds strengthen.
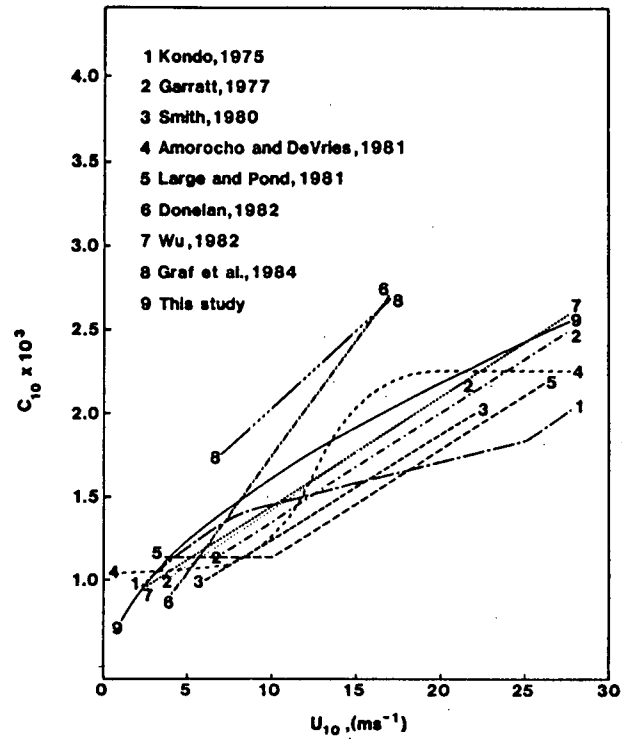
Fig. 2.5   Variations in the drag coefficient as a function of the
            10-m elevation wind speed. (From Hsu, 1986).

Because the wind vector varies with elevation above the sea surface, a given model will be calibrated to accept input at a particular reference elevation-- 10 m and 19.5 m are common standards. If wind input is only available at other than the reference level, it must first be converted by application of an atmospheric boundary layer model. The simplest of these is an empirical relationship such as

$$U_m = U_r \left(\frac{h_m}{h_r}\right)^A \qquad (2.13)$$

where U_m is the measured wind speed at elevation h_m,

$\quad U_r$ is the wind speed at the reference level h_r, and

$\quad A$ is an empirical constant approximated by Det norske Veritas (1982) as 0.15.

Accurate hindcasting requires more precise atmospheric boundary layer models such as the method used in the CMC forecast spectral wind model (Delage, 1985). The same procedure is also required to derive surface winds from the surface pressure data via the gradient wind. With this method, the friction velocity u_* is determined as a function of the free-atmosphere (or gradient) wind u_o, the air column stability which depends on the upper air temperature and the sea surface temperature, and an empirical form for the surface roughness length (conceptually equivalent to C_D). A logarithmic profile of U is assumed, as a function of air column stability and surface roughness length, to extract wind speed $U(z)$ at the required reference elevation z. For the neutral stability case, the solution is determined from

$$\left.\begin{array}{l} u_* = \kappa u_o \{\ln(\ln(z/z_o))\}^{-1} \\ U(z) = (u_*/\kappa) \ln(\ln(z/z_o)) \end{array}\right\} \qquad (2.14)$$

where κ is von Karman's constant (0.4)

$\quad z_o$ is the surface roughness length ($0.35\ u_*^2/g$)

$\quad g$ is the gravitational constant

The angular rotation of the wind vector at the sea surface due to the frictional boundary layer is also calculated and depends on the same stability and surface roughness length parameters as well as the boundary layer thickness.

3.0 SPECTRAL WAVE MODELS

Spectral models have evolved with improvements in understanding of the physics of wave generation. The "first generation" models, dating from the 1960's, are discrete spectral formulations that consider the frequency bins to be independent of each other. Hasselmann et al. (1973) have shown not only that interactions between the frequencies (wave-wave interactions) are important, but that during the growth stage of wind seas, they are the principal source of energy on the low frequency forward face of the spectrum. The "second generation" of discrete spectral models mimick these interactions by redistribution of the energy over the frequency bins after each modelling time step. It was the difficulty of generalizing this energy redistribution mechanism for arbitrary spectra that gave impetus to the parametric spectral modelling method. These models too are "second generation", however, in that they have had to include a priori restrictions on spectral shape because an accurate representation of the non-linear wave-wave interaction process that can be evaluated economically is not available.

The "third generation" model proposed by the WAM Group (Komen, 1984) is based on a complete representation of all source terms in the energy conservation equation that removes all a priori restrictions on spectral shape. Some preliminary results of this third generation model have been presented by Komen, but full implementation is still a few years away.

In this chapter, three model classes are described with specific details drawn from a particular wave model. The models represented are as follows:

Model Class	Model Name	Reference(s)
second generation parametric spectral	The HYPA Model	Hasselmann et al. (1976) Günther et al. (1979a,b)
first generation discrete spectral	The ODGP Model	Cardone et al. (1975)
second generation discrete spectral	The ADWAVE Model	Resio (1981, 1982, 1985)

3.1 Parametric Spectral Wave Models

There are many parametric spectral wave models that have been developed for research, operational wave forecasting, and wave hindcasting. Of these, the best known are based on the work of K. Hasselmann and his co-workers (Hasselmann et al., 1976; Günther et al., 1979a,b) and the following discussion is based on their techniques.

The basic concept in parametric spectral wave modelling is to solve the energy balance equation by assuming a parametric form for the energy spectrum E(f). The parametric spectrum $\hat{E}$ is expressed in terms of a set of spectral parameters a_i that are readily specified based on the results of wave measurement experiments.

To obtain solutions to (2.1) naturally involves several simplifying assumptions. Hasselmann et al. (1976) integrated (2.1) over direction to obtain model equations in the form of (2.2) and used the JONSWAP parametric spectral form for $\hat{E}$(f) to substitute for E(f). This substitution yields equations of the form

$$\frac{\partial a_i}{\partial t} + D_{ijk}\frac{\partial a_i}{\partial x} = T_i \qquad (3.1)$$

where a_i = the set of five JONSWAP parameters $\{f_p, \alpha, \gamma, \sigma_a, \sigma_b\}$

D_{ijk} = the wave propagation velocities (functions of a_i)

T_i = the source terms (functions of a_i)

Hasselmann et al. (1976) argued that of the five spectral parameters only the first two, f_p and α, are necessary as modelling variables because of the shape invariance of the spectrum. This simplification results in a prognostic model for wave energy in terms of $\nu = f_p U/g$ (non-dimensional peak frequency) and α with equations similar in form to (3.1). Günther et al. (1979) included all five JONSWAP parameter spaces.

In order to solve these equations, empirical formulae are substituted for the wind input and dissipation processes, and S_{nl} is parameterized by a look-up table of exact solutions to the Boltzman integral for a range of spectra $\hat{E}(f;a_i)$. In practice, this approach is simplified by using the solution of only the mean JONSWAP spectrum. The result is quite simple S_{nl} parameterizations:

$$S_\nu \sim -0.54 \, \alpha^2 f_p^2$$
$$S_\alpha = -5.0 \, \alpha^3 f_p$$
$$S_\gamma = -16.0(\gamma - 3.3)\alpha^2 f_p$$
$$S\sigma_a = -[25.5(\sigma_a - 0.07) - 0.5(\sigma_b - 0.09)]\alpha^2 f_p$$
$$S\sigma_b = -[25.5(\sigma_b - 0.09) - 0.5(\sigma_a - 0.07)]\alpha^2 f_p$$

The constant coefficient of S_ν is calibrated by empirical relations of f_p and α as functions of non-dimensional fetch. Günther et al. (1979b) report using a value of -0.586 for the North Sea.

The expression for S_{in} is given by Günther et al. (1979b) as

$$S_{in} = 5.022 \times 10^{-3} \, \nu^{4/3} \alpha f_p$$

and occurs in only the α equation of the set specified by (3.1). The constant coefficient is also determined from the empirical fetch dependence of f_p and α. In the models described by Hasselmann et al. (1976) and Günther et al. (1979b), it has been assumed that the spectral domain of interest lies below the region of S_{ds} influence so that this dissipation term was omitted.

The equations are solved on a spatial grid as a function of time by a predictor-corrector method (Günther et al., 1979a). The solution scheme is reported to be second order accurate in space and time and the stability criterion requires that the ratio of grid spacing to time step $\Delta x / \Delta t$ be larger than the largest group velocity of waves in the solution domain. In the Günther et al. (1979a) application, a 2 km grid and a 5 min integration step were used to model selected periods of the JONSWAP experiment. The cosine-squared directional spreading function, independent of f, was assumed to apply and the mean wave direction was specified by the average local wind direction. The entire parametric model is thus a straightforward set of five equations in the five parametric spectral unknowns a_i. Once these a_i are determined, the spectrum $E(f)$ is specified, and application of the directional spreading function provides $F(f, \theta)$.

One severe limitation of parametric spectral models is that they exclude any swell energy contributions to the wave spectrum. The coupling of a parametric spectral wind-sea model and a swell model is referred to as a hybrid parametric spectral model. The disadvantages with the hybrid models are well-known (Günther et al., 1979b; Janssen et al., 1984). The first problem is the large computational housekeeping requirement to convert between ray characteristics and the wind-sea fixed grid mesh to incorporate appropriate

contributions of swell energy to the calculated E(f) solution--but this is chiefly an inconvenience. The other disadvantage arises from the large number of somewhat arbitrary assumptions required to distinguish wind-sea from swell and to deal with the interaction of the two. This difficulty is much more fundamental and rather poor performance of the Dutch operational forecasting model has been attributed to it (Janssen et al., 1984).

For example, Günther et al. (1979b) made the following assumptions.

(1) Wind-Sea Becoming Swell: If $f_p < 0.13g/U$ (i.e. below the PM value of f_p for a 10 m elevation wind) then $f_p = f_p(PM)$; α is adjusted to conserve energy in the wind-sea portion of E(f) above $f_p(PM)$; energy at $f < f_c$ (a cut-off frequency) becomes swell where f_c is determined numerically to maintain the same total energy in E(f) before and after swell separation; cosine-squared directional spreading of swell is included.

(2) Swell Becoming Wind-Sea: If swell frequency exceeds $0.9f_p$ then swell is absorbed instantaneously into the wind-sea spectrum without regard to direction; energy is conserved by adjusting f_p with α and γ fixed.

(3) Swell Interacting With Wind-Sea: Swell may exist at frequencies subject to wave growth, but outside the range of non-linear interaction, i.e. $f_o < f < 0.9f_p$ (defining f_o as $g/2\pi U \cos\psi$ where ψ is the angle separation between wind and swell directions); the Miles-Phillips growth mechanism is assumed such that $S_{in} = 2\pi f [(f-f_o)/f_o][c\rho_a/\rho_w]$ for $f > f_o$ and otherwise $S_{in} = 0$ (where ρ_a = density of air, ρ_w = density of water and $c = 0.05$).

These assumptions by Günther et al. (1979b) are described as intuitive, and have no doubt been refined, but they do illustrate the fundamental objection to parametric spectral wave modelling.

3.2 Discrete Spectral Wave Models

Discrete spectral wave models are solutions of (2.1) achieved by finite difference techniques in which the spectrum $F(f, \theta)$ is divided into discrete frequency and direction domains. These models have three obvious advantages: (1) they do not rely on empirical spreading functions to redistribute wave energy by direction, (2) they do not impose a universal parametric spectral shape except when energy saturation is achieved, and (3) they treat local wind sea and swell as a combined phenomenon rather than as a hybrid combination of different wave types.

The various operational and research models in this class are distinguished from one another primarily by their parameterization of the energy source term $S(f,\theta)$, and two fundamentally different formulations have developed. One of these, exemplified by the ODGP model (Cardone et al., 1975), bases $S_{in}+S_{ds}$ on empirical formulations to describe wave initiation by turbulent atmospheric pressure fluctuations at the sea surface and wave growth by the Miles-Phillips instability mechanism. Furthermore, the Cardone model assumes that S_{nl} is a negligible contributor to the energy balance. The other approach to parameterization of $S(f,\theta)$ is much more closely based on the JONSWAP results including each of the S_{in}, S_{ds} and S_{nl} terms, and Resio's (1981, 1982) ADWAVE model is the most well-developed, well-published example.

3.2.1 The ODGP Model

The ODGP model was developed by Cardone et al. (1975) under the oil industry sponsorship of the Ocean Data Gathering Program in the Gulf of Mexico. The impetus for the study was to monitor wind and wave conditions during hurricanes with a view to building a calibrated wave hindcasting model to describe the evolution of hurricane waves throughout the Gulf. The ODGP wave model is described by its authors as "a rather straightforward application and calibration of the Pierson-Tick-Baer (PTB) model", published by Pierson et al. (1966). Because the wave model came to be commercially exploited by Cardone, the published details of its code and calibration procedure are sketchy.

Wave growth and dissipation are applied to down-wind spectral components according to the empirical formulae

$$S_{in} = \left[A(f,\theta,U) + B(f,\theta,U).F(f,\theta) \right] \left[1 - \left(\frac{F(f,\theta)}{F_\infty(f,\theta,U)} \right)^2 \right] \qquad (3.2)$$

where A   is the linear growth coefficient which initiates the excitation of gravity waves on a calm sea surface,

     B.F is the exponential growth term incorporating the Miles-Phillips instability mechanism,

     U   is the wind speed,

     F_∞ is the saturated PM spectrum for a given wind speed multiplied by a directional spreading function $G(f, \theta)$.

The formulations of the A and B coefficients are unpublished. The A term is relatively unimportant, serving only to initiate spectral energy growth.

Dissipation of upwind spectral components is not described by Cardone et al. (1975), but in the original PTB model it had the form:

$$\frac{F_{diss}}{F_o} = [\exp(-78\sqrt{m_o}f_i^4)]^N \tag{3.3}$$

That is, dissipation was applied as a damping function on the upwind components of the initial spectrum $F_o(f,\theta)$. Equation (3.3) is calibrated to be applied at 2-hourly intervals where

m_o is the zeroth moment (ft^2) of the wind sea spectrum (i.e. the half-plane down-wind spectrum),

N   is a function of the deviation of the wave component direction from the local wind direction and calculated as $N=4-[|\theta_i-\theta_w|-180]/15$,

θ_i is the upwind wave component direction,

θ_w is the local wind direction.

Details of the Gulf of Mexico hindcast illustrate another difference between discrete and parametric spectral models, the large computer memory requirements for the finite difference solutions to (2.1). The Gulf of Mexico study area was represented by 1265 discrete points arranged in a triangular grid pattern on an icosahedral-gnomonic map projection in which straight lines are great circles and hence are deepwater wave trajectories. The nominal grid spacing was 20 nautical miles.

At each of these grid points a discrete directional spectrum was calculated and stored that was comprised of 13 frequency bands and 24 direction bands. In all then, almost 4×10^5 components of spectral energy were determined at each hourly time step. This demand for computer memory and input/output to mass storage devices is the primary limitation to implementation of such wave models on small computers.

Fig. 3.1 is from published results of the ODGP hurricane Camille hindcast and illustrates the performance of this model. Based on the hurricane Camille results, three other hurricane hindcasts and one tropical storm hindcast, Cardone et al. (1975) report that the root-mean-square error in the predicted maximum wave height is 4.9 feet (1.5 m) and the bias is +1.5 feet (0.5 m) in sea states of maximum wave height ranging between 20 and 80 feet. Such values represent generally satisfactory accuracies, but the measurement-prediction comparison pairs are almost certainly the maximum measured and the maximum predicted wave heights, without regard to the time of occurrence of either.
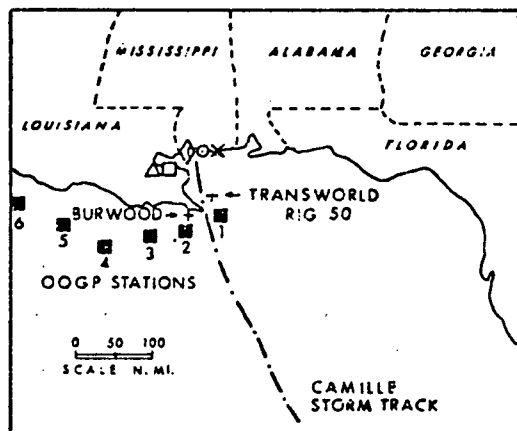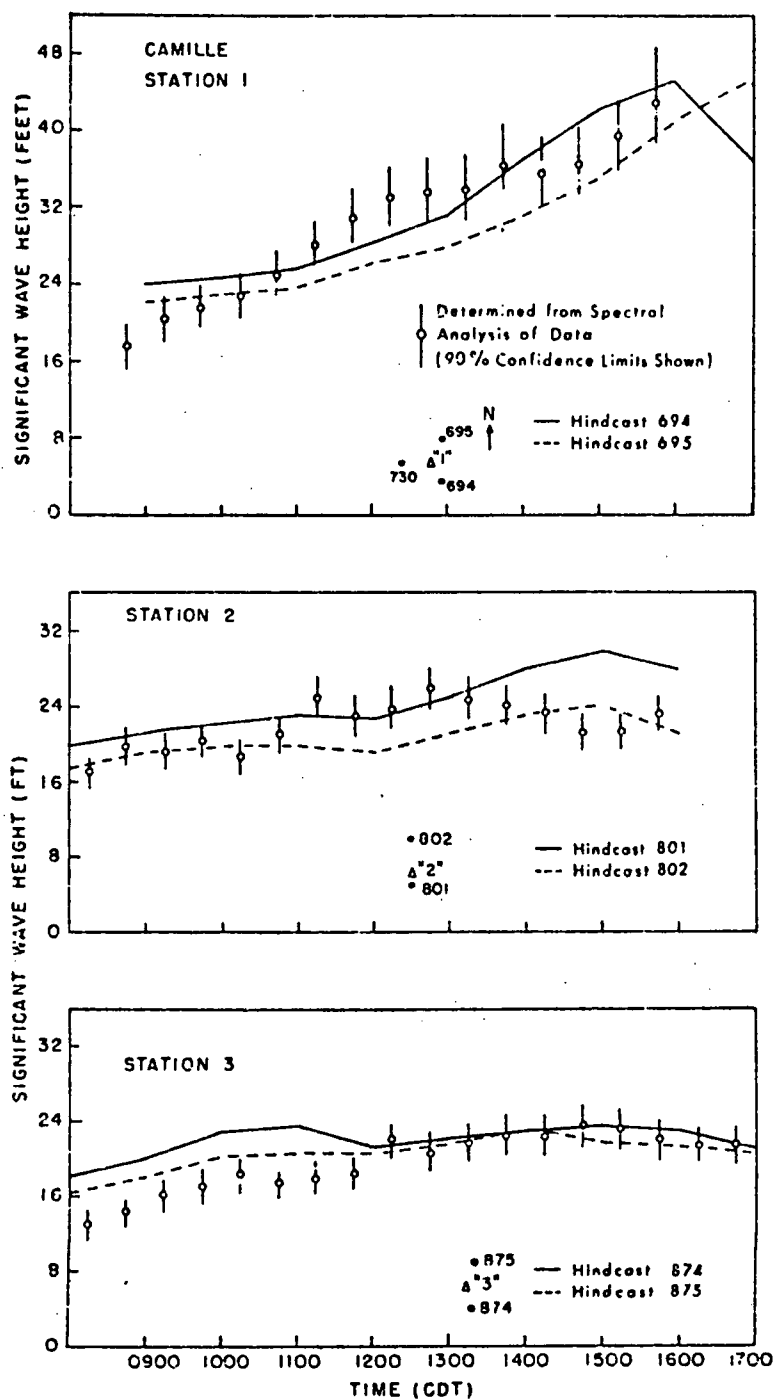
Fig. 3.1   Measured and hindcast significant wave height time-series at three stations in the Gulf of Mexico during Hurricane Camille. The hindcast site numbers designate grid points close to the measurement sites. (From Cardone et al., 1975).

3.2.1 ADWAVE

The ADWAVE hindcast model has evolved from precursors described by Resio (1981, 1982). Its present formulation (Resio, 1985) is a finite difference solution to the complete energy balance equation (2.1) in which the source terms include wind input, non-linear energy transfer between wave frequencies (wave-wave interaction) and dissipation. Propagation is done by the method of characteristics which is generalized for shallow water calculations. The energy spectrum $F(f,\theta)$ is discretized in frequency and direction (as illustrated schematically in Fig. 3.2) at each point on a regular x-y grid applied over the modelling domain. Propagation and the source/sink mechanisms are calculated as changes in energy in each of these f and θ elements.

Propagation

The propagation of wave energy is most readily understood in terms of a single frequency-direction element $F(f_k, \theta_m)$ in a deep water location. At a fixed solution grid location (i,j) the energy content at time $n+\Delta t$ in the discretized element $F(f_k, \theta_m; i, j)$ can only have originated from the position $(i+\delta x, j+\delta y)$ at time n, and will have travelled a distance $c_g \Delta t$ along the characteristic ray. Along this ray the quantity $F.c.c_g$ is conserved, f is invariant and θ only changes as the ray moves from deep into shallow water. The deep water (constant θ) case is illustrated in Fig. 3.3a. The energy content of $F(f_k, \theta_m)$ at $(i+\delta x, j+\delta y)$ is determined by bilinear interpolation of F at time level n, first at the grid intersection (i.e. at point B in Fig. 3.3a) and then at the ray origination point $(i+\delta x, j+\delta y)$ (i.e. at point O in Fig. 3.3a).

The same principle applies for the generalized depth case, but the characteristic rays are curvilinear as depicted in Fig. 3.3b. The back ray tracing to location points O and B is done in small incremental steps in order to vary c and c_g as functions of depth.

Since the model is written in terms of fixed discrete frequencies and directions with depth specified independently of time, all the interpolation constants (location of points B and O), phase and group velocities may be pre-calculated for each grid point (i,j) at each frequency and direction. This pre-processing adds very significantly to the computer memory requirements, but speeds the time stepping calculation phase of the model.
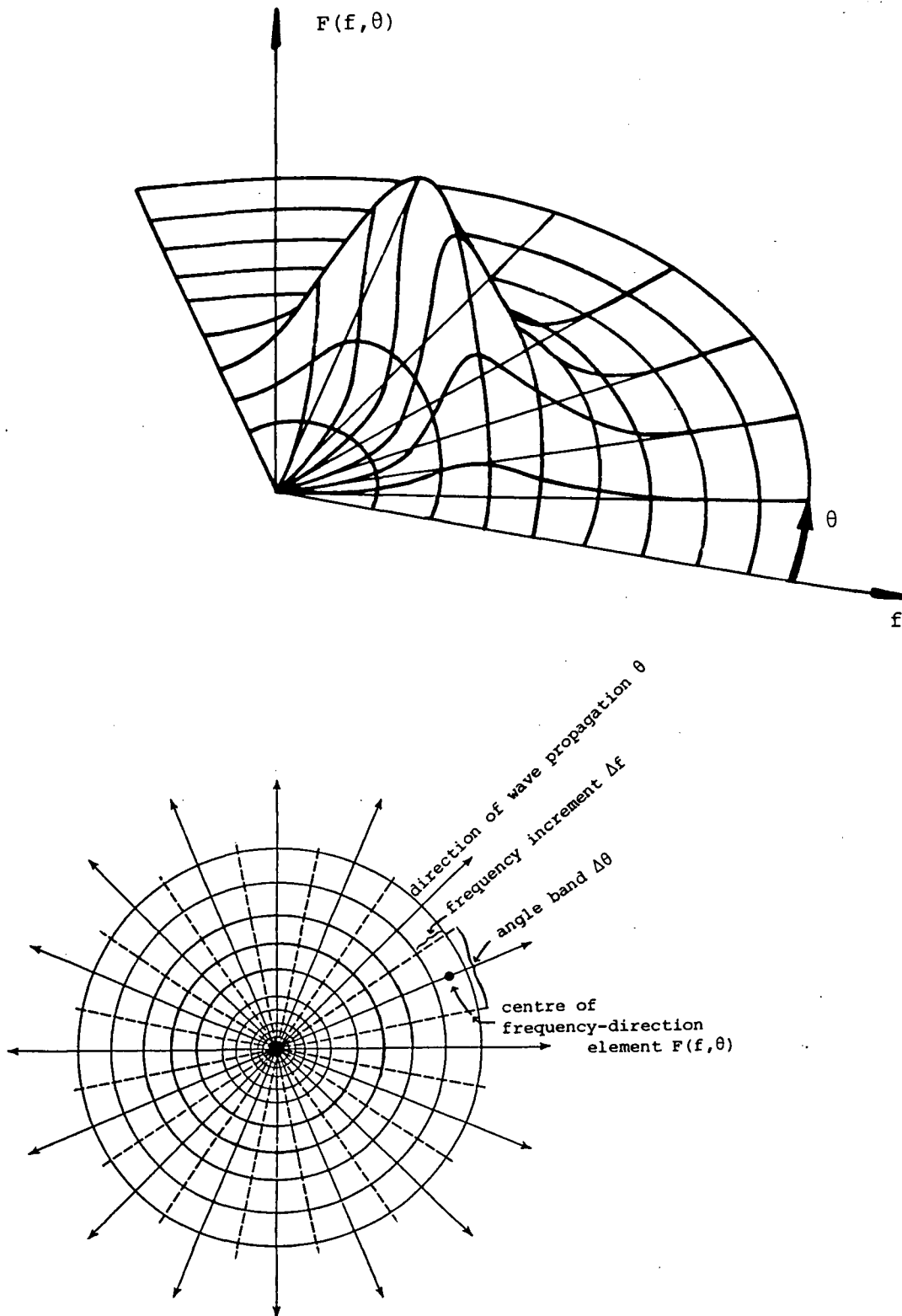
Fig. 3.2   Representation of a two-dimensional spectrum. The upper
panel (from Sarpkaya and Isaacson, 1981) shows a portion
of F(f,θ) in three-dimensional relief and the lower
panel shows the discretization of that spectrum in
increments of frequency and direction as applied in
ADWAVE.

a

position of wave component at beginning of time step

position of wave component at end of time step

b

interpolation along ray

interpolation along grid boundary
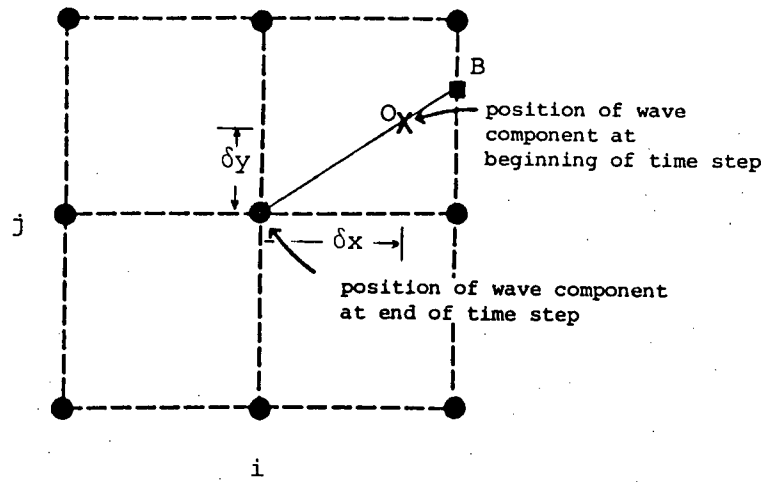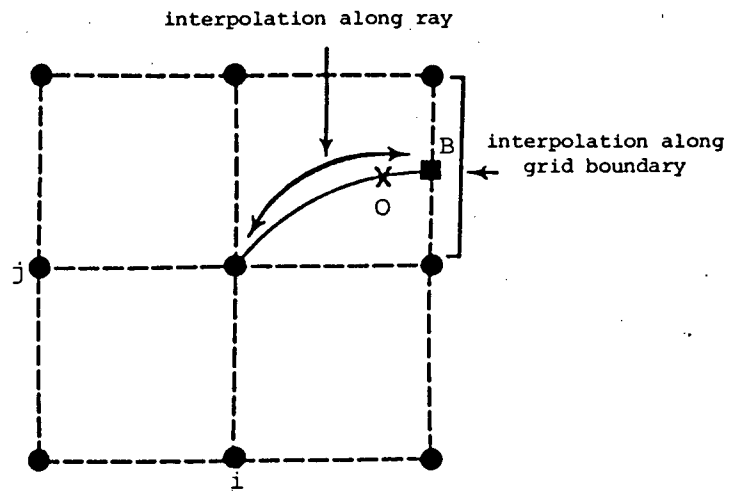
Fig. 3.3   The bilinear interpolation scheme in ADWAVE (a) in deep water and (b) in shallow water.

Source Terms: $S_{in} + S_{nl} + S_{ds}$

Hasselmann et al. (1973) and Resio (1981, 1982) have shown theoretically and empirically that in deep water the balance among the source/sink terms involves primarily the wind input S_{in} and the wave-wave interactions S_{nl}. There is also a growing resource of measurements to give empirical evidence that this is also so in shallow water (Bouws et al., 1985). Further evidence of the suitability of the Resio (1985) formulation for the wave-wave interaction mechanism comes from a recent study sponsored by the ESRF Waves Committee (Hodgins et al., 1986). The transformation of deep water waves into shallow water as predicted by ADWAVE was compared with measurements in 12 m of water on Sable Island Bank with a directional wave buoy during winter storms in 1984-85. Preliminary results indicate that the agreement is quite acceptable, within about 10% in total energy and significant wave height but somewhat low in peak period.

In ADWAVE the energy spectrum is considered to be composed of three segments as shown in Fig. 3.4: the forward face at frequencies below f_p, an intermediate range where S_{in} is operational and the high frequency tail of the spectrum. The high frequency tail (region III) is regarded as fully saturated at all times and governed by the $E(f) \propto f^{-5}$ power law. This part of the energy spectrum is also referred to as the Phillips' equilibrium range where energy input is balanced by dissipation through whitecapping and wave breaking.

Modern hypotheses (Resio, 1985; Kitaigorodskii, 1983) argue that the source of energy to region III is not from the local wind, but from resonant nonlinear wave-wave interactions originating from region II. The transition between regimes II and III in deep water is approximately (Kitaigorodskii, 1983)

$$\tilde{\omega}_g = \frac{2\pi f_g U_a}{g} \approx \frac{\beta}{\alpha_u} \tag{3.4}$$

where α_u is approximately 4.4×10^{-3},

β is approximately 1.5×10^{-2}, and

U_a is the average wind speed.

Thus f_g is about $5.32/U_a$. For a moderate wind of 20 knots ($U_a = 10$ m/s) then f_g is about 0.5 Hz or $T_g = 2$ s. For the transition to be at the normal high frequency cutoff in wave modelling ($T_g = 5$ s), U_a must be 26.6 m/s or just over 50 knots. It would therefore be rare to have a region III (i.e. an f^{-5} slope regime) in a hindcast wave spectrum.
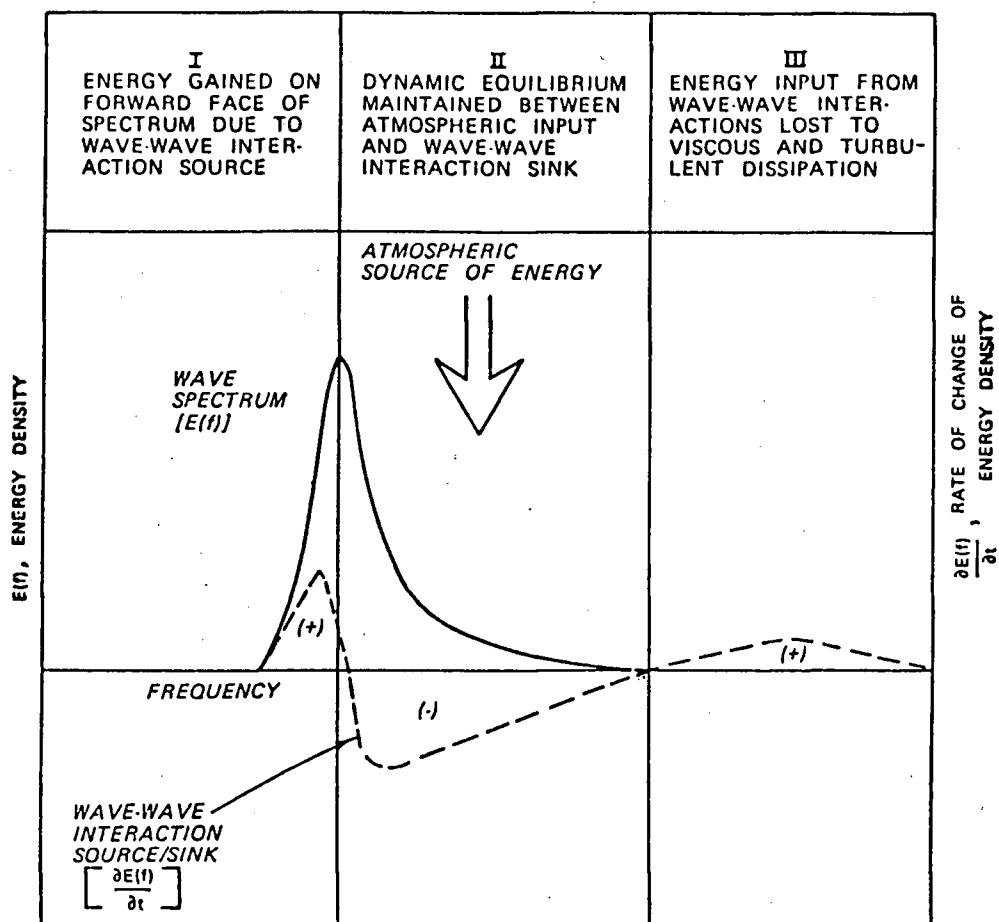
Fig. 3.4   Energy regimes within a spectrum during active wave growth. (From Resio, 1982).

Resio (1985) and Kitaigorodskii (1983) hypothesize that region II also has an equilibrium shape characterized by a power law, support for which has been found by Kitaigorodskii in experimental data from several sources:

$$E(\omega) = \alpha_u g U_a{}^{-4} \qquad (3.5)$$

where α_u is a non-dimensional constant ($\simeq 4.4 \times 10^{-3}$),

      g is the gravitational constant,

      U_a is the mean wind speed ($u_*/U_a \simeq 1/30$), and

      ω is angular frequency ($2\pi f$).

In other words, the saturated shape of this part of the spectrum is invariant, but the energy content depends directly on mean local wind speed. The limits of the range are f_p and f_g, and as such they have dynamic definitions that depend, for the most part, on local wind speed. This central region of the energy spectrum has been designated by Kitaigorodskii (1983) as Kolmogoroff's equilibrium range in recognition of the parallels between Kitaigorodskii's theories of energy transfer from low to high frequencies in wave spectra and Kolmogoroff's theory of a turbulent energy cascade from low to high frequencies.

In ADWAVE, the wind energy input to region II is defined as

$$S_{in} = \lambda \frac{\rho_a}{\rho_w} C_D \frac{U_{10}^3}{g} \qquad (3.6)$$

where λ is a partitioning coefficient expressing the fraction of wind momentum that enters the wave field,

    ρ_a is air density,

    ρ_w is water density,

    C_D is the surface drag coefficient,

    U_{10} is the 10-m elevation wind speed, and

    g is the gravitational constant.

Hasselmann et al. (1973) concluded that the minimum atmospheric momentum flux into the wave field is of the order of 10 to 40% of the total momentum transfer across the air-sea interface, but it may be up to 100% if dissipation is important. Resio (1985) argues that the partitioning coefficient is more reasonably about 60%.

The drag coefficient has the form proposed by Large and Pond (1981) with slightly different coefficients:

$$C_D = (0.75 + 0.054 \ U_{10}) \times 10^{-3} \tag{3.7}$$

Resio (1985) has assumed that where bottom effects are negligible S_{in} is exactly balanced by S_{nl} when the energy spectrum is saturated in region II. Based on this equilibrium balance and an approximate integration of the collision (Boltzmann) integral, the expression for the total energy flux rate in terms of spectral parameters is given as

$$S_{nl} = \frac{\varepsilon \sqrt{g} \ E_o^3 \ k_p^{4.5}}{\tanh^{3/4}(k_p d)} \tag{3.8}$$

where ε is a non-dimensional constant (evaluated numerically to be of the order of 100),

g is the gravitational constant,

E_o is the total spectral energy in the domain $f_p < f < \infty$,

k_p is the peak wave number ($4\pi^2 f_p^2/g$ in deep water), and

d is the local water depth.

When the wind-wave system is not in balance, $S_{in} - S_{nl}$ provides a net source or sink of energy to or from the Kolmogoroff range although the method of distributing the net energy among the wave numbers or frequencies (and directions) is not discussed by Resio in any of the referenced works (Resio, 1981; 1982; 1985).

Energy growth on the forward face of the spectrum (region I in Fig. 3.4) is defined as a fixed proportion of S_{nl}, the remainder of which is dissipated by implicit transfer to the permanently saturated spectral region III. The shape of the forward face is presumed to have an evolutionary rather than an equilibrium form (Resio, 1985). The rate of energy transfer among the frequencies is viewed as an analogue of heat transfer in a medium of constant conductivity. In deep water, this idea yields

$$E(f) = E(f_p) \ \exp\{-\delta(f/f_p)^{-4}\} \tag{3.9}$$

where δ is a dimensionless constant.

Other energy source-sink terms included in ADWAVE are shoaling, refraction and bottom interaction effects, although none of these factors are included in the deep water tests performed as part of this research.

Using historical wave measurements from four different locations (Duck, North Carolina; Hiezu Coast, Japan; Nishikinohama Coast, Japan; and Melkbosstrand, South Africa), Resio (1985; also included in Hodgins et al., 1986 and Seaconsult, 1986a) has been able to verify the performance of the shallow water implementation of ADWAVE for a wide variety of energy source-sink conditions. Table 3.1 presents Resio's summary of these test cases. The four righthandmost columns give the relative importance of shoaling, refraction, wind input and nonlinear interactions in each spectral test case. In case 1, for example, as the wind input diminishes with time, the S_{nl} term quickly becomes negligible and shoaling begins to be the dominant source of wave growth. Columns 2 and 3 give the simultaneous H_s values at the deeper H_1 location and the shoreward shallow H_2 site. It is the difference between these H_s values that is being attributed to the various S(f) terms in the last four columns.

The ADWAVE prediction of H_s at site H_2 is given in column 4 and is almost always within 10% of the measured value without any apparent bias. In the two examples that exceed the 10% deviation, the relative importance of the S(f) terms is about the same but certainly not uniquely so. These results indicate very acceptable performance by ADWAVE over a broad range of physical prototype conditions.

Table 3.1

Comparison of Predicted and Observed Wave Heights

as a Function of

Modelled Energy Source Terms

Date-Time	H_1	H_2	H_{pred}	Dev	% Dev	$%_1$	$%_2$	$%_3$	$%_4$	
8210100100	1.8	1.8	1.8	.0	-.1	-4.5	.0	49.7	-45.8	
8210101300	2.4	2.6	2.8	.2	7.8	54.1	.0	30.6	-15.3	
8210110100	2.1	2.7	2.6	-.1	-3.7	59.0	.0	31.7	-9.3	
8210111300	2.0	2.6	2.4	-.2	-6.1	83.7	.0	10.5	-5.8	- Case 1
8210120100	2.0	2.4	2.5	.1	5.3	91.9	.0	1.9	-6.2	
8210121300	2.4	3.1	3.0	-.1	-3.3	93.1	.0	.6	-6.3	
8210121900	2.2	3.1	2.8	-.3	-9.9	94.9	.0	.7	-4.4	
8210241300	4.1	3.4	3.5	.0	1.1	.9	-.9	42.5	-55.7	- Case 2
8210251300	3.6	3.2	3.6	.4	13.5	50.4	-11.7	.1	-37.9	
8410060700	1.1	1.0	1.0	.0	-3.0	-.9	.0	48.0	-51.1	
8410061900	1.4	1.2	1.3	.1	5.7	-12.2	-.4	41.8	-45.5	- Case 3
8410070700	1.5	1.4	1.5	.0	2.1	-18.3	-.9	50.0	-30.9	
6412021405	1.9	1.8	2.0	.1	6.1	59.1	-22.2	.0	-18.7	
6412021434	2.4	2.1	2.4	.3	12.0	61.4	-16.4	.1	-22.1	- Case 4
6412021527	2.0	2.0	2.1	.1	4.3	69.6	-14.6	.2	-15.6	
6410021546	1.9	1.9	1.9	-.1	-2.9	-63.5	-18.8	.3	-17.4	
6401311620	.8	.7	.6	.0	-2.2	-.9	-.2	37.6	-61.4	- Case 5
6401311710	.8	.8	.8	.0	6.6	-.5	-.6	52.6	-46.4	
6901160000	1.7	1.5	1.5	.1	4.0	-44.6	-31.3	15.3	-8.9	
6905130000	3.4	3.1	3.3	.2	6.4	27.4	-13.6	.3	-58.8	
6905290000	2.7	2.4	2.6	.2	8.4	17.4	-49.3	.1	-33.2	
6908190000	3.4	3.0	3.0	.0	-.5	-59.3	-2.2	1.4	-37.0	- Case 6
6910070000	2.1	2.2	2.3	.1	3.4	81.9	-5.4	7.1	-5.6	
6911180000	4.4	3.5	3.6	.2	4.5	17.4	-15.7	6.3	-60.6	
7001270000	2.7	2.6	2.5	-.1	-3.6	-7.7	-69.8	5.9	-16.6	

KEY

H_1 .... measured wave height (m) at site 1 (deeper)

H_2 .... measured wave height (m) at site 2 (shallower)

H_{pred} .... predicted wave height (m) at site 2

Dev ...... $H_{pred} - H_2$ (m)

% Dev .... $100 \times (H_{pred} - H_2)/H_2$

%1 .... percentage of change due to shoaling

%2 .... percentage of change due to refraction

%3 .... percentage of change due to wind input

%4 .... percentage of change due to nonlinear interactions

4.0 WIND FIELD SENSITIVITY: AN APPLICATION OF ADWAVE

To investigate the effects that wind field errors may cause in wave hindcasting, a systematic sensitivity analysis has been constructed. The choice of ADWAVE for the wave hindcast model was dictated largely by availability and familiarity. On the other hand, it is a good choice because it represents a very up-to-date solution method for the conservation of energy equation in arbitrary water depths. Since it contains parameterizations of more physics than is found in a first generation model like ODGP, it is expected to more accurately model diverse input conditions without calibration for each new situation. ADWAVE has been successfully applied on the west coast of Canada (Hodgins and Nikleva, 1986), in the Beaufort Sea (Seaconsult, 1986b) and on Sable Island Bank on Canada's east coast (Hodgins et al., 1986; Seaconsult, 1986a).

Because it is a complex computer program, it is very demanding of computer resources: CPU time, virtual memory and peripheral mass storage. However, for important hindcasting applications its use is justified on the grounds of minimizing modelling errors, especially if wind field errors may be large (Resio and Vincent, 1979). These authors note that input and wave model errors are generally additive, so that in most cases reducing either one automatically reduces the total rms error. The characteristic wave model error is usually a bias in total energy (significant wave height) and/or frequency distribution (peak period). For engineering applications, it is important to remove as much bias as possible from a wave hindcast and then to understand the probable nature of any remaining random errors. In this way safe, economical designs are achieved with optimal safety factors.

4.1 Structure of the Sensitivity Analysis

The purpose of this investigation is to quantify the variations in hindcast sea-state parameters in the B.C. coastal waters that are attributable to known variations in the meteorological forcing parameters.

The sea-state parameters of interest are significant wave height (H_s), peak spectral period (T_p), mean wave direction ($\bar{\theta}$) and spectral shape ($E(f)$ or $F(f,\theta)$). The physical determinants of these parameters (in deep water) are wind speed, fetch and duration. In turn these factors are governed by meteorological conditions of the surface pressure field: intensity of the low pressure system (radial extent of the system and depth of the central low), path of the low in relation to the coastline or to sites of interest, rate of storm passage along its trajectory and rate of storm intensification. Fig.

4.1 illustrates how these factors are related. In particular it shows that most surface pressure parameters influence the fetch, primarily through control of the wind field curvature.

To systematically alter the surface pressure patterns, an idealized model was utilized in which a radially symmetric pressure field P is defined as a function of radius r in terms of the central pressure P_o, the mean pressure field, and a radial scale R. In accordance with the usual wind-wave hindcasting conventions, one surface pressure map was constructed for each 6-hourly hindcast interval of a 2.5 to 3.5 day storm duration. An analysis of 27 years of severe storms in the northeast Pacific by Lewis and Moran (1985) was used to select reasonable values for P_o and R as well as for the trajectory of the central low X_o, the velocity of the low along that trajectory $\Delta X_o/\Delta t$, the position of $P_o(min)$, and the rates of intensification and filling of the low $\Delta P_o/\Delta t$. Gradient and near-surface wind fields were calculated from the surface pressure maps and these latter vector winds were interpolated in time to the wave model time step.

The hindcast model configuration was designed to provide a very detailed $1°x1°$ latitude-longitude specification of the deep water sea-state. The present application output would provide the input spectral boundary conditions for shallow water coastal hindcasting.

Hindcast results consist of time-series of one- and two-dimensional spectra (E(f) and F(f,θ)) and derived sea-state parameters H_s, T_p and $\bar{\theta}$ at selected locations within the modelling domain as well as complete fields of the derived parameters at every point on the solution grid.

4.2 Wind Field Specification

The idealized wind fields are derived from surface pressure patterns that are fully specified in time and space by a three parameter model based on

- the time history of the central low pressure position,
- central low pressure as a function of time, and
- a radial scaling parameter

assuming a mean background pressure equal to 1015 mb.

A gradient wind calculation was applied to the surface pressure maps to derive the free atmosphere wind. The boundary layer model described in Section 2.3.3 was used to calculate surface winds suitable for direct input to the ADWAVE hindcast wave model.

derived
sea-state
parameters

$$H_s = 4 \sum_{k} \sum_{m} F_{km} \cdot \Delta f \cdot \Delta \theta$$
$$T_p = 1/f(\max(F_{km}))$$
$$\bar{\theta} = \theta(\max(F_{km}))$$

modelled
sea-state

$$F(f,\theta) \quad f_{min} \leq f \leq f_{max}$$
$$0^{\circ} \leq \theta \leq 360^{\circ}$$

governing
physical
parameters

| U wind | F fetch | t duration |

controlling
meteorological
conditions

| storm intensity | trajectory of storm | velocity of storm | deepening & filling |

surface
pressure
parameters

$$\begin{array}{c} P_o \\ \Delta P/\Delta r \\ R \end{array} \qquad X_o \qquad \Delta X_o/\Delta t \qquad \Delta P_o/\Delta t$$
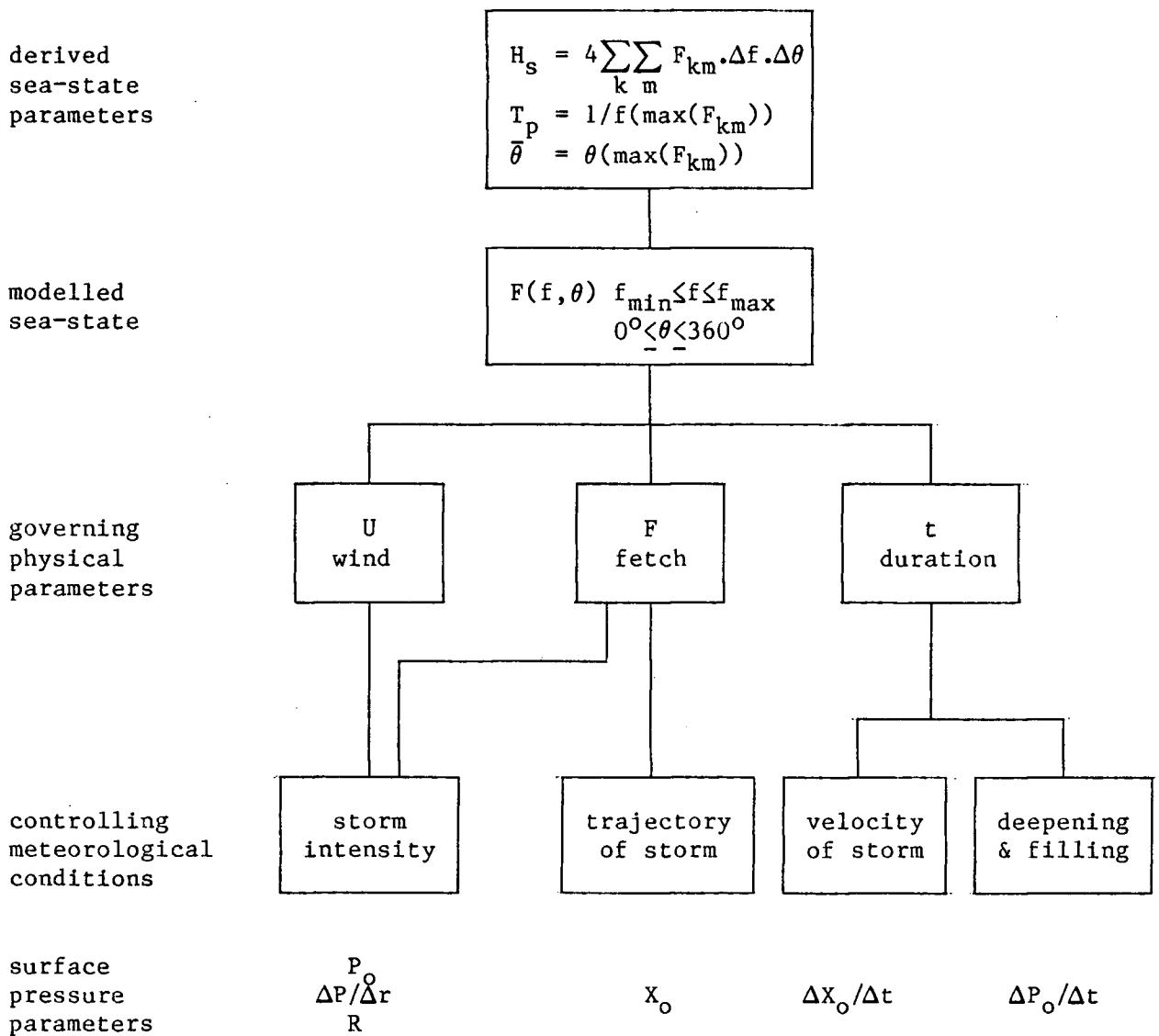
Fig. 4.1   The inter-relationship of meteorological and sea-state
parameters.

4.2.1 The Surface Pressure Field Model

The model used has been adapted from one by Cardone et al. (1975) that was applied to hurricanes in the Gulf of Mexico. In this model an axially symmetric storm pressure field (P) is superimposed on a large scale pressure field ($\bar{P}$) of constant gradient. The combined surface pressure distribution governs the free atmosphere wind field from which the surface wind is determined.

The axially symmetric storm pressure field is defined by the set of isobars P as a function of radius r from the storm centre as

$$P = P_0 + \Delta P \, e^{-R/r} \tag{4.1}$$

where P_0 is the central pressure

ΔP is the pressure gradient between $r \to \infty$ and $r = 0$ (i.e. $\bar{P} - P_0$)

R is a radial scale parameter such that at $r = R$

$$P = P_0 + 0.37\Delta P$$

Fig. 4.2 for Hurricane Camille illustrates how P_0, ΔP and R are determined from surface pressure measurements during the passage of a storm. In this application, $\bar{P}$ was assumed equal to 1015 mb, and P_0 and R were specified for a given geographical location, X_0, of P_0.

If ΔP is represented by the AES standard 4 mb isobar increment, then the radius of those isobars is expressed by rearrangement of (4.1) as

$$r_i = -R/\ln(4i/\Delta P) \quad \text{for } i = 1,I \tag{4.2}$$

where $I = INT((\Delta P-1)/4)$, and the pressure values of those isobars are

$$P_i = 4i + P_0 \quad \text{for } i = 1,I \tag{4.3}$$

This mapping of the pressure field is equivalent to the format of a standard surface pressure chart prepared by AES. Fig. 4.3a illustrates a synthetic pressure field in 5 mb increments for $\Delta P = 60$ mb, $P_0 = 955$ mb, and R=479 km. Since wind speed is inversely proportional to dP/dr, evaluating $d^2P/dr^2 = 0$ provides that the maximum velocity will be found at R/2. For comparison, an actual hand-drawn pressure chart is shown in Fig. 4.3b, based on the few available observations of P. The idealized pressure contours are more concentrated near the centre of the system and much more dispersed near its periphery. The result will be somewhat stronger winds in a small region near the eye of the storm and a broad surrounding area of very weak winds. Neither
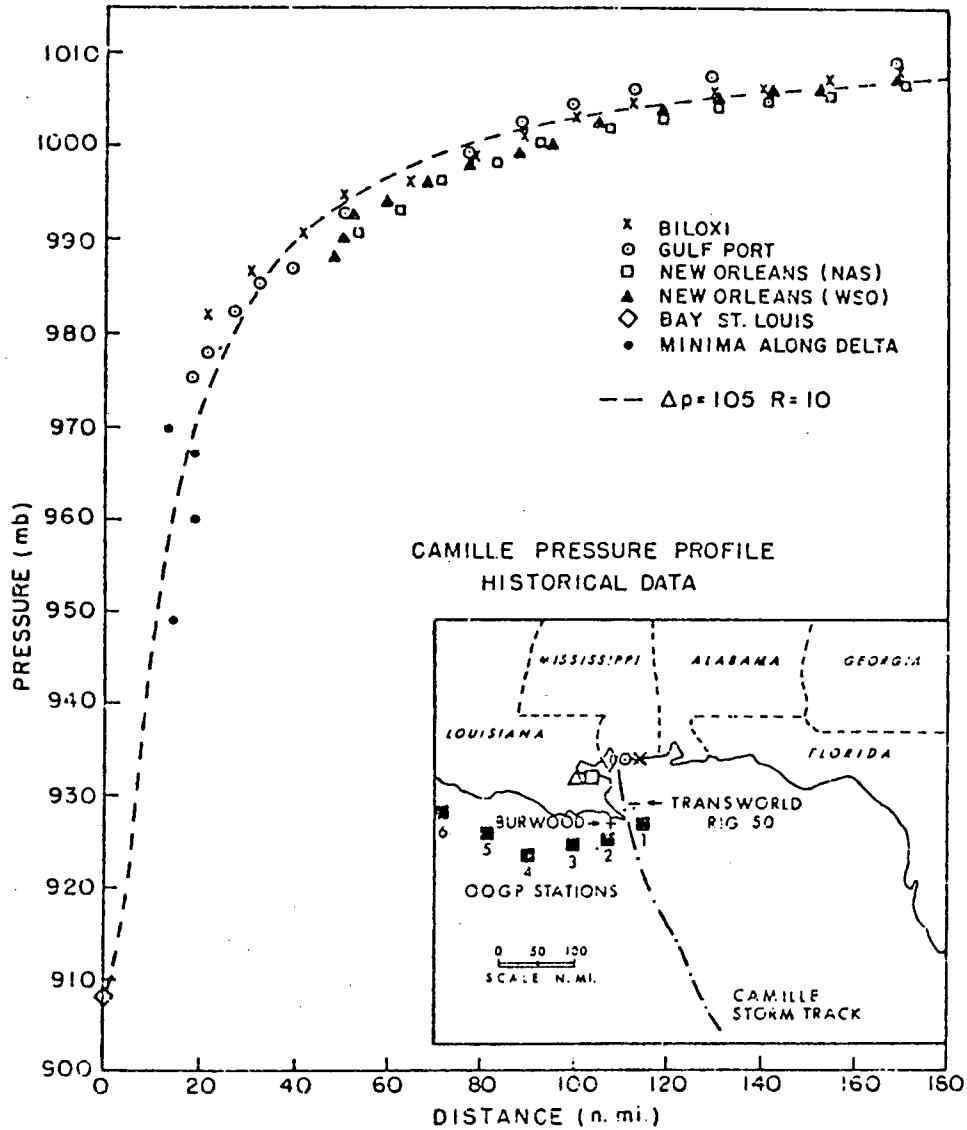
Fig. 4.2   Surface pressure as a function of distance calculated
             from measurements made during the passage of Hurricane
             Camille. (From Cardone et al., 1975).

At 860101 00 hours

Storm centred at   50.00 degrees N 145.00 degrees W
          Central Pressure =   955. mb
          Mean Geostrophic Pressure = 1015. mb
          Pressure Difference =   60. mb
          Radial Scale =   479.46 km

P(i) =	960.	mb	R(i) =	193.	km
P(i) =	965.	mb	R(i) =	268.	km
P(i) =	970.	mb	R(i) =	346.	km
P(i) =	975.	mb	R(i) =	436.	km
P(i) =	980.	mb	R(i) =	548.	km
P(i) =	985.	mb	R(i) =	692.	km
P(i) =	990.	mb	R(i) =	890.	km
P(i) =	995.	mb	R(i) =	1182.	km
P(i) =	1000.	mb	R(i) =	1667.	km
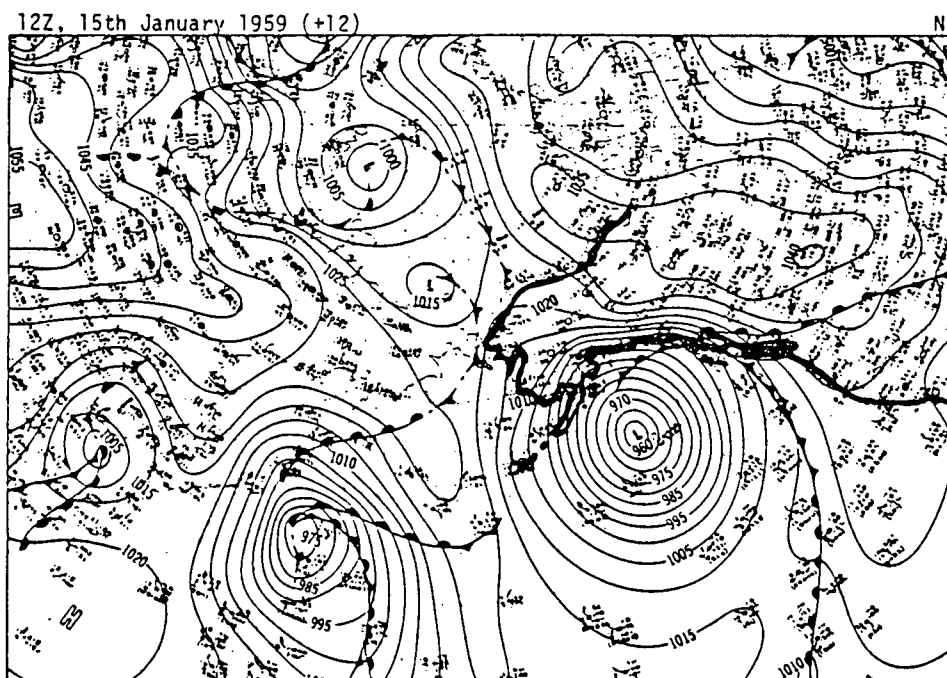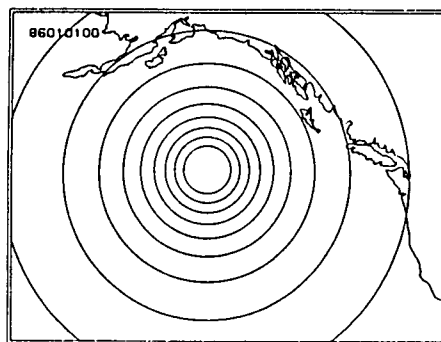
Fig. 4.3   An idealized pressure field for a moderately intense
            storm (upper panel) and an actual surface pressure chart
            (bottom panel), both at approximately the same scale for
            the same low pressure system.

of these differences should restrict the usefulness of the pressure field model for idealized wind field generation.

The storm pressure map in Fig. 4.3a is located on the earth's surface with the central pressure at $X_o(\phi_o, \lambda_o)$ where ϕ_o is the latitude relative to the equator and λ_o is the longitude relative to the Greenwich meridian (hence west longitudes are negative). Assuming the earth is a perfect sphere, then the orthodrome (or great circle arc) from X_o to an arbitrary point $X_2(\phi_2, \lambda_2)$ has a length d defined in Fig. 4.4 as

$$d = a \, \cos^{-1}[\sin\phi_o\sin\phi_2 + \cos\phi_o\cos\phi_2\cos\Delta\lambda] \qquad (4.4)$$

where a is the earth's radius (6371 km) and $\Delta\lambda = \lambda_2 - \lambda_o$.

The problem, given X_o and $d = r_i$, is to determine X_2. For a unique solution, the azimuth (the angular deflection α of the orthodrome measured clockwise from the meridian λ_o) must also be imposed.

With reference to Fig. 4.4, the angle θ subtended by the arc d is

$$\theta = \frac{d}{a} \qquad (4.5)$$

The law of cosines for a spherical triangle may then be invoked to specify the latitude of X_2 as

$$\phi_2 = \sin^{-1}[\cos\theta\sin\phi_o + \sin\theta\cos\phi_o\cos\alpha] \qquad (4.6)$$

Applying the law of sines to the azimuth angle α yields the specification of the longitude of X_2 as

$$\lambda_2 = \lambda_o + \sin^{-1}\left[\frac{\sin\alpha\sin\theta}{\cos\phi_2}\right] \qquad (4.7)$$

In other words, an isobar P_i at radial distance r_i from X_o may be discretized in latitude-longitude coordinates as a function of azimuth angle α.

In this application, the circumference C of the isobaric contour was divided into 2M elements such that the arc length between discretization points could not exceed a minimum length. Taking advantage of symmetry about the meridian λ_o, α was varied from $\Delta\alpha$ to $M\Delta\alpha$ radians where $\Delta\alpha = \pi/M$. In all cases two additional points were added at $\alpha = 0$ and $\alpha = \pi$. At the same time, at least 12 points were required to define each isobaric contour. These numbers were chosen to correspond roughly to the rate of digitization of a standard AES
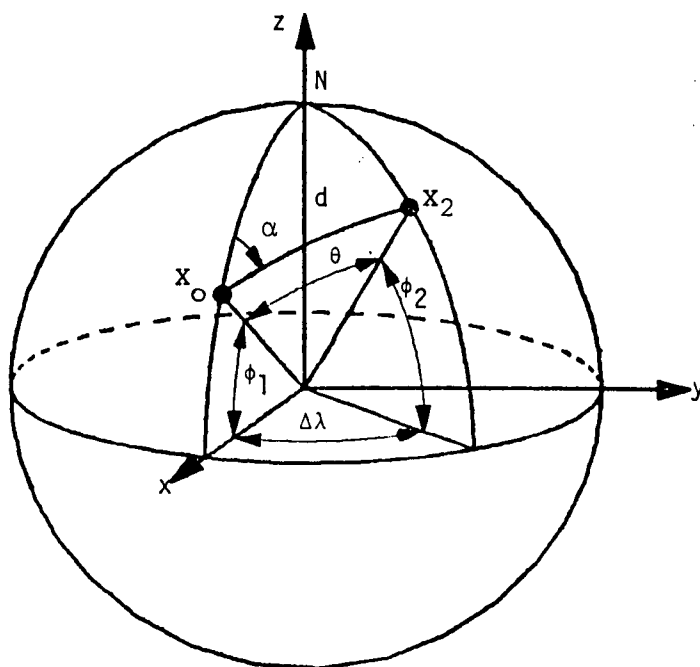
Fig. 4.4   Parameters defining distance between arbitrary points on a sphere. (From Pearson, 1984).
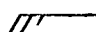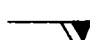
surface pressure chart.

The trajectory of X_o was defined as a function of time at discrete latitude-longitude positions. The speed of translation is readily calculated for any segment of the path as $v=d/\Delta t$ using (4.4) to calculate d.

4.2.2 Gradient and Surface Wind Fields
The gradient wind field, also known as the free atmosphere wind field, is calculated from the gradient of the surface pressure distribution. The basis of the computation is a force balance among pressure gradient, Coriolis and a centrifugal force term due to curvature of the isobars. This gradient wind is assumed to be at 500 m elevation, above the influence of the atmospheric boundary layer.

The gradient wind is reduced to an arbitrary near-surface elevation z using a boundary layer model based on the work of Delage (1985) at the Canadian Meteorological Centre and Yamada (1976). As discussed in Section 2.3.3, the method determines u_* as a function of the gradient wind, upper air and sea temperatures, and an empirical surface roughness length. Wind at a specific elevation z is then calculated from u_* using empirical profiles, the form of which depend on air column stability. In this application the near-surface reference level is z=10 m and neutral stability is imposed. This wind field which is denoted by U_{10} is calculated on a $1^o x 1^o$ latitude-longitude grid that encompasses the domain of the wave model. Fig. 4.5 shows an example of a surface pressure map and the corresponding U_{10} field. Isobars are drawn at 1 mb spacing and the wind vectors are drawn in the standard meteorological convention in which each full feather represents 10 knots, each half feather is 5 knots and the "v" feather is a shorthand for 50 knots. Direction of the wind is from the feathers to the head of the vector. Thus, for example,

$\overline{//\!\!/}$ means 25 knots from the west and

$\underline{}_{\mathbf{\backslash\!\backslash}}$ means 60 knots from the east.

4.3 Wave Model and Grid Setup
The study area for modelling purposes is bounded by $39^o N$ on the south, by $60^o N$ on the north, by $160^o W$ on the west and by $124^o W$ on the east. The spatial discretization is in 1° latitude and 1° longitude increments giving a grid which is 37 by 22 elements. At each of these points the energy spectrum $F(f,\theta)$ is determined at each model time step. The mapping of the model domain on a polar stereographic projection of the northeast Pacific Ocean is shown in
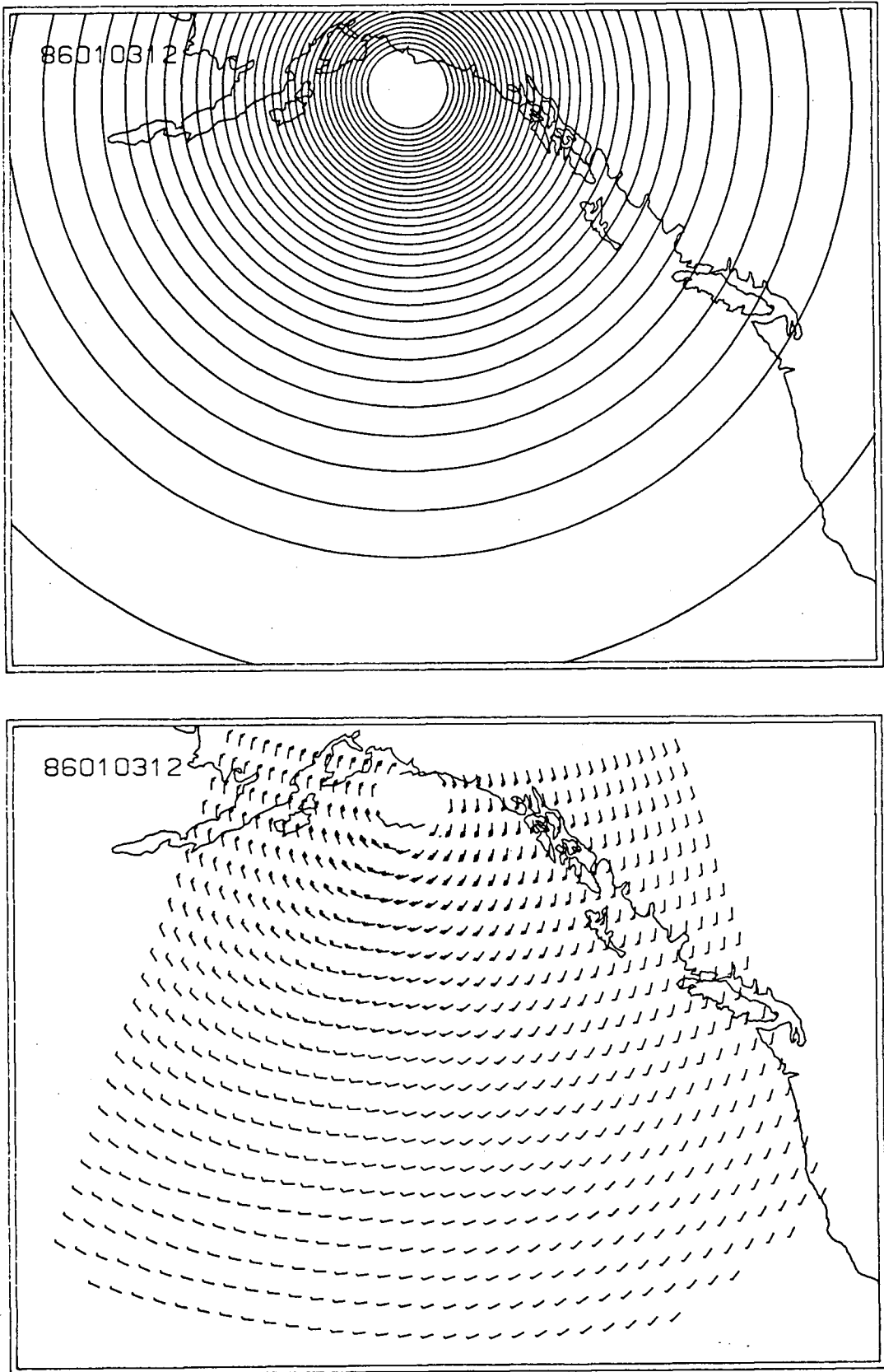
Fig. 4.5   A typical idealized pressure field (upper panel) and its
corresponding surface wind (U_{10}) field (lower panel).

Fig. 4.6. The resolution of the coastline is necessarily coarse and would not be suitable for hindcasting of wave climate near the coast.

Because the majority of the calculation points are in deep water, optional calculation of shoaling and refractive effects in shallow water have been omitted, although these effects would have to be included for accurate hindcast modelling of nearshore sea-states. The deep water configuration on a coarse grid is the typical first step in coastal wave modelling; spectral values calculated at the edge of the shelf break become the input boundary conditions for a finer mesh, shallow water calculation along the coast. Modelling in very shallow water or in regions of complex bathymetry may require a third, yet finer grid.

Directional resolution was fixed at 16 angles ($\Delta\theta = 2\pi/16 = 22.5°$). Frequency was parameterized in 16 equal frequency classes such that $f_{min} = 0.030$ Hz (T=32.8 s), $\Delta f = 0.0113$ Hz and $f_{max} = 0.2$ Hz (T=5.0 s).

Using linear wave theory and deep water approximations, the longest period wave of 33 s will have a group velocity c_g of $gT/4\pi$ or 26 m/s. Since the smallest grid element length is about 57 km, the maximum time step for computational stability of the propagation scheme is $57\times10^3/26 = 2192$ s. As a result, a convenient time step of 1800 s (0.5 h) was selected.

Time-series output of H_s, T_p, $\bar{\theta}$, E(f) and F(f,θ) was obtained at 11 special points designated in Fig. 4.6: four along the coast (including one wave buoy location in Queen Charlotte Sound marked by a star symbol), two parallel rows of three additional points each running southwest from the central coastal locations (including a U.S.A. deep ocean meteorological data buoy station), and a second deep ocean data buoy site off the Washington-Oregon coast. These time-series, obtained at hourly intervals, provide the first level of comparisons between the various case studies. Hourly output of the entire field of H_s, T_p and $\bar{\theta}$ was also made from which contoured maps of H_s were constructed to illustrate the overall development and evolution of the sea-state. To compare between certain input scenarios, fields of ΔH_s were contoured to highlight regions where the sea-state development was significantly different.
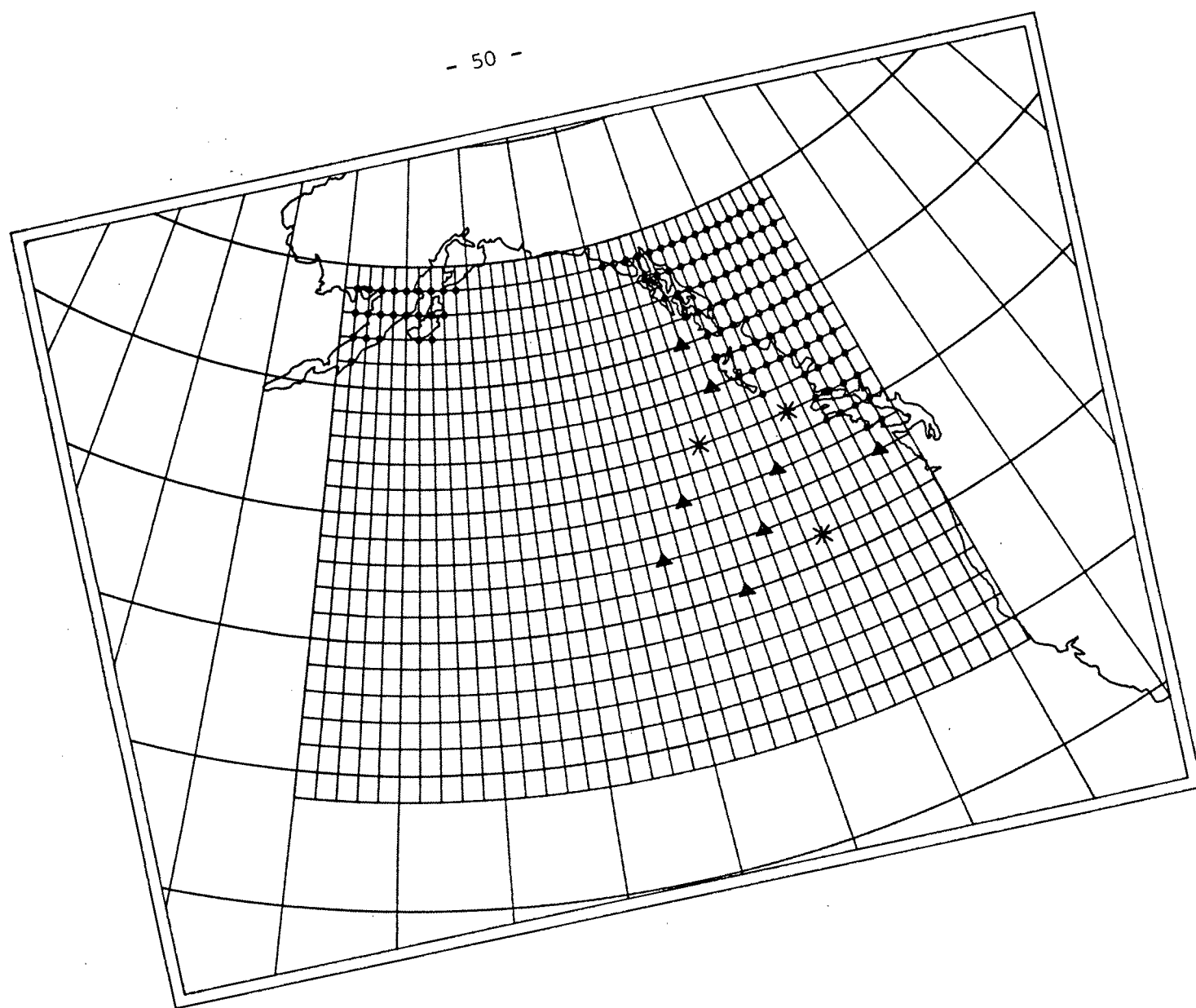
Legend: + land point

▲ special output point

✳ special output point
corresponding to an
historical wave buoy

Fig. 4.6   The wind and wave model grid showing the 1°x1° latitude-
longitude grid, the coastline representation , and the
special output points.

4.4 Pressure Parameter Specification

Recently, Lewis and Moran (1985) prepared a catalogue of severe storms in the northeast Pacific Ocean. From this document, it was possible to derive realistic mean or median and extreme values for the pressure parameters governing the surface pressure field evolution. Two meteorological storm classes were considered: the southwest frontal low and the southwest cold low as defined by Lewis and Moran.

Both usually occurred between October and March, but the frontal low is somewhat more common with 21 events in the 27 year database from 1957 to 1983. Waves generated by these storms are reportedly as great as 25 m with concurrent 16.5 m swell, although more typical reports are 8 to 10 m. Ship sinking or severe damage is known to have happened during five of these 21 storms. Many of the storm centres track fairly consistently from the west between the 40° and 45°N parallels and turn sharply to the north along 145°W, approximately, as sketched in Fig. 4.7a. The greatest storm intensification, as indicated by the lowest central pressure, is offshore of the Queen Charlotte Islands between 50° and 55°N. As the storms enter the Gulf of Alaska they usually begin to dissipate quite rapidly.

There were 14 southwest cold low storms in the 27 years studied by Lewis and Moran (1985). About half of these have a similar trajectory to the frontal lows as shown in Fig. 4.7b. These storms are generally less severe in terms of wave generation, although one did reportedly cause 20 m waves. One ship sinking has been attributed to this storm type, but ship-reported wave heights at the time were not especially large.

Clearly these are severe storms which must be a concern to Canada's west coast shipping and fishing industries. Fortunately, they are generally sufficiently far offshore that serious damage along the coast does not occur. Nevertheless, the nearshore wave climate resulting from such strong meteorological forcing will be very important in a comprehensive sea-state description for design purposes, especially for the exposed outer coast. Because they are recorded quite frequently, reasonable statistics of their major characteristics can be derived.
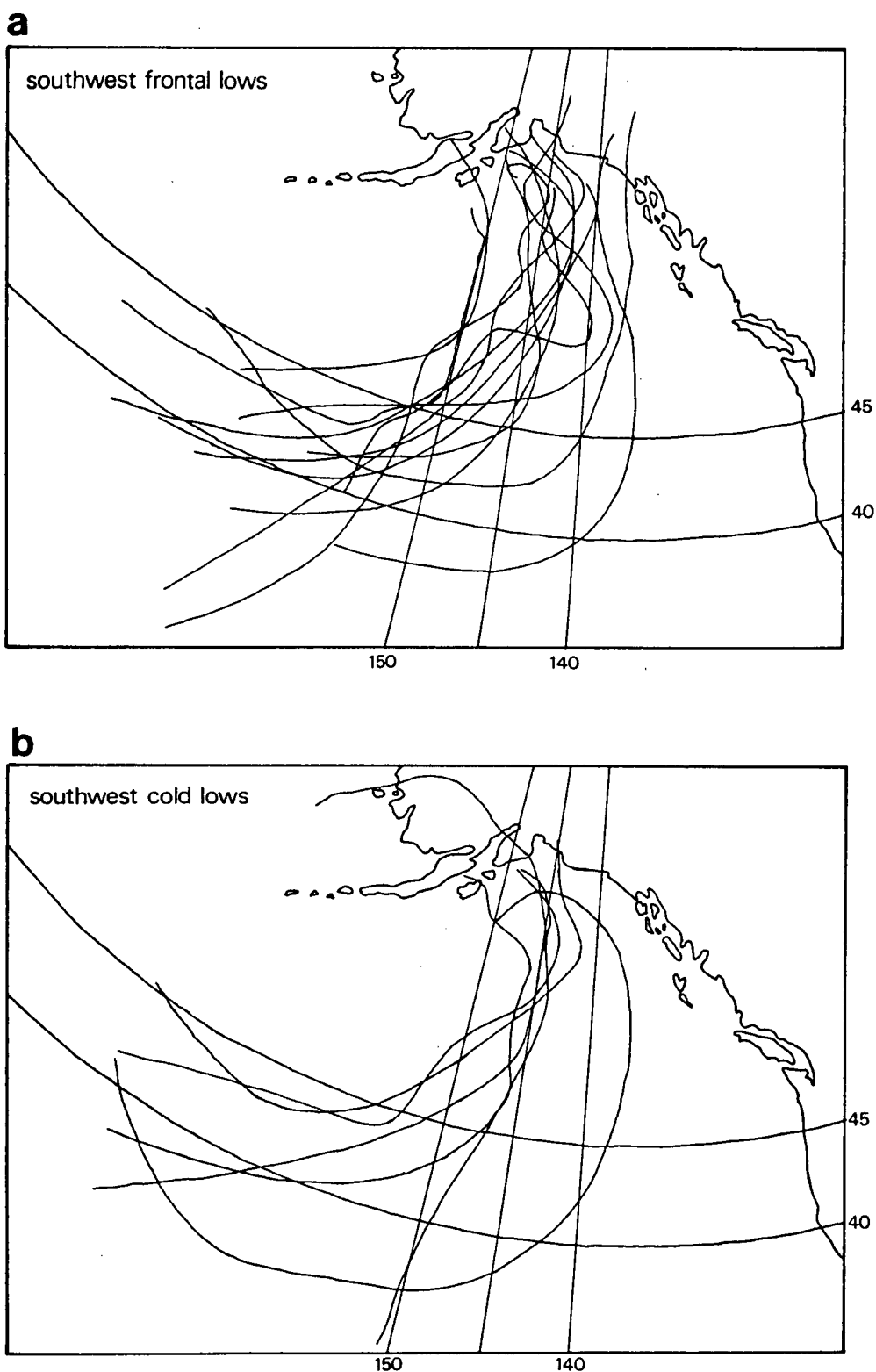
Fig. 4.7   The storm trajectories of (a) southwest frontal lows and
(b) southwest cold lows. (Adapted from Lewis and Moran,
1985).

4.4.1 Trajectory

These storms were idealized in terms of three segments illustrated in Fig. 4.8: a spin-up leg between the western model boundary (point A) and the point where the trajectory turns north (B), a storm intensification leg proceeding north to the location of minimum central low pressure (C), and a storm filling leg over which the central pressure increases as the storm approaches the northern edge of the model domain (D). The mean trajectory path was imposed from the west along 42°N (A to B) and thence north along 145°W (B to C to D). Variations within ±5° of the 145°W longitude are also realistic.

4.4.2 Central Pressure

The average minimum central low pressure based on the 21 southwest frontal and cold lows sketched in Fig. 4.7 is 958 mb for data ranging between the minimum record of 944 mb and the largest value of 970 mb. The median position (C) of this low pressure was imposed at 53°N 145°W, due west of the Queen Charlotte Islands.

At the western edge (A), the mean pressure of the 21 storms was 984 mb from data ranging between 954 and 1010 mb. At the northern edge (D), the mean central pressure was 970 mb with a minimum of 952 mb and a maximum of 982 mb. The values at point B are more difficult to specify since the trajectories (Fig. 4.7) vary greatly in this area. Instead, the mean rate of change of P_o between A and C was used to estimate a reasonable value at B. The average rate of deepening of the central pressure $\Delta P_o / \Delta t$ was determined to be approximately -0.6 mb/h which implies $P_o = 969$ mb at B for typical rates of storm translation.

4.4.3 Storm Speed

There are two aspects to storm speed: the rate of translation of the storm centre $\Delta X_o / \Delta t$ through the segments of the study area and the rate of development (or deepening) of the low pressure system $\Delta P_o / \Delta t$. The speed with which the storm moves depends on its stage of development (leg A-B, B-C or C-D). The final stage usually has the slowest movement and occasionally a storm system will become stationary in this area for up to 24 hours. Average speeds are on the order of 35 to 40 km/h which is the equivalent of 18 hours to move from the latitude of the Queen Charlotte Islands to the southern Alaskan coast. During the early storm formation in the southwestern region of the study area, typical speeds are 45 to 55 km/h between 160°W and 145°W along 42°N. The highest velocities occur during the intensification stage, averaging about 70 km/h. These speeds cannot be calculated very accurately
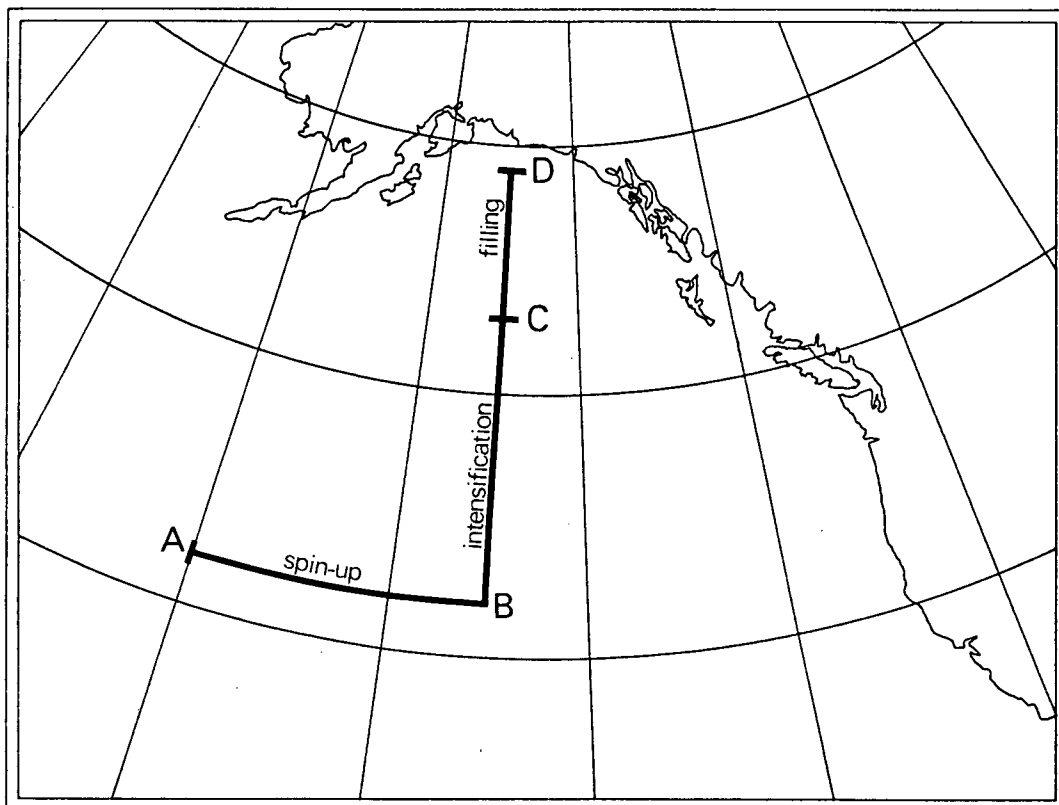
Fig. 4.8   The three segments of an idealized storm trajectory
           based on the southwest frontal lows and the southwest
           cold lows.

from the 12-hourly central pressure positions, but they do suffice for the development of the idealized wind field time-series.

The average rate of central pressure deepening $\Delta P_o/\Delta t$ is -0.6 mb/h. Occasionally, in 8 of the 21 storms, this rate exceeds -1 mb/h over a 12 hour period, and this situation is known as "explosive deepening" of the low pressure system. Since the winds strengthen so quickly, a very high sea-state can develop without much warning and many of these storms will be among the most severe affecting an offshore or outer coastal location. For the eight events containing a period of explosive deepening, the average rate was -1.8 mb/h. During one of these storms -3.3 mb/h intensification occurred followed by reports of 10 m local wind waves and 12.5 m swell waves.

4.4.4 Radial Scaling Parameter

Of all the storm characteristics, the radial scaling parameter R was the most subjectively determined due to limitations in the available data for the 21 storms. From inspection of the fully developed storm maps in Lewis and Moran (1985) and the evolution in time and space of a few other low pressure systems, it was determined that the physical dimension of these pressure patterns is more or less constant from the centre to the 990 mb isobar over the time history of a given system. For the 21 fully developed pressure maps, the average of this radial dimension $\bar{r}_{990}$ was about 8° of latitude (or 890 km), while the other data maps which were of very intense storms suggested $\bar{r}_{990}$ could be as small as 3 or 4° of latitude. A compromise of 6° of latitude was selected for substitution in (4.1) to determine R for each specific P_o since by rearrangement

$$R = -\bar{r}_{990} \ln \left[\frac{990 - P_o}{\Delta P} \right] \tag{4.8}$$

In essence then, because the radial dimension $\bar{r}_{990}$ was specified, R varies throughout a storm as a function of P_o. As a result, the sensitivity to R can only be tested indirectly through adjustment of $\bar{r}_{990}$.

4.5 Summary of Model Test Cases

4.5.1 Storm 1: The Median Base Scenario

A baseline storm was constructed against which to compare most other test cases. It was composed of the median trajectory from the west along 42°N turning north along 145°W with the average P_o values of 984 mb imposed at point A, 969 mb at point B, P_o(min) of 958 mb at point C (53°N 145°W) and 970 mb at point D. The average rate of deepening $\Delta P_o/\Delta t = -0.6$ mb/h was selected followed by a typical rate of filling with $\Delta P_o/\Delta t = +0.7$ mb/h.

The rate of storm advance along the trajectory path is not an independent parameter after the other variables are imposed. The resulting speeds $\Delta X_o/\Delta t$ are representative of the 21 storms that were analyzed from Lewis and Moran (1985). Table 4.1 summarizes the storm parameters.

Table 4.1

Storm 1 Scenario Parameters

Point	Leg	Latitude Longitude	Length (km)	Time YYMMDDHH	Duration (h)	$\Delta X_o/\Delta t$ (km/h)	P_o (mb)	$\Delta P_o/\Delta t$ (mb/h)
A		42°N 160°W		86010100			984	
	A-B		1238		24	52		-0.6
B		42°N 145°W		86010200			969	
	B-C		1223		18	68		-0.6
C		53°N 145°W		86010218			958	
	C-D		667		18	37		+0.7
D		59°N 145°W		86010312			970	

4.5.2 Storm 2: Explosive Deepening

The central pressures of storm 1 at points A, C and D were unchanged in storm 2, but $\Delta P_o / \Delta t$ was adjusted along legs A-B and B-C so that in the 12 hours preceding the achieving of P_o(min) at point C the rate of deepening was -1.8 mb/h. This was the average explosive deepening rate in the 8 case storms discussed in Section 4.4.3. Table 4.2 contains the complete specification of the pressure parameters.

Table 4.2

Storm 2 Scenario Parameters

Point	Leg	Latitude Longitude	Length (km)	Time YYMMDDHH	Duration (h)	$\Delta X_o / \Delta t$ (km/h)	P_o (mb)	$\Delta P_o / \Delta t$ (mb/h)
A		42^oN 160^oW		86020100			984	
	A-B		1238		24	52		-0.2
B		42^oN 145^oW		86020200			980	
	B-C		1223		18	68		-1.2 (avg.) -1.8 (max.)
C		53^oN 145^oW		86020218			958	
	C-D		667		18	37		+0.7
D		59^oN 145^oW		86020312			970	

4.5.3 Storm 3: Easterly Shifted Northward Trajectory

As illustrated in Fig. 4.7, the B-C-D portion of the storm trajectory can easily be 5° closer to the B.C. coastline. Storm 3 was used to investigate the effect of this eastward translation by simply moving point B and the subsequent storm path from 145°W in storm 1 to 140°W in storm 3. Table 4.3 summarizes the resulting pressure parameters and confirms that the only other consequential variation from storm 1 is a small increase in $\Delta X_o/\Delta t$ in leg A-B.

Table 4.3
Storm 3 Scenario Parameters

Point	Leg	Latitude Longitude	Length (km)	Time YYMMDDHH	Duration (h)	$\Delta X_o/\Delta t$ (km/h)	P_o (mb)	$\Delta P_o/\Delta t$ (mb/h)
A		42°N 160°W		86030100			984	
	A-B		1649		24	69		-0.6
B		42°N 140°W		86030200			969	
	B-C		1223		18	68		-0.6
C		53°N 140°W		86030218			958	
	C-D		667		18	37		+0.7
D		59°N 140°W		86030312			970	

4.5.4 Storm 4: Increased Radial Extent

Storm 4 has the same trajectory, central pressure history and speed of translation as storm 1, but the radial extent was increased from $\bar{r}_{990}=6°$ to $8°$ of latitude. The effect of this change is, on average, to reduce $\Delta P/\Delta r$ and hence reduce the wind speeds. As discussed in Section 4.4.4, $8°$ was the average radius of the 990 mb isobar in the 21 fully developed pressure maps from Lewis and Moran (1985) that were studied. The storm scenario parameters are repeated from Table 4.1 in Table 4.4.

Table 4.4

Storm 4 Scenario Parameters

Point	Leg	Latitude Longitude	Length (km)	Time YYMMDDHH	Duration (h)	$\Delta X_o/\Delta t$ (km/h)	P_o (mb)	$\Delta P_o/\Delta t$ (mb/h)
A		$42°N$ $160°W$		86040100			984	
	A-B		1238		24	52		-0.6
B		$42°N$ $145°W$		86040200			969	
	B-C		1223		18	68		-0.6
C		$53°N$ $145°W$		86040218			958	
	C-D		667		18	37		+0.7
D		$59°N$ $145°W$		86040312			970	

4.5.5 Storm 5: Advection Rate (Stalled Weather System in the Gulf of Alaska)

Storm 5 is identical to storm 1 until day 03 hour 00 which is 6 hours past point C in the trajectory. At this point (55°N 145°W) the system remains constant in character and stationary for 24 hours. It then proceeds north in the same manner as storm 1. Table 4.5 describes the characteristics of this storm.

Table 4.5

Storm 5 Scenario Parameters

Point	Leg	Latitude Longitude	Length (km)	Time YYMMDDHH	Duration (h)	$\Delta X_o / \Delta t$ (km/h)	P_o (mb)	$\Delta P_o / \Delta t$ (mb/h)
A		42°N 160°W		86050100			984	
	A-B		1238		24	52		-0.6
B		42°N 145°W		86050200			969	
	B-C		1223		18	68		-0.6
C		53°N 145°W		86050218			958	
	C-stall		222		6	37		+0.7
stall		55°N 145°W		86050300 86050400	24	0	962	0.0
	stall-D		445		12	37		+0.7
D		59°N 145°W		86050412			970	

4.5.6 Storm 6: Deepest Central Low

In this scenario the minimum central pressure imposed at the same point C (53°N 145°W) was set to the minimum recorded P_o(min) among the storms illustrated in Fig. 4.7 which was 944 mb. The rate of deepening along leg B-C and the rate of filling along leg C-D were adjusted to keep the values of P_o at points B and D nearly equal to those in storm 1. The resulting rate of deepening was -1.3 mb/h between B and C and the rate of filling doubled to $+1.4$ mb/h. The character of this storm is, therefore, a rapid development of a very intense low pressure system followed by very rapid dissipation as described by Table 4.6.

Table 4.6

Storm 6 Scenario Parameters

Point	Leg	Latitude Longitude	Length (km)	Time YYMMDDHH	Duration (h)	$\Delta X_o / \Delta t$ (km/h)	P_o (mb)	$\Delta P_o / \Delta t$ (mb/h)
A		42°N 160°W		86060100			984	
	A-B		1238		24	52		-0.7
B		42°N 145°W		86060200			968	
	B-C		1223		18	68		-1.3
C		53°N 145°W		86060218			944	
	C-D		667		18	37		$+1.4$
D		59°N 145°W		86060312			970	

4.5.7 Storm 7: Highest Minimum Central Pressure

In storm 7 the minimum central pressure deepens only as far as 974 mb. This was the highest value among the 21 storms illustrated in Fig. 4.7. However, the prototype storm system was still responsible for creating storm force winds which are defined by Lewis and Moran (1985) as a wind speed exceeding 48 knots (i.e. Beaufort scale 10 or greater). In the idealized scheme, the system did not deepen at all in leg A-B and then P_o decreased by about -0.6 mb/h to the 974 mb minimum at point C and did not fill in leg C-D. The details of this scenario are listed in Table 4.7.

Table 4.7

Storm 7 Scenario Parameters

Point	Leg	Latitude Longitude	Length (km)	Time YYMMDDHH	Duration (h)	$\Delta X_o/\Delta t$ (km/h)	P_o (mb)	$\Delta P_o/\Delta t$ (mb/h)
A		42°N 160°W		86070100			984	
	A-B		1238		24	52		0.0
B		42°N 145°W		86070200			984	
	B-C		1223		18	68		-0.6
C		53°N 145°W		86070218			974	
	C-D		667		18	37		0.0
D		59°N 145°W		86070312			974	

4.5.8 Storm 8: Idealization of the February 5-7, 1960 Storm

The storm of February 5-7, 1960 is the one in which P_o(min) reached the lowest recorded value of 944 mb among the 21 storms extracted from Lewis and Moran (1985). It constitutes quite a severe storm, especially since the minimum pressure was reached very early in the trajectory. Fig. 4.9 shows the weather system on February 6 at 12Z and the history of its central pressure in terms of X_o and P_o at 12 hour intervals. The idealized storm is presented in the same terms in Fig. 4.10. The synthetic version reaches its P_o(min) at a point 6 hours _west_ of point B and remains constant at this low value for 24 h as the storm progresses along the trajectory of storm 1 (and 6). The rate of advance of the idealized low pressure system is fairly steady at about 50 km/h throughout its history as seen in Table 4.8.

One other difference between storm 8 and the other test cases is that the maximum pressure change is only 20 mb of deepening in storm 8 since it is already significantly deepened at the western edge of the study domain. On the other hand, P_o(min) is followed by 20 mb of filling. By comparison, storm 1 deepens by 26 mb but fills by only 12 mb.

The duration of storm 8 is 6 hours longer than storm 1 and point C is defined to be at the same time in the two storms (day 02 hour 18) but it is positioned 3° of latitude further south in storm 8.

Table 4.8
Storm 8 Scenario Parameters

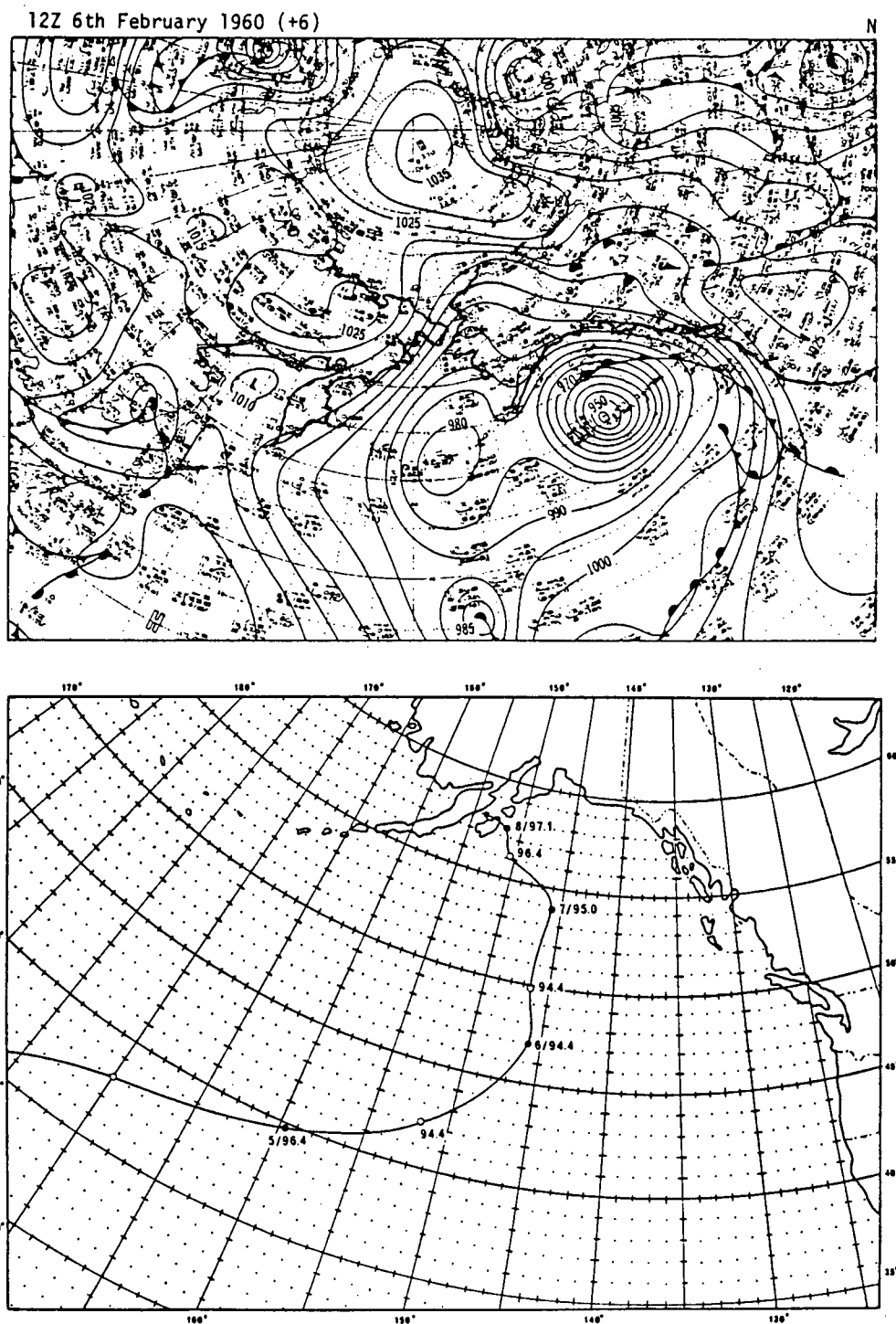| Point	Leg	Latitude Longitude	Length (km)	Time YYMMDDHH	Duration (h)	$\Delta X_o/\Delta t$ (km/h)	P_o (mb)	$\Delta P_o/\Delta t$ (mb/h)
A		42^oN 160^oW		86080100			964	
	A-P_o(min)		908		18	50		-1.1 (avg.) -1.7 (max.)
P_o(min)		42^oN 149^oW		86080118			944	
	P_o(min)-B		331		6	55		0.0
B		42^oN 145^oW		86080200			944	
	B-C		890		18	49		0.0
C		50^oN 145^oW		86080218			944	
	C-D		1001		24	42		+0.8
D		59^oN 145^oW		86080318			964	

Fig. 4.9   The surface pressure chart for February 6, 1960 at 12Z
at the peak of the storm (upper panel) and the storm
trajectory (lower panel) with 12-hourly central
pressures (kPa). (From Lewis and Moran, 1985).

```
P(i) =    949. mb    R(i) =    146. km
P(i) =    954. mb    R(i) =    197. km
P(i) =    959. mb    R(i) =    248. km
P(i) =    964. mb    R(i) =    305. km
P(i) =    969. mb    R(i) =    370. km
P(i) =    974. mb    R(i) =    448. km
P(i) =    979. mb    R(i) =    546. km
P(i) =    984. mb    R(i) =    675. km
P(i) =    989. mb    R(i) =    847. km
P(i) =    994. mb    R(i) =   1101. km
P(i) =    999. mb    R(i) =   1512. km
```
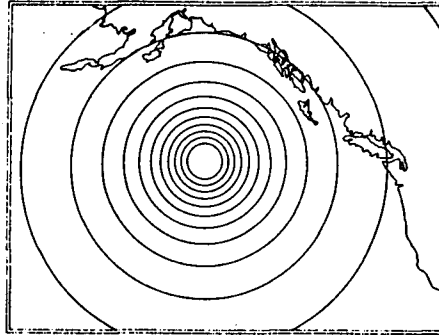
Storm 8

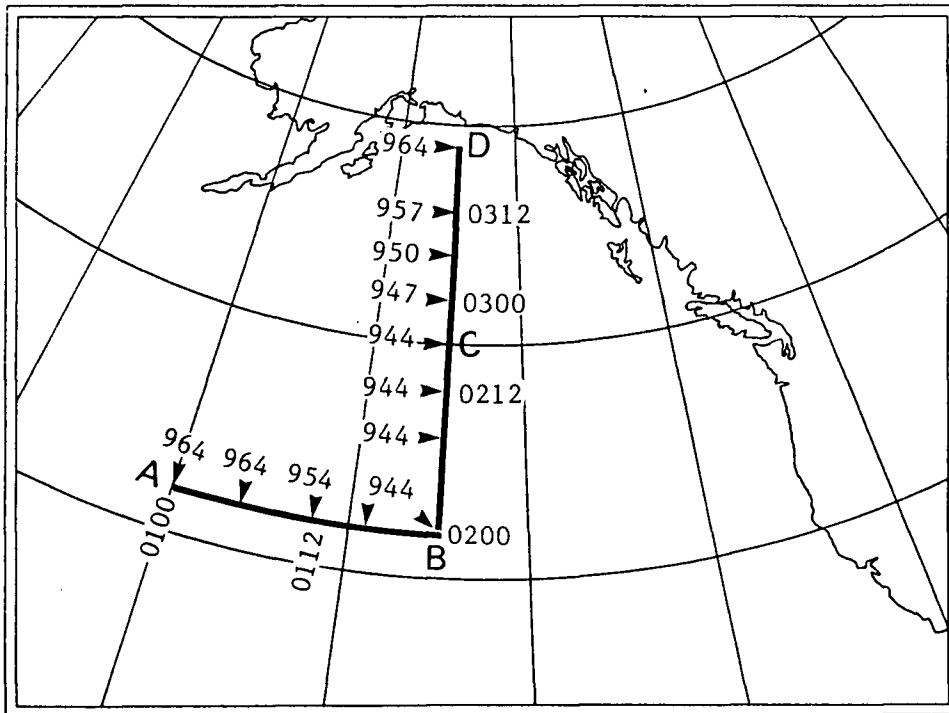Fig. 4.10   Idealization of the surface pressure chart corresponding
to February 6, 1960 at 12Z (upper panel) and the storm
trajectory (lower panel) at roughly the same scales as
the actual storm data in Fig. 4.9.

5.0   DISCUSSION OF SENSITIVITY ANALYSIS RESULTS

5.1   The Base Scenario

Storm 1 is the base scenario against which most other cases are compared. The characteristics of its pressure field were selected to represent average conditions for a severe winter storm. Maximum wind speeds at the peak of the event are 60 knots as shown in Fig. 5.1. The 6-hourly time-series of significant wave height fields is presented in Fig. 5.2 from the end of the spin-up period (P_o centred at point B of the storm trajectory) to the end of the simulation 36 hours later (P_o centred at point D). Sea-states exceeding 9 m are present from day 02 hour 12 to the end of the sequence on day 03 hour 12. The maximum H_s is about 10 m on day 03 hour 00 which is 6 h after the storm winds are maximum.

Along the west coast of British Columbia, waves arrive from the southwest. As a result, the sea-state evolves from a fairly uniform H_s of 0.5 to 1.0 m to a gradient increasing from about 1.8 m near Tofino to 4.5 m at the north end of the Queen Charlotte Islands over a 24 hour period beginning on day 01 hour 12.

Fig. 5.3 shows the $(H_s, T_p, \bar{\theta})$ history at the site in the entrance to Queen Charlotte Sound. At this location, the maximum wind speed is about 15 knots from the south from day 02 hour 12 to day 03 hour 00; thereafter wind speed diminishes and shifts progressively more southwesterly. Under such light forcing, H_s will not exceed about 1.5 m assuming a steady wind for 12 hours with unrestricted fetch (Bretschneider nomogram in U.S. Army, 1977). The abrupt increase in T_p on day 03 at about 03 hours in Fig. 5.3 and the corresponding increase in H_s is due to swell propagating shoreward from the generation region on the southeastern side of the storm system as it was positioned about 15 hours previously. This finding highlights the importance of swell energy to the correct hindcasting of the coastal wave regime.
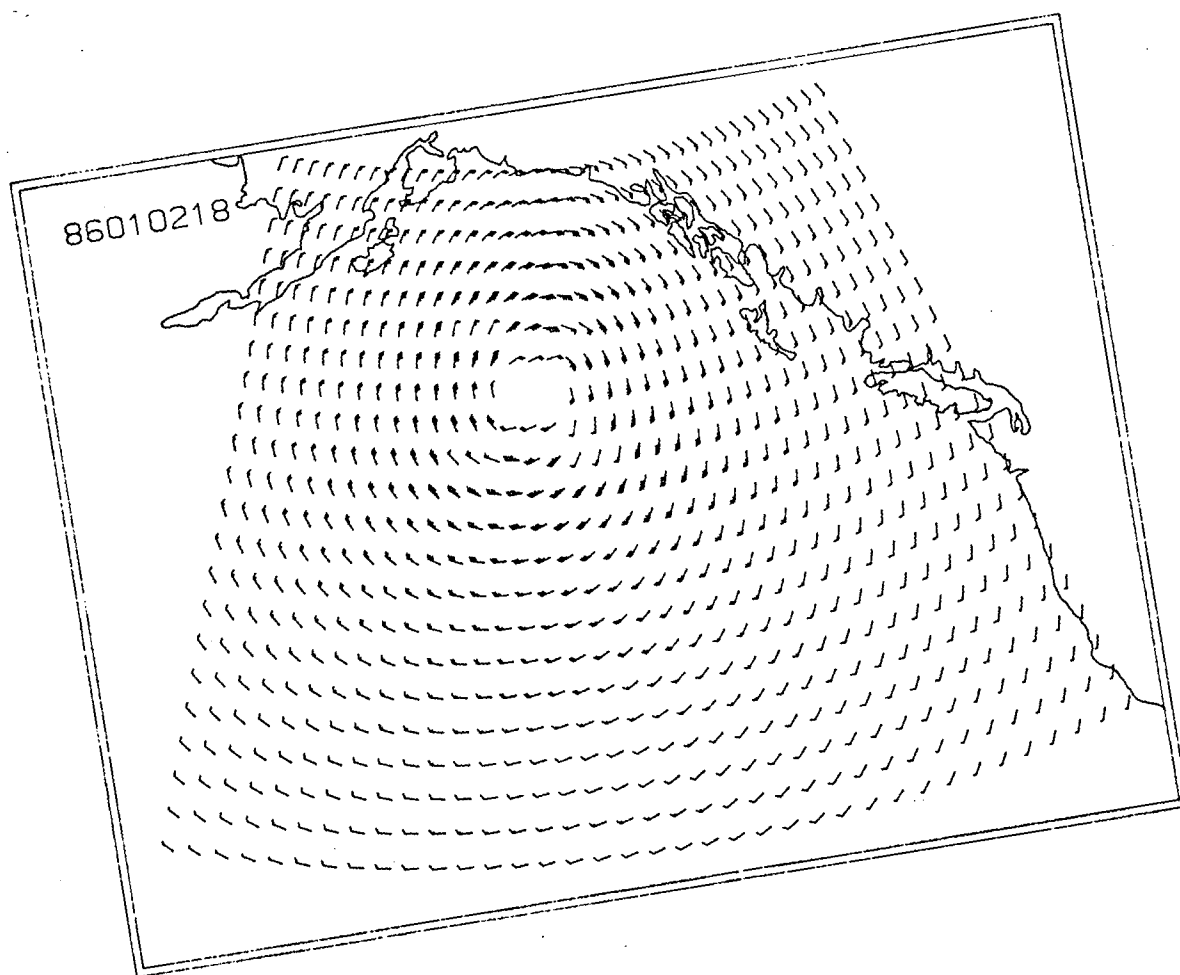
86010218

Fig. 5.1   Peak wind field for storm 1 showing maximum winds of 60 knots.
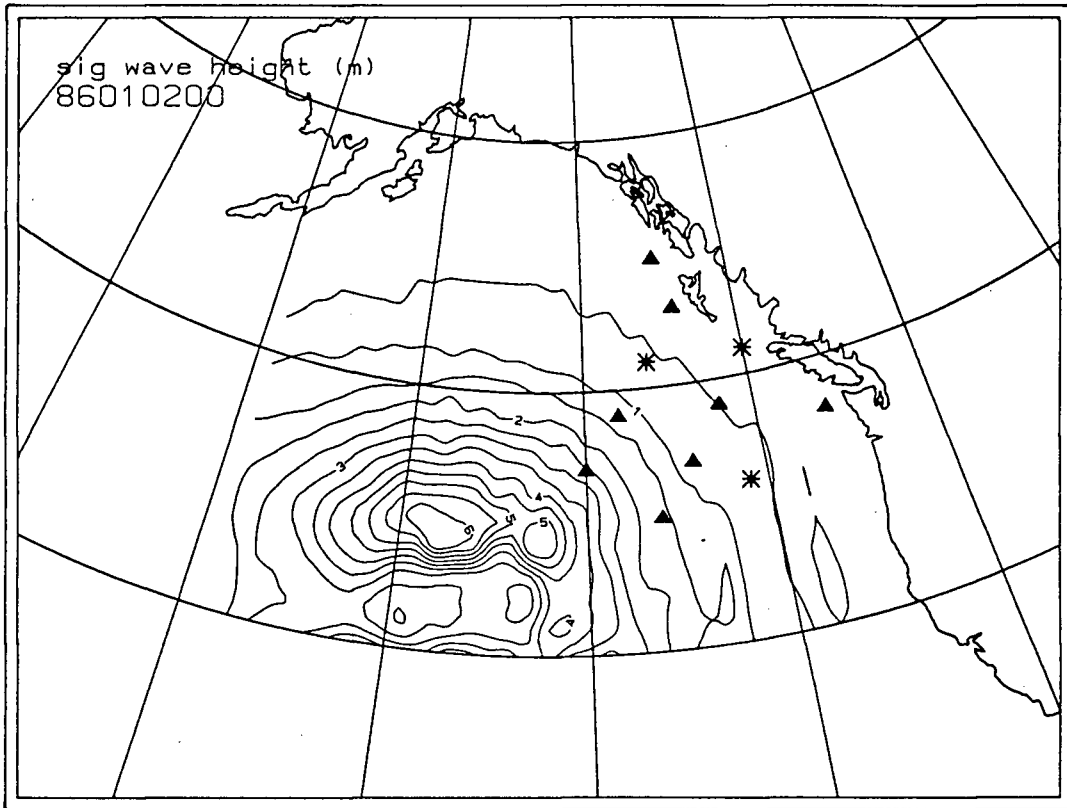
Fig. 5.2   Six-hourly significant wave height fields produced by
            storm 1 along legs B-C and C-D of the storm trajectory.
            The peak of the storm winds occurs at 86010218 (day 02
            hour 18) in the fourth panel; the maximum waves are six
            hours later at 86010300 (day 03 hour 00).

Fig. 5.2   Continued.

sig wave height (m)
86010218

sig wave height (m)
86010300

Fig. 5.2   Continued.
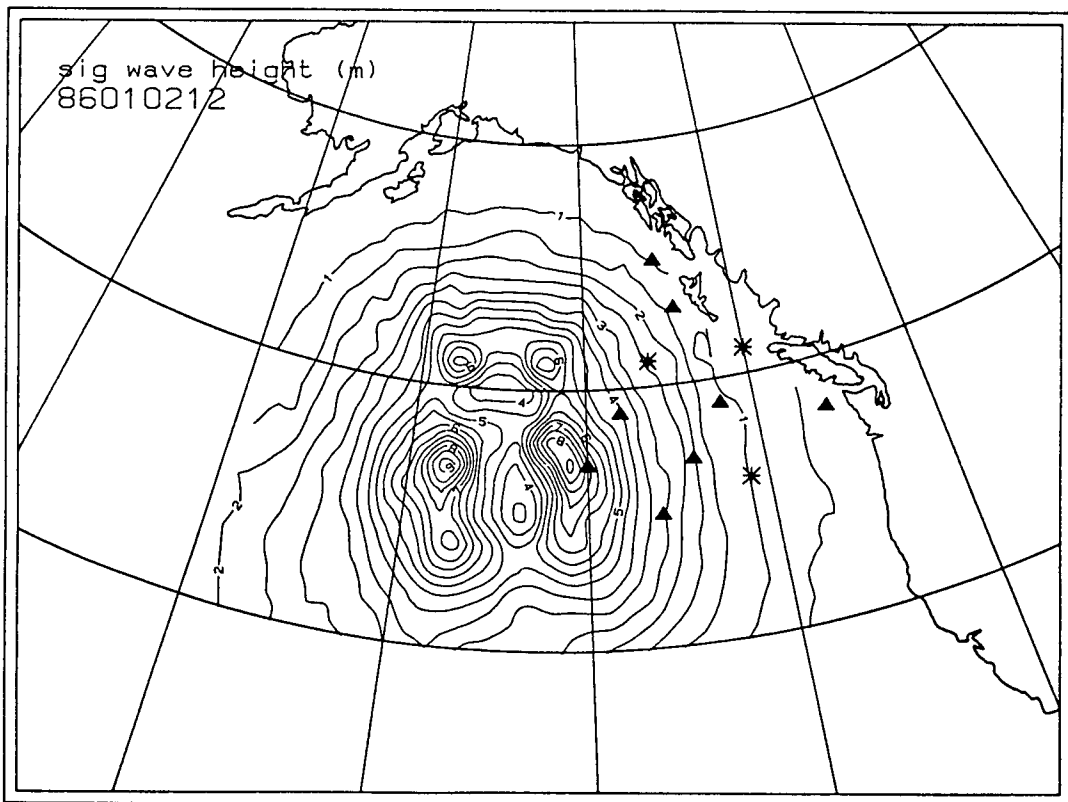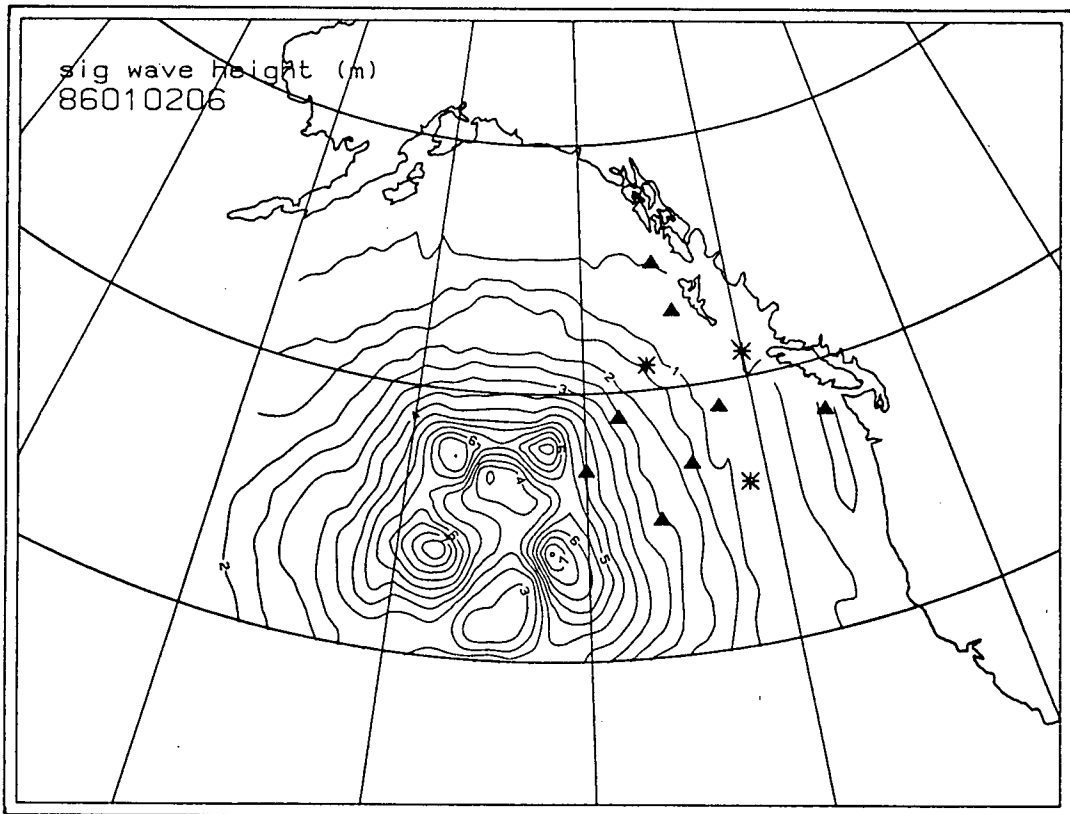
sig wave height (m)
86010306
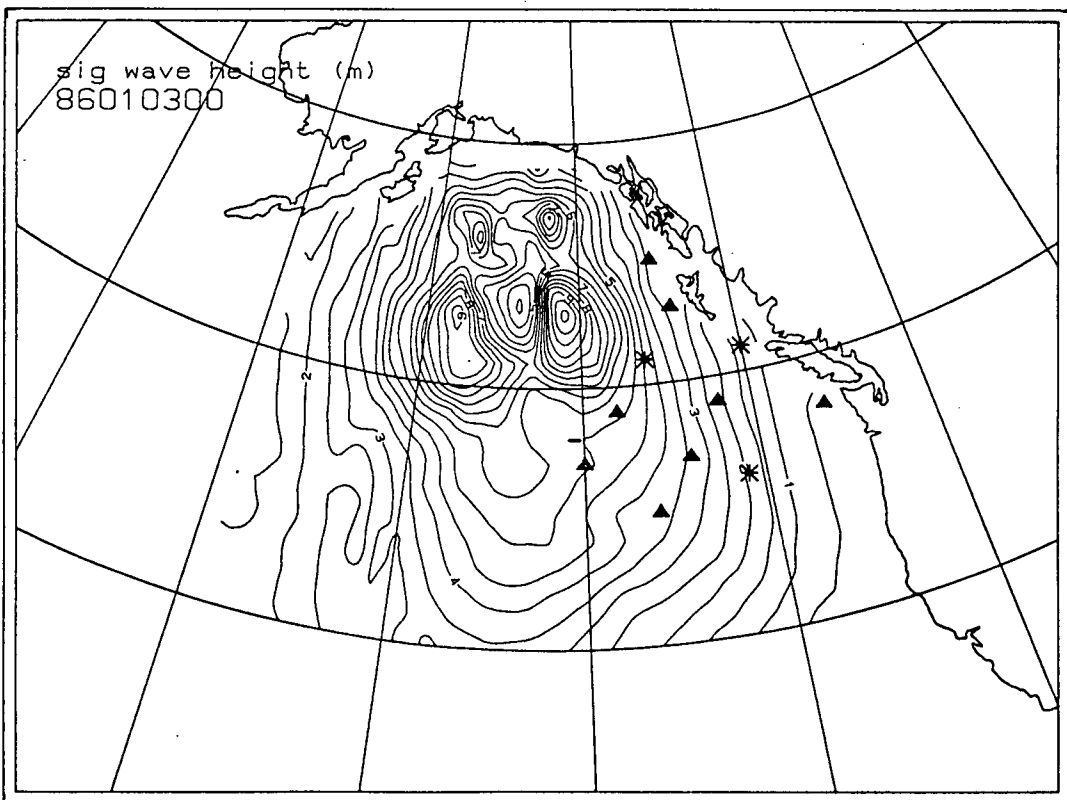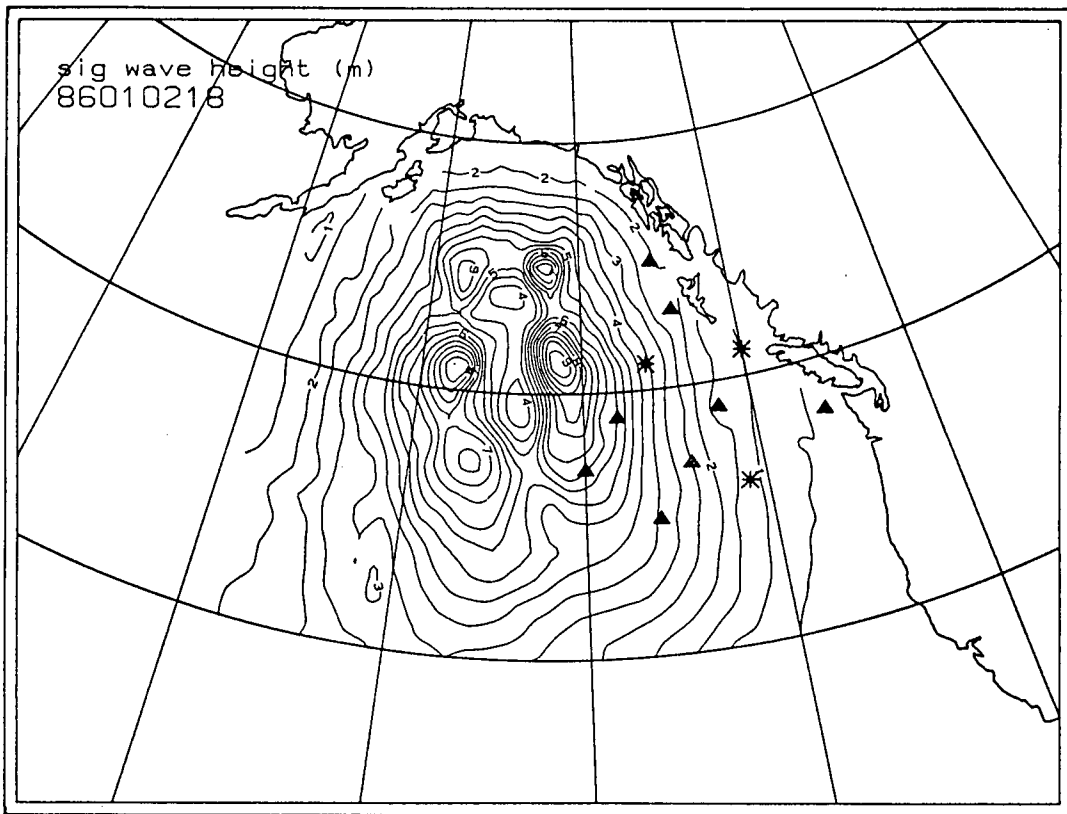
sig wave height (m)
86010312

Fig. 5.2   Continued.

Storm 1   Queen Charlotte Sound

                                     _____ (31,13)

Fig. 5.3   Time-series of significant wave height (H_s), peak period
            (T_p) and mean wave direction at the special output point
            at the entrance to Queen Charlotte Sound (model grid co-
            ordinates (31,13)) during storm 1.

5.2   Storm Intensity Variations

Storm 2 tests the effect of more rapid development of an equally intense storm as measured by $P_o(min)$. In essence, this scenario has a spin-up of a diminished intensity followed by a short period of explosive deepening as illustrated in Fig. 5.4. The expectation is, therefore, that the early sea-state development will be retarded and maximum sea-states will be less high than in storm 1. If the local seas are roughly in equilibrium with local winds, the difference in the field of H_s by the end of the slow moving C-D leg should not be very great. Because the early development is weaker, coastal swell energy should not be as great as in storm 1.

Fig. 5.5 shows the difference in the H_s field every 6 hours from day 02 hour 06 at the beginning of the explosive deepening until day 03 hour 00 which is 6 hours after the end of the deepening to $P_o(min)$ and which corresponds to the time of maximum H_s values in storm 1. The difference ΔH_s is calculated as H_s(storm 2) minus H_s(storm 1) so that negative differences indicate a region wherein the sea-state of storm 2 is less than that of storm 1. In this case, the largest differences are somewhat greater than 5 m. Comparison with Fig. 5.2 indicates that these differences are coincident with the highest sea-state areas where H_s(storm 1) is on the order of 7.5 to 8.0 m. As storm 2 develops, the differences diminish to about 3.5 m by the storm peak on day 02 at hour 18. Futhermore, the largest differences are no longer coincident with peak H_s regions. By day 03 hour 00, there is virtually no difference in the area of local wind generation north of about 50^oN. South of this latitude is a broad region in which H_s is 1 to 2 m less. This results in swell energy of about 2 m lower significant wave height 12 hours later along the coast. This finding is illustrated by the Queen Charlotte Sound site in Fig. 5.6.

At the coastal site north of the Queen Charlotte Islands there is virtually no difference in the time-series response between storm scenarios 1 and 2 (Fig. 5.7). This is because the site is well-sheltered during the early stages of the storm development (i.e. offshore winds) and there can be little swell energy arriving at this site until the storm has passed this northerly latitude.
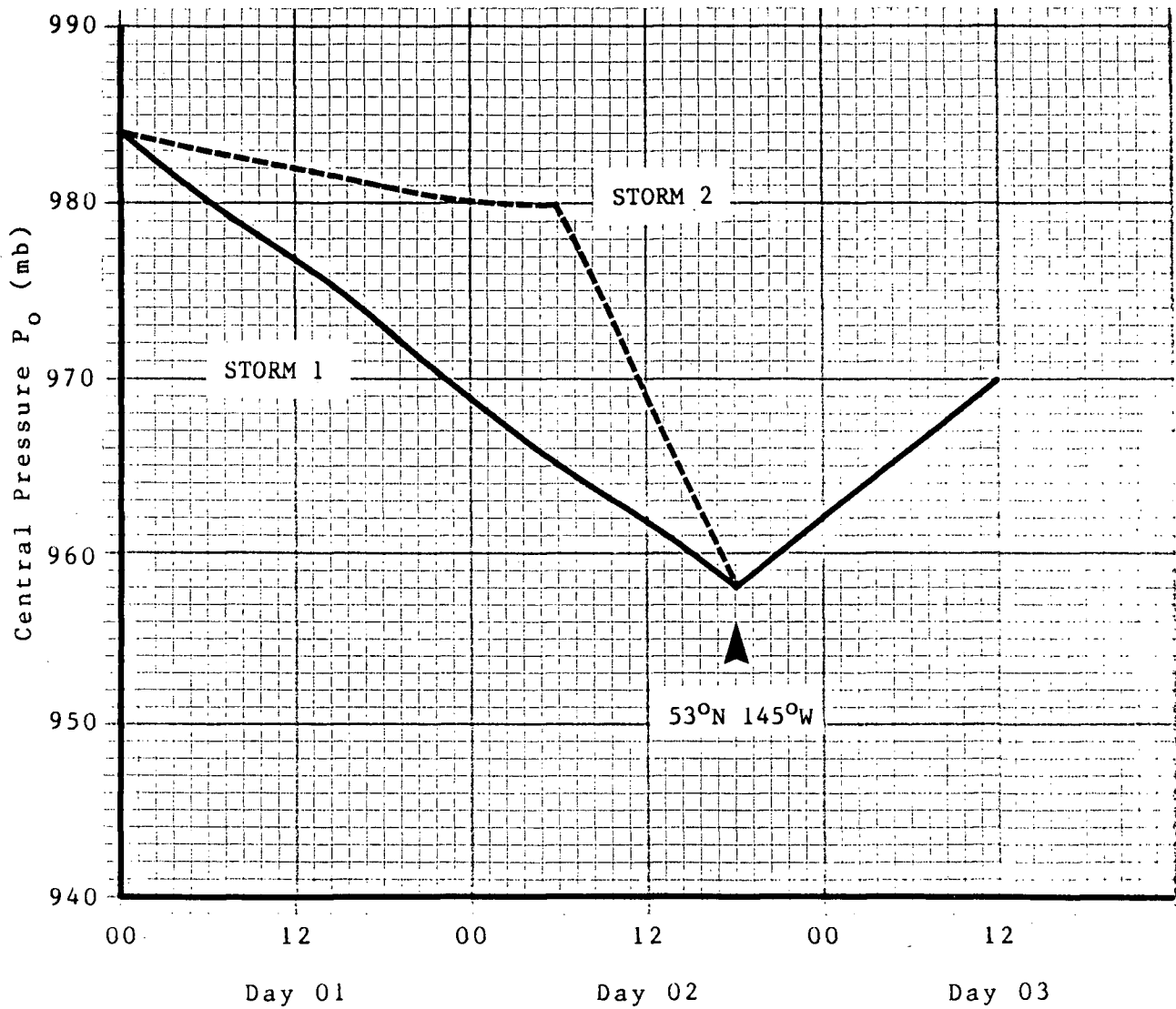
Fig. 5.4   The evolution of P_O in storms 1 and 2.
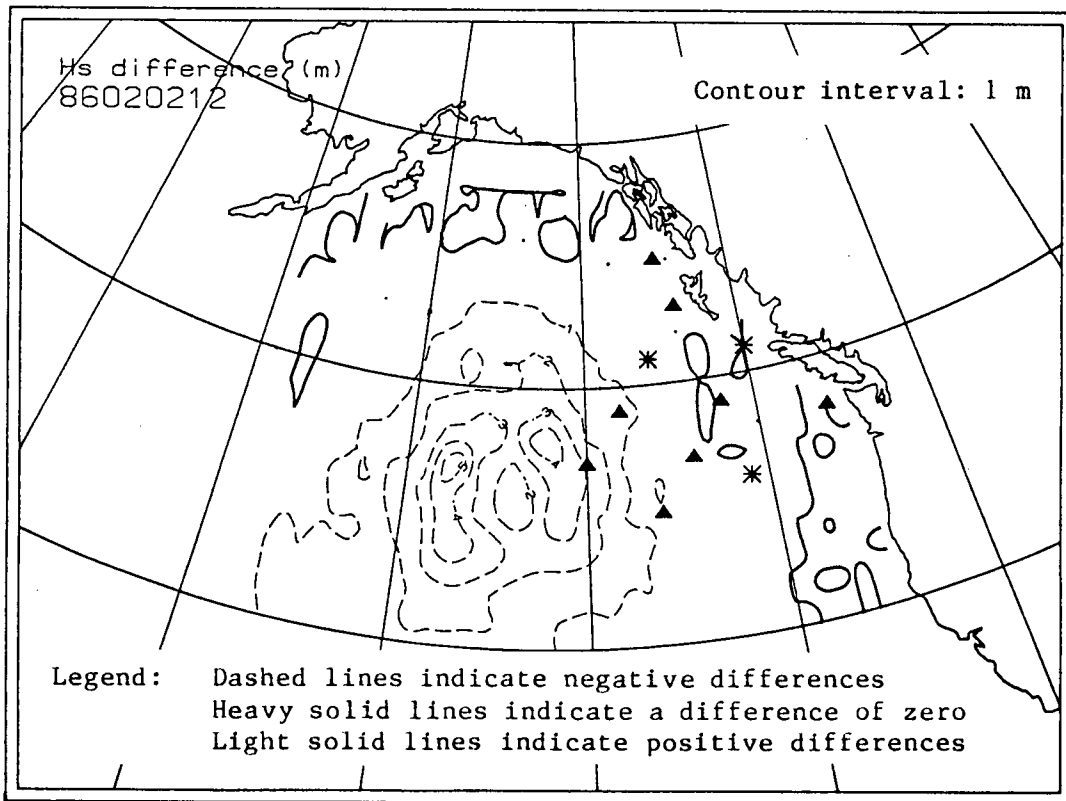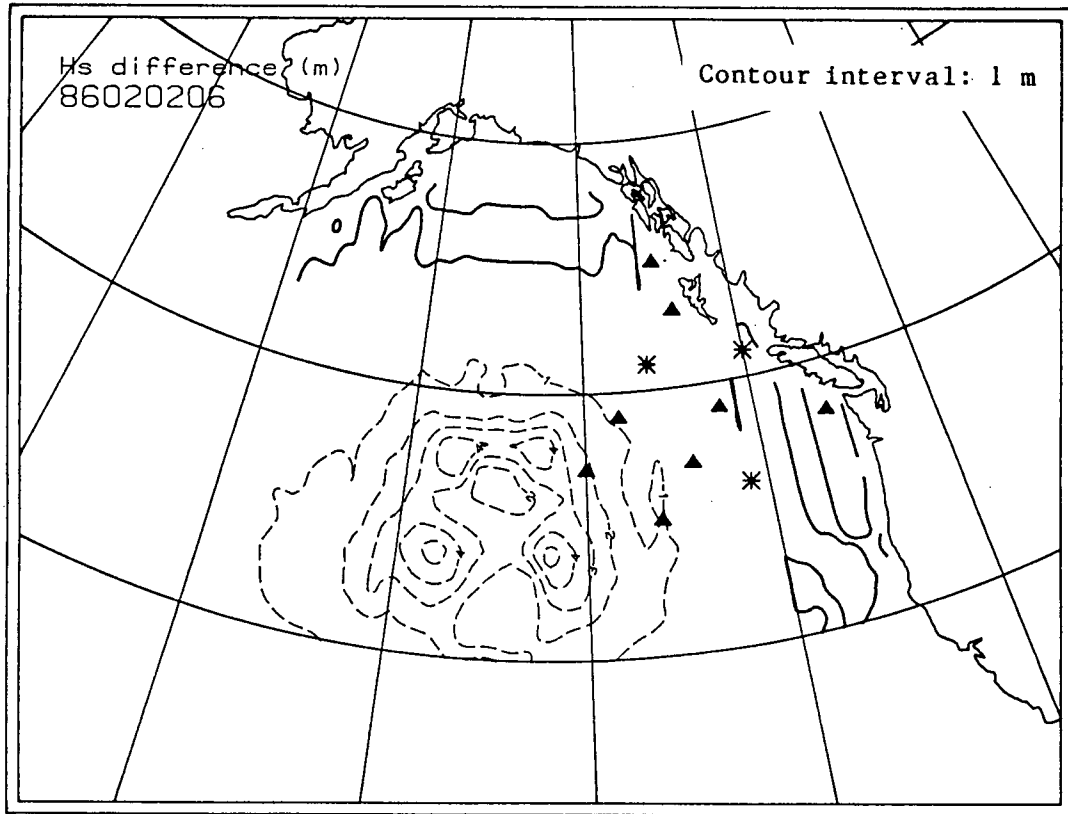
Fig. 5.5 Contoured fields of ΔH_s calculated as storm 2 less storm 1 for the period day 02 hour 06 to day 03 hour 00 in 6-hourly time steps.
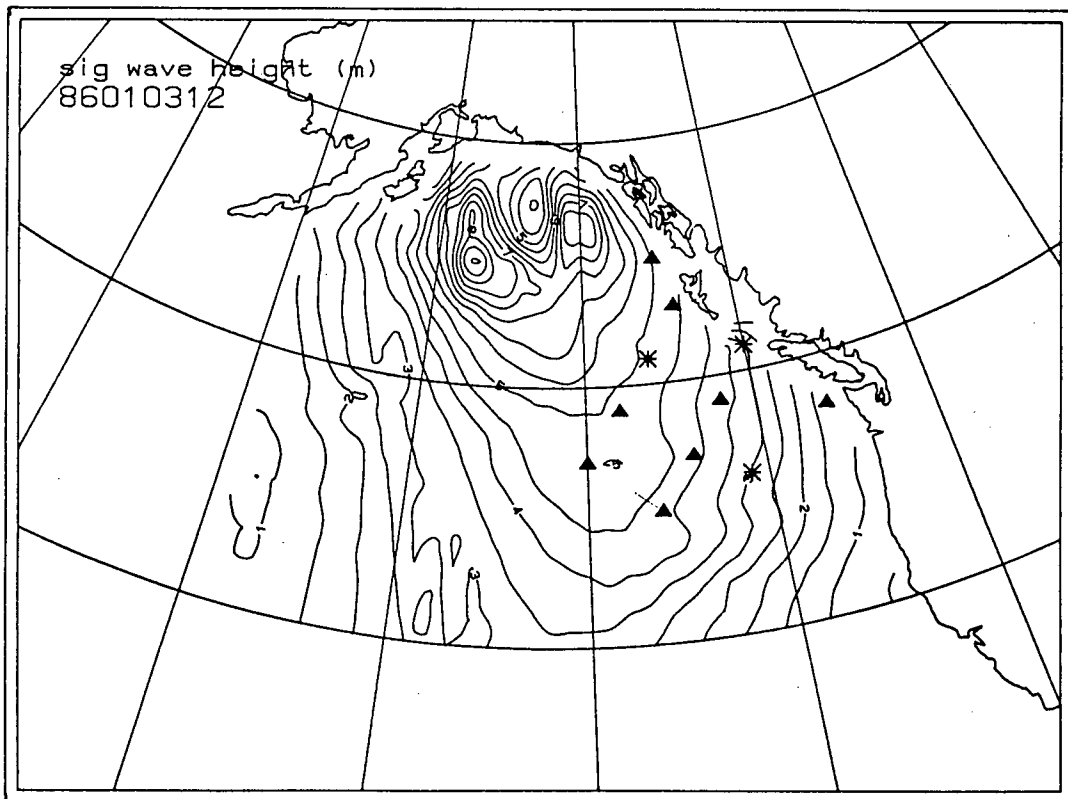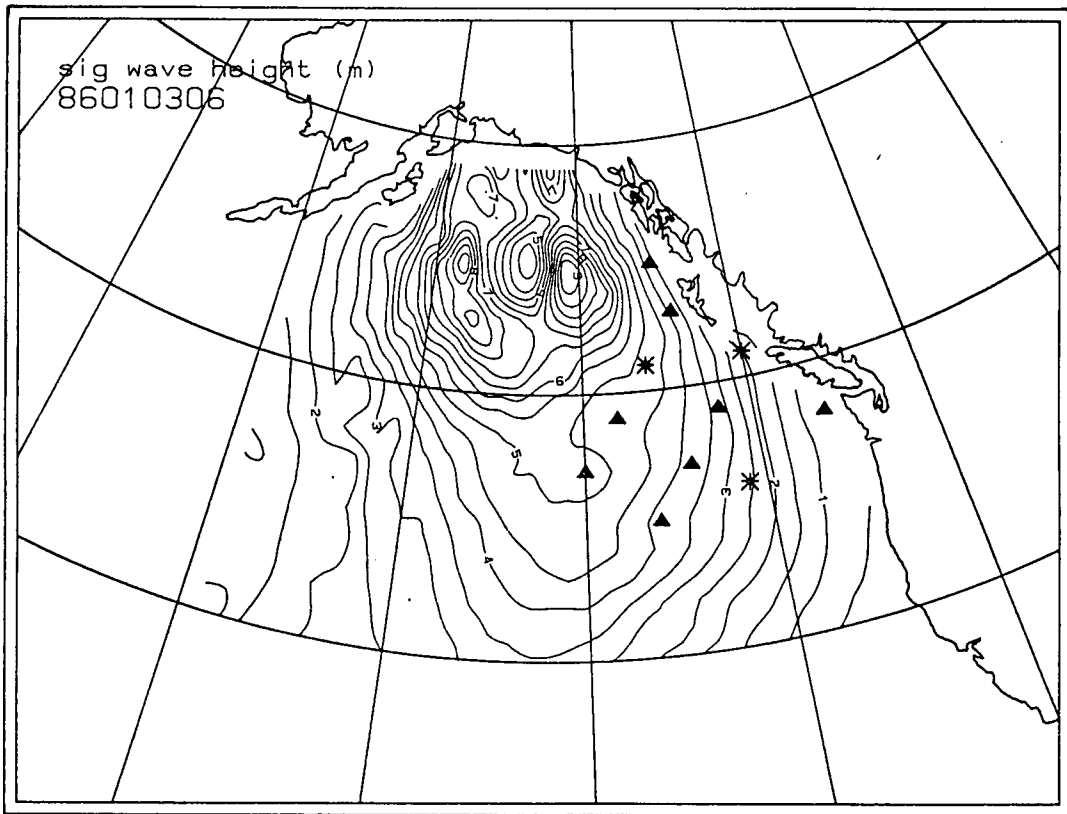
Fig. 5.5   Continued.
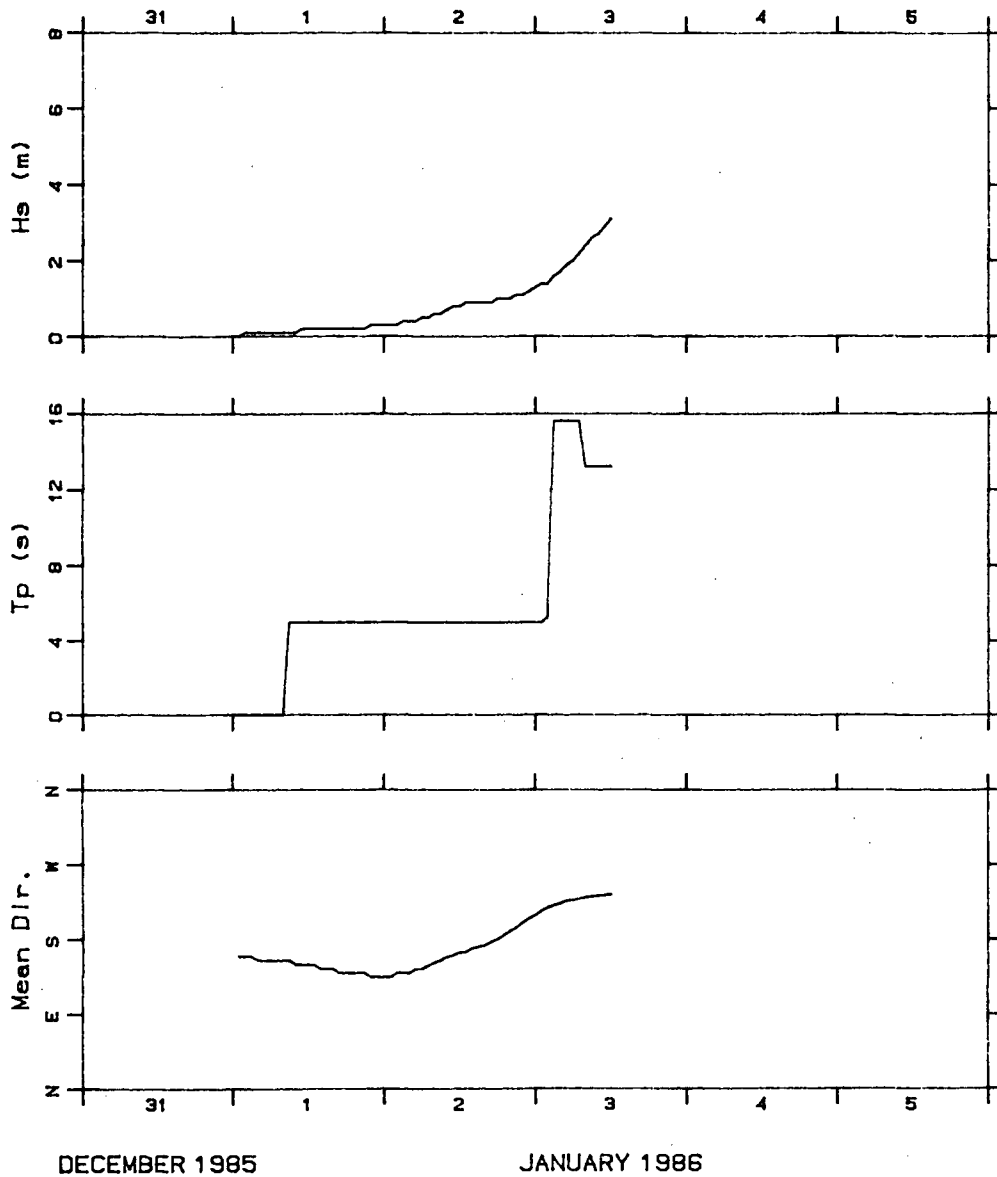
Storm 2

Queen Charlotte Sound

———— (31,13)

Fig. 5.6   Time-series of significant wave height (H_s), peak period (T_p) and mean wave direction at the special output point at the entrance to Queen Charlotte Sound (model grid co-ordinates (31,13)) during storm 2.
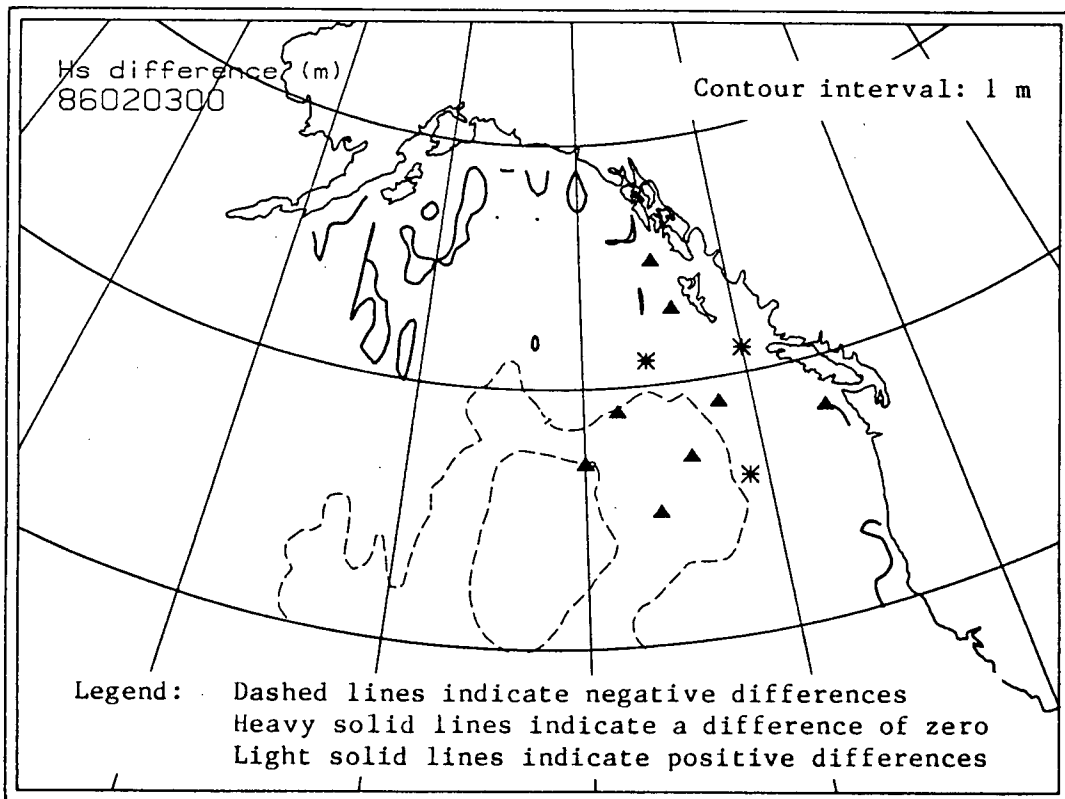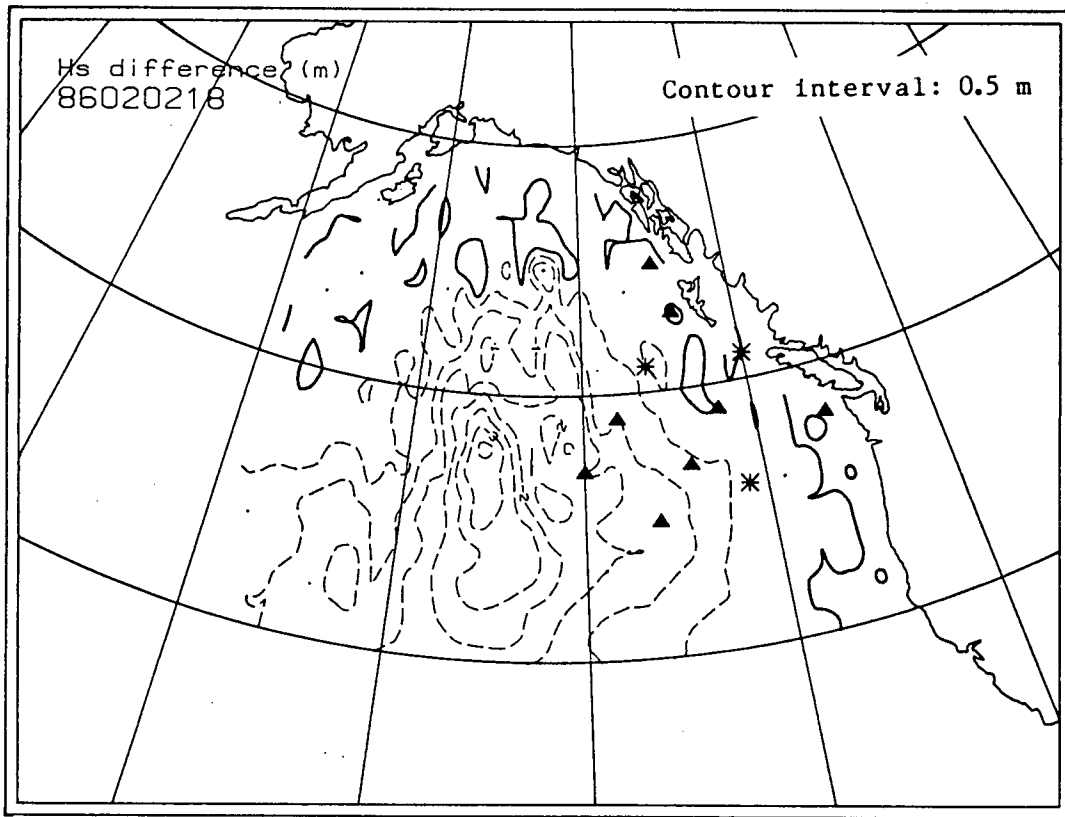
Storm 1   North of Queen Charlotte Islands
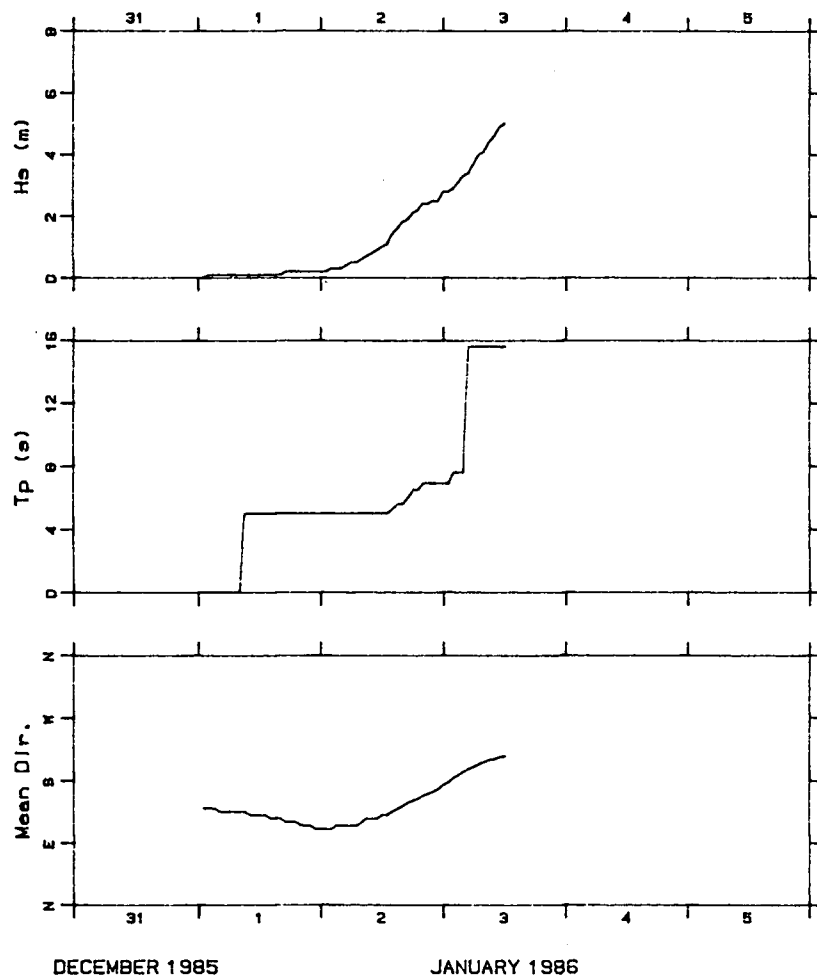
—— (26,17)

Storm 2   North of Queen Charlotte Islands

—— (26,17)

DECEMBER 1985   JANUARY 1986

JANUARY 1986   FEBRUARY 1986
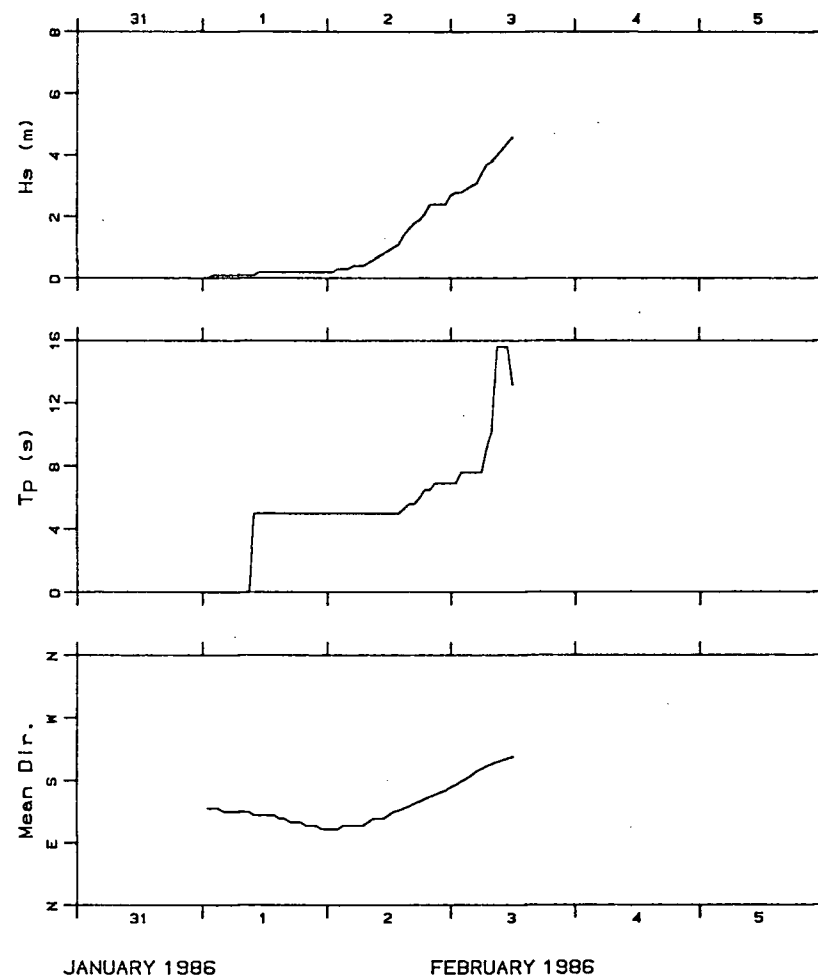
Fig. 5.7 Time-series of significant wave height (H_s), peak period (T_p) and mean wave
direction at the special output point north of the Queen Charlotte Islands (grid
coordinates (26,17)) during storms 1 and 2.

Storms 6 and 7 test the sensitivity of the wave field to variations in storm intensity created by the differences in central pressure that are shown in Fig. 5.8. In storm 6 the 14 mb difference in P_o(min) is quite important since the maximum winds are strengthened from 60 to 75 knots (or 25%). The consequence for the wave field is an increase in the largest H_s from 10 m to 14 m (or 40%).

Along the coast the differences are exemplified by the northern Queen Charlotte Islands and Queen Charlotte Sound sites in Fig. 5.9. The first deviation appears at about the time of peak winds (day 02 hour 18) and progressively builds to an increase of about 1.0 m over 3 m for storm 1 in Queen Charlotte Sound and about 1.5 m in 5 m north of the Queen Charlotte Islands. In terms of specifying a boundary condition to a fine grid nested coastal model, errors of at least 30% could easily result from a serious under estimate of P_o(min) for this type of storm trajectory.

Within the area dominated by local wind sea, Fig. 5.10 shows maximum differences of 5 m in about 9 m as predicted by storm 1, or a potential error of nearly 60% resulting from a 25% change in P_o(min) which is calculated relative to $\bar{P}$=1015 mb. There are, of course, also differences in the storm history in terms of $\Delta P_o / \Delta t$ which mitigate against large sea-state changes. Since the rate of development in storm 6 is more rapid than in storm 1 (in fact, it is similar to storm 2 in this respect), there will be less time for the local sea to reach its maximum potential for the given wind forcing.
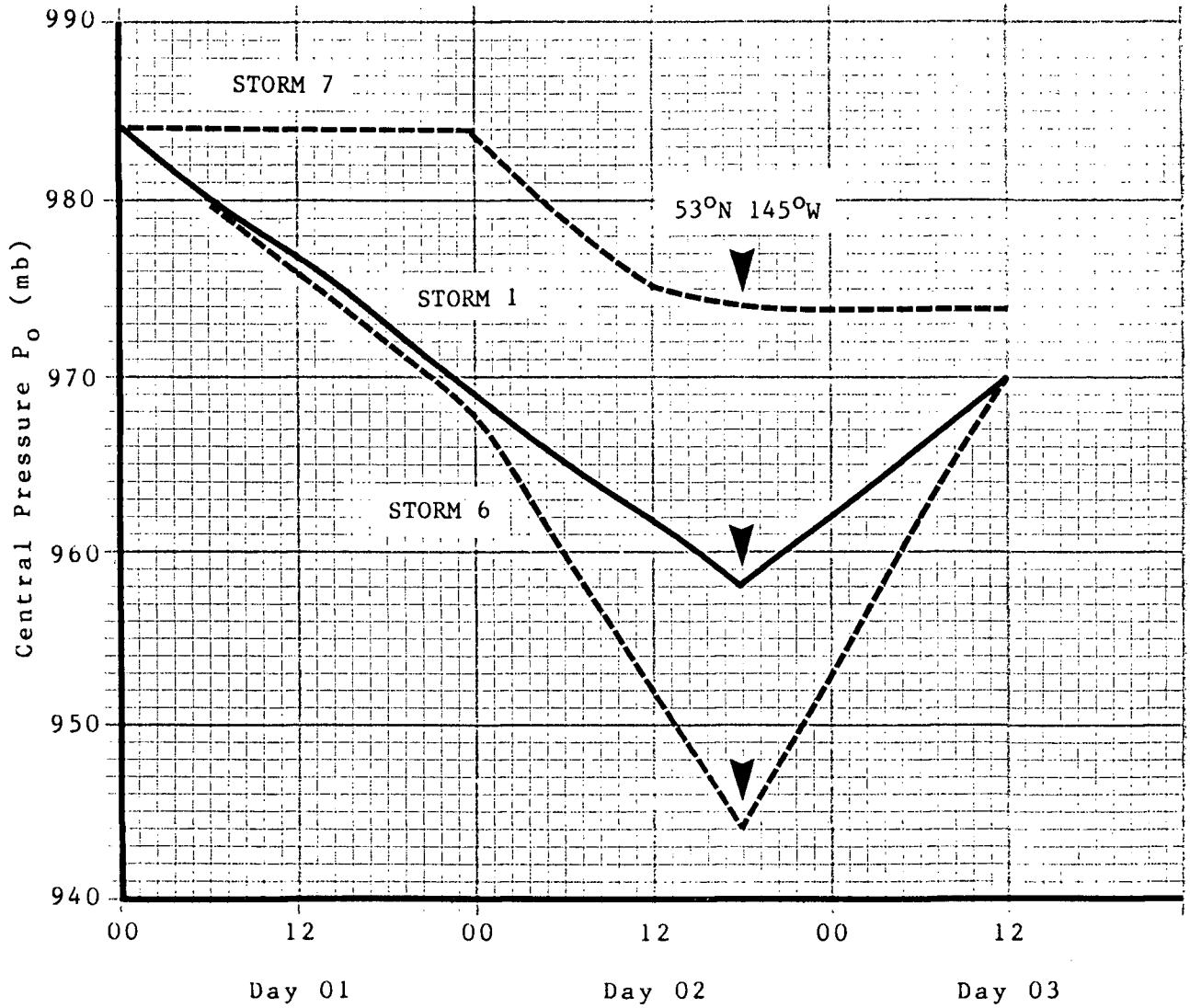
Fig. 5.8   The evolution of P_o in storms 1, 6 and 7.   In all cases P_o(min) is imposed at 53°N 145°W.

Storm 6   north of the Queen Charlotte Islands
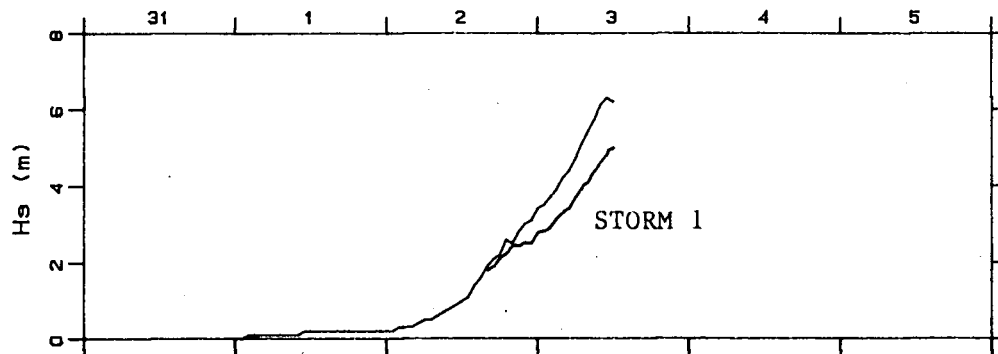
_____ (26,17)

Storm 6   Queen Charlotte Sound

_____ (31,13)

MAY 1986   JUNE 1986
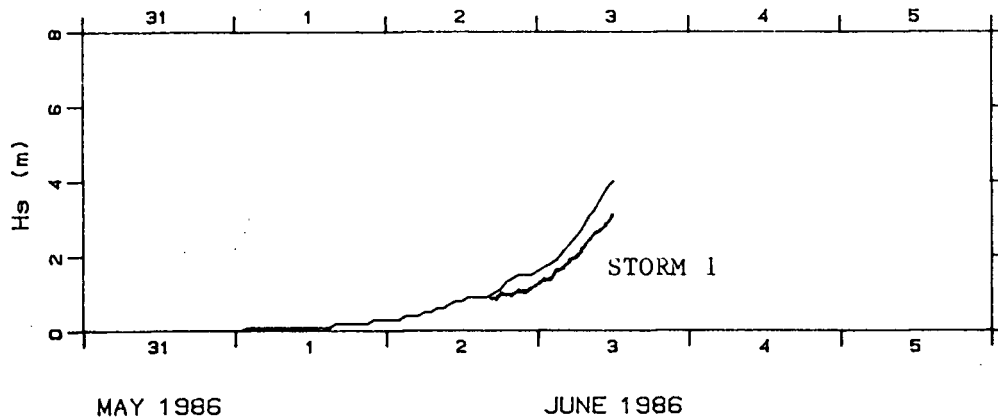
Fig. 5.9   Comparison of storm 1 and storm 6 response as
            exemplified by significant wave height at the special
            output points north of the Queen Charlotte Islands
            (26,17) and at the entrance to Queen Charlotte Sound
            (31,13).

- 82 -

Fig. 5.10 The field of ΔH_s at the time of maximum wave heights in
storm 1 (day 03 hour 00) differenced as storm 6 minus
storm 1 (upper panel) and the corresponding field of H_s
from storm 1.

Storm 7 has considerably weaker winds than storm 1 since its central low of 974 mb is 16 mb higher representing a change of 28% in P_o relative to $\bar{P}$. Peak winds reach only 35 knots, just a little more than half of the 60 knot maximum in storm 1. The largest difference in the significant wave height field is between 5 and 6 m in 10 m for storm 1 as shown in Fig. 5.11. Comparison with the storm 1 H_s field indicates a general reduction, on the order of 50%, throughout the region dominated by the local wind-sea.

The coastal swell climate is also greatly reduced in both height and period due to the weaker sea-state development in the early stages of the storm. Fig. 5.12 illustrates this trend at two stations: one northwest of the Queen Charlotte Islands and the other southeast of these islands in the entrance to Queen Charlotte Sound. A difference of 2 m in H_s combined with a 6 s lower T_p is predicted in storm 7 for the more northerly site by the end of the test which is 18 h after the storm peak. At the Queen Charlotte Sound site, the H_s difference is almost as great, but some long period swell begins to arrive just before the end of the model run.

Storm 4 is also a test of storm intensity in that the radial extent defined by $\bar{r}_{990}$ is increased to 8° of latitude from 6° in storm 1 (and all other storms). This represents an increase in storm size of 222 km (33%) from the centre to the 990 mb isobar. Since the derivation of wind speed depends on dP/dr, lower wind speeds are expected. However, as shown in Fig. 5.13, the local rate of change in P may actually increase for the larger storm system due to the logarithmic scaling of pressure. In Fig. 5.13 this somewhat anomalous behaviour is seen at radial distances between about 800 and 1000 km. In this example, there is essentially no difference in the pressure gradient between about 300 and 800 km and a slight decrease in the gradient from the centre out to about 300 km for the larger storm system.
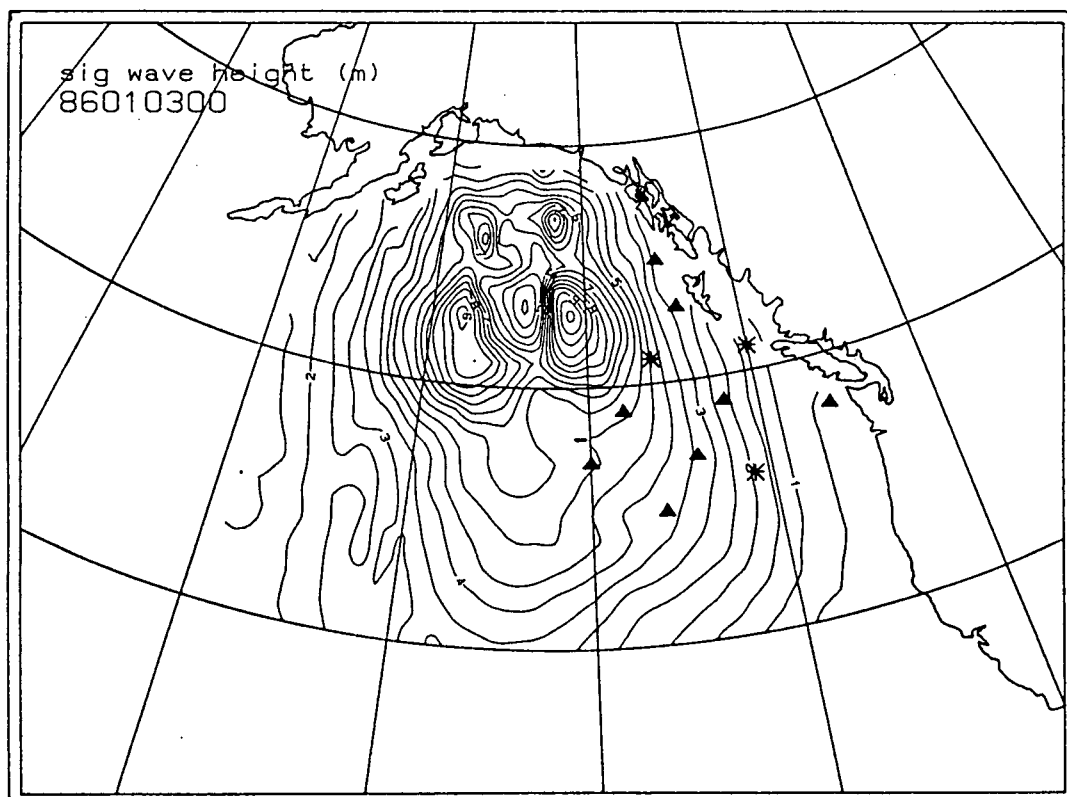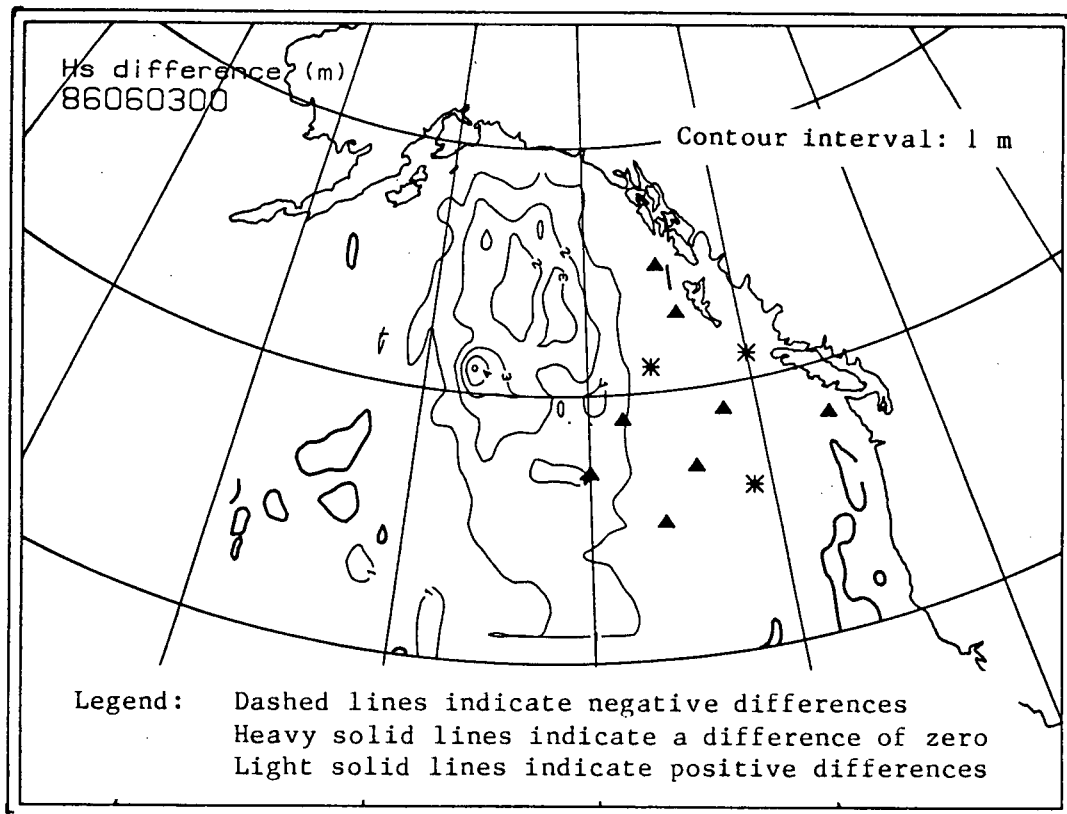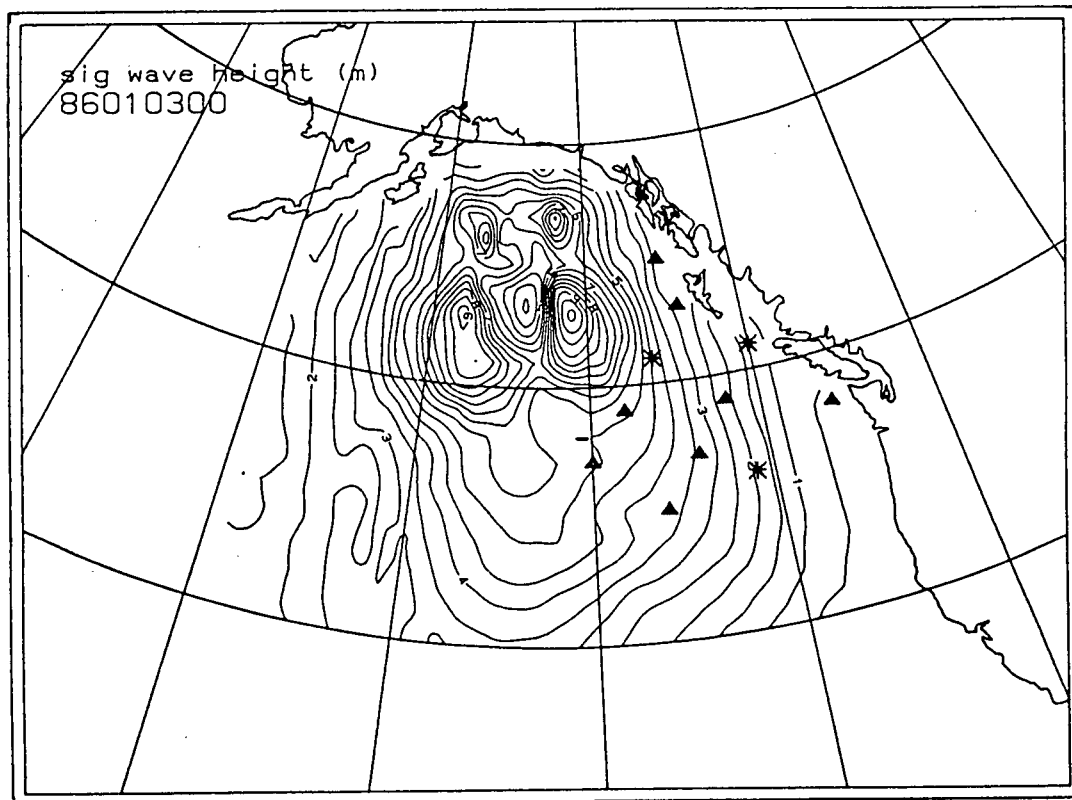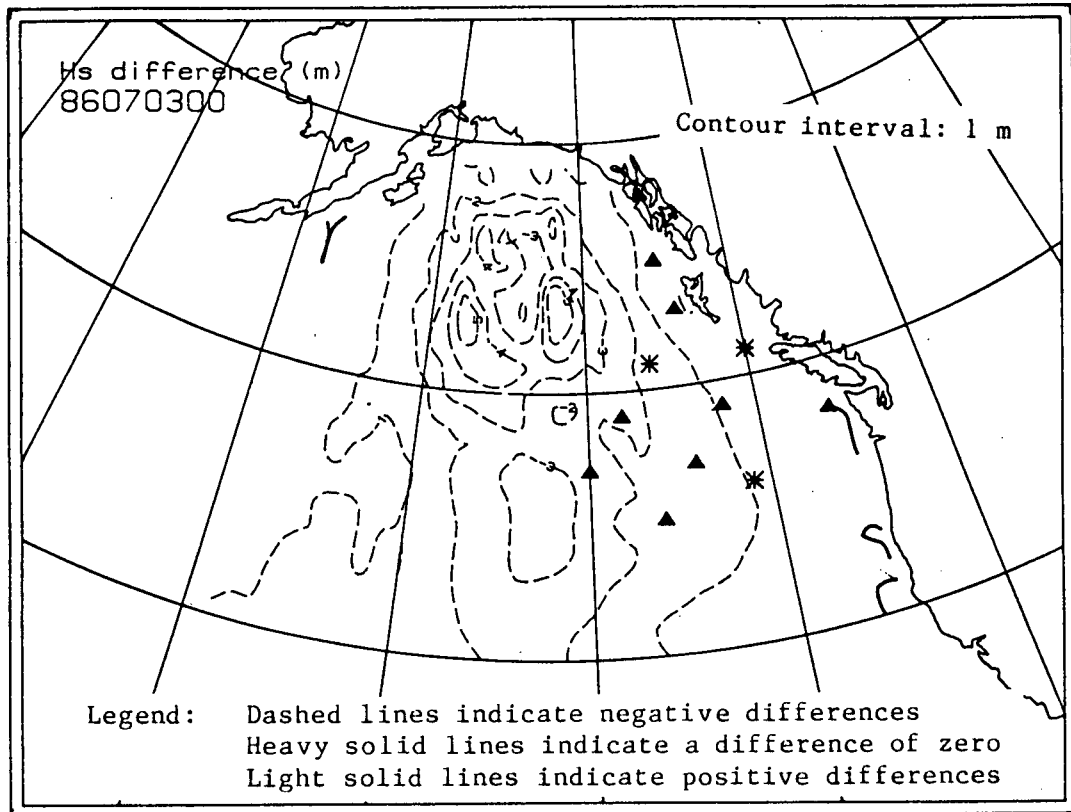
Fig. 5.11   The field of ΔH_s at the time of maximum wave heights in storm 1 (day 03 hour 00) differenced as storm 7 minus storm 1 (upper panel) and the corresponding field of H_s from storm 1.

Storm 7   Queen Charlotte Sound   Storm 7   North of Queen Charlotte Islands
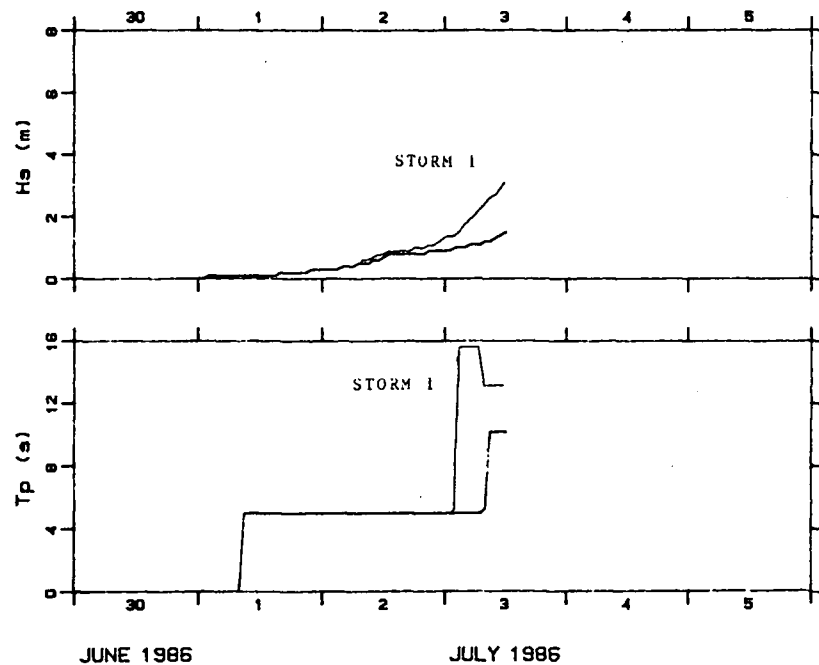
—— (31,13)   —— (26,17)
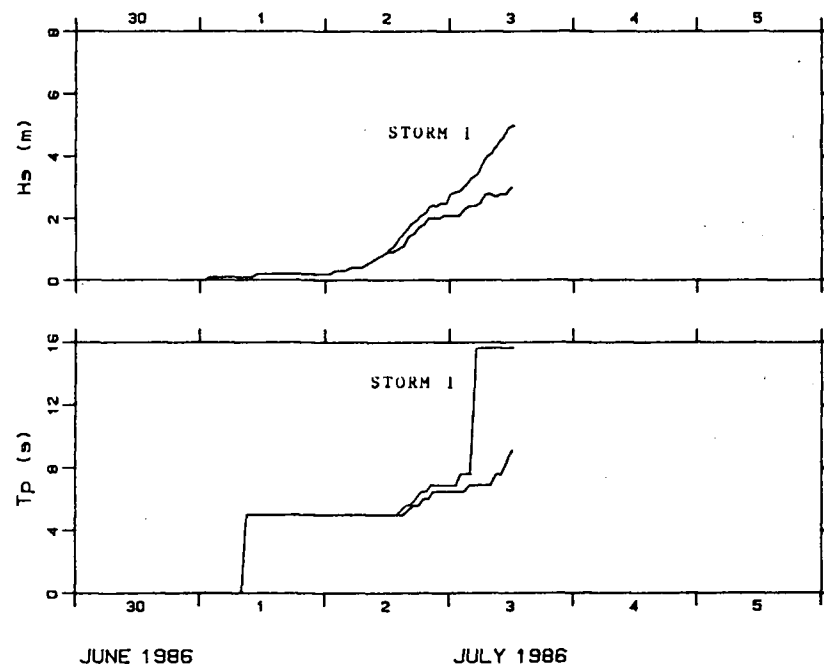
Fig. 5.12   Time-series of H_s and T_p in the entrance to Queen Charlotte Sound and at the coastal site that is north of the Queen Charlotte Islands.
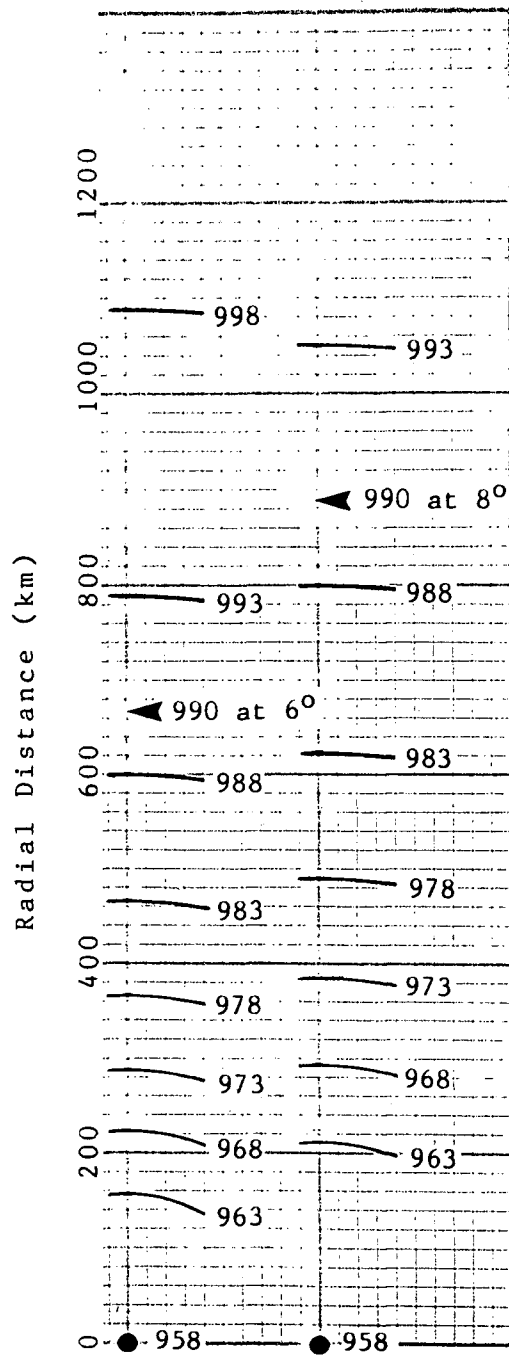
Fig. 5.13   Comparison of isobar radii as a function of the radial scale $\bar{r}_{990}$ for the case of P_o=958 mb.

Fig. 5.14 shows the ΔH_s field (storm 4 minus storm 1) at the time of peak winds in the upper panel and at the end of the model run in the lower panel. These results indicate that during storm development the wave field along the coast is slightly greater in storm 4 than in storm 1 although in the area dominated by local wind-sea the larger storm system H_s values are up to 2 m less than in the smaller base storm. By the end of the storm there is almost no difference in H_s at most of the coastal stations. This conclusion is supported by the time-series of H_s and T_p comparisons in the entrance to Queen Charlotte Sound (Fig. 5.15). At the peak of the storm early on day 03 the storm 1 periods are longer by 2 to 10 s in storm 1. The wave heights are essentially equal throughout the storm, although the storm 4 results are numerically larger. This is due to the slight wind intensification at the storm periphery that is explained by Fig. 5.13.

At the westernmost special output point, which is within 380 km of the storm centre early on day 02, the first 42 hours of results are nearly equal in storms 1 and 4. However, as the overall storm wave field peaks (day 03 hour 00) and decays, the model results at this site (Fig. 5.16) show that the sea-state is 0.5 to 1.0 m less when forced by the larger storm 4.

Of the three intensity parameters tested (speed of development, minimum central pressure, and radial extent), the wave results are certainly least sensitive to changes in radial extent, although the range of values of this parameter that were tested is quite small. Of the remaining two parameters, the value of $P_o(min)$ appears to be the more critical and it is an exceedingly difficult parameter to determine accurately from the scattered measurements made by ships at sea and the few meteorological buoys. Further observations on the speed of storm development will be drawn in Section 5.5 in the discussion of the idealization of the February 5-7, 1960 storm.
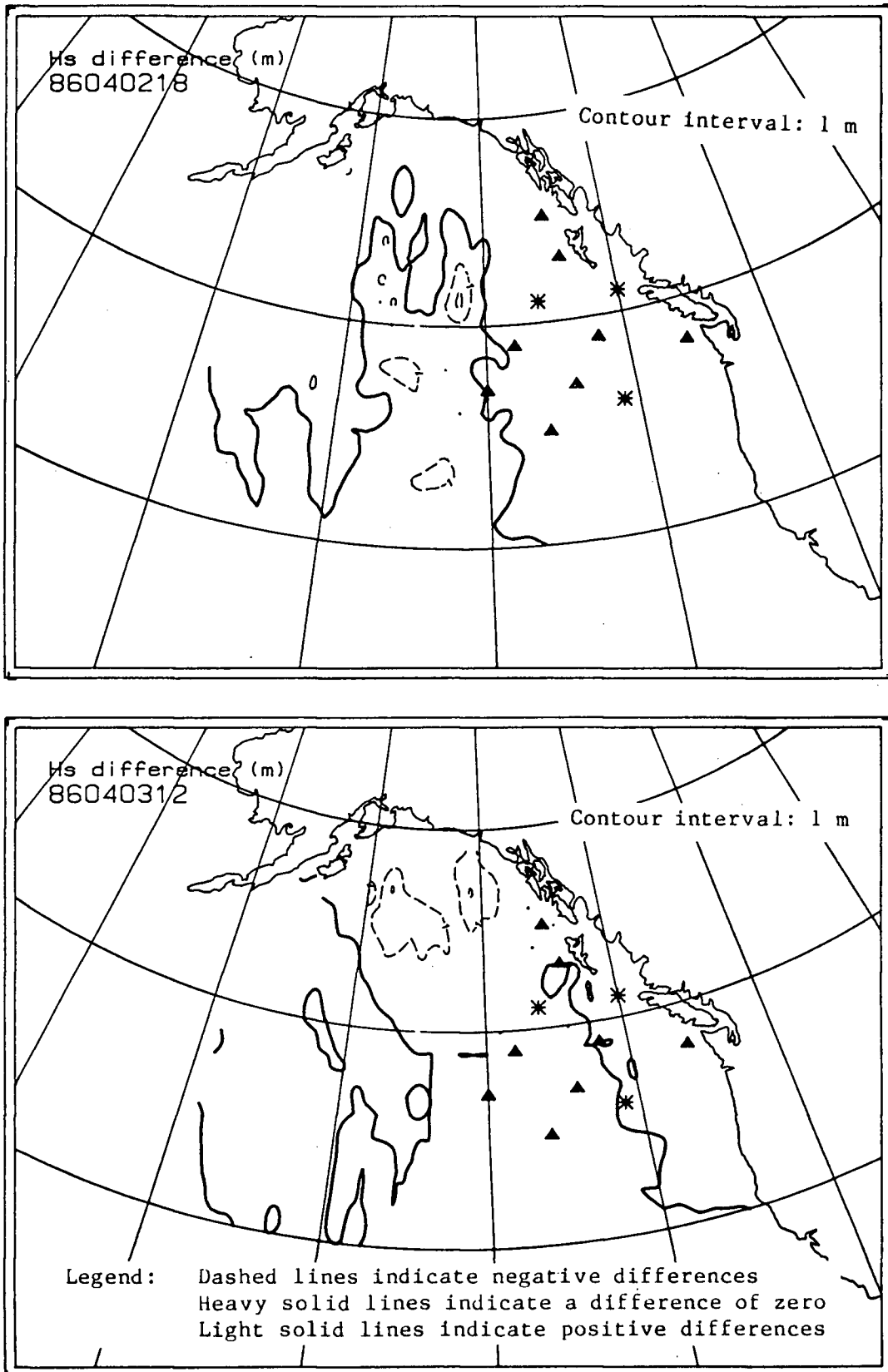
Fig. 5.14   The field of ΔH_s at the time of maximum winds (day 02 hour 18 ;upper panel) and at the end of the modelling sequence (day 03 hour 12; lower panel) differenced as storm 4 minus storm 1.
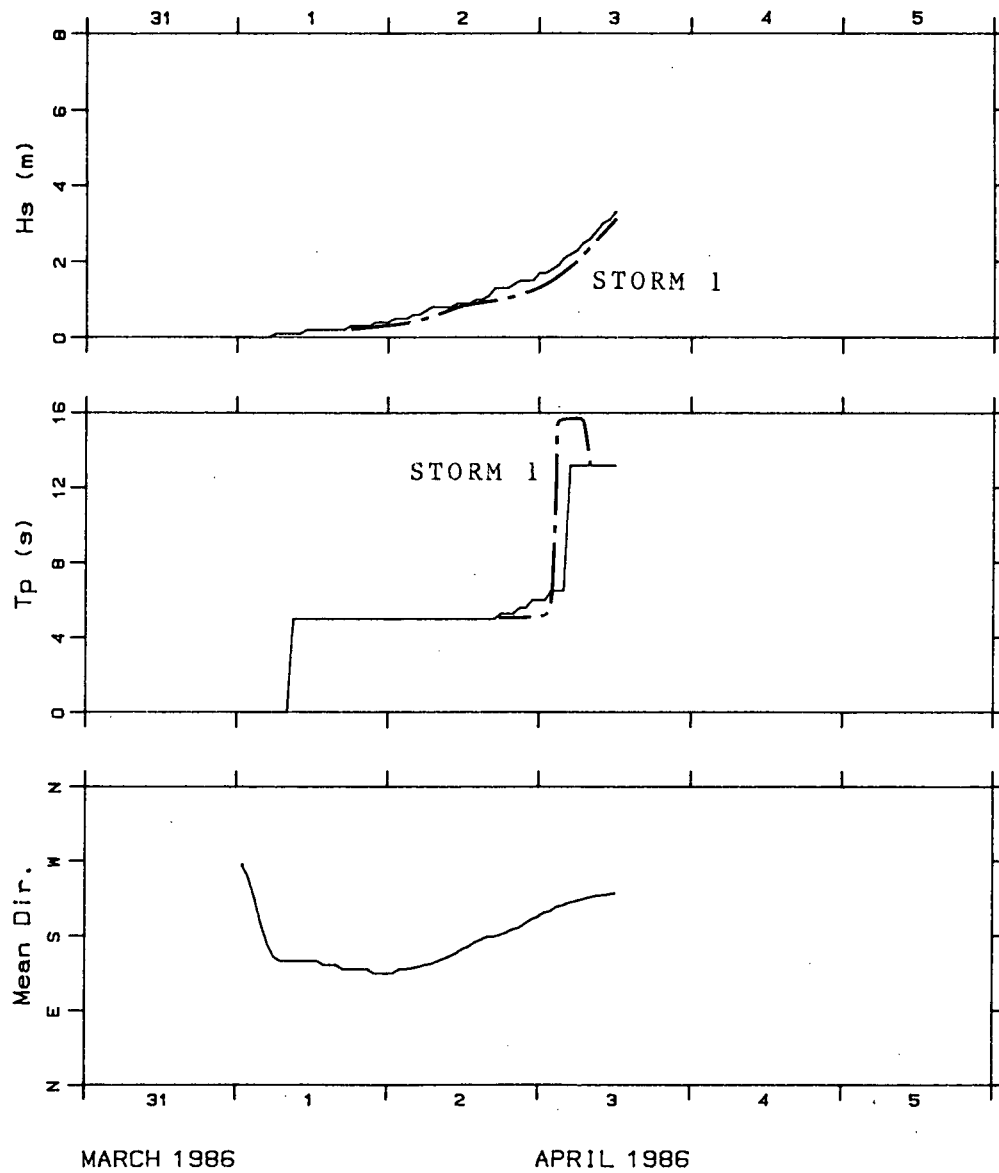
Fig. 5.15   Time-series comparison of H_s and T_p from storms 4 and 1
            at the entrance to Queen Charlotte Sound.

Storm 4

_____ (21,9)
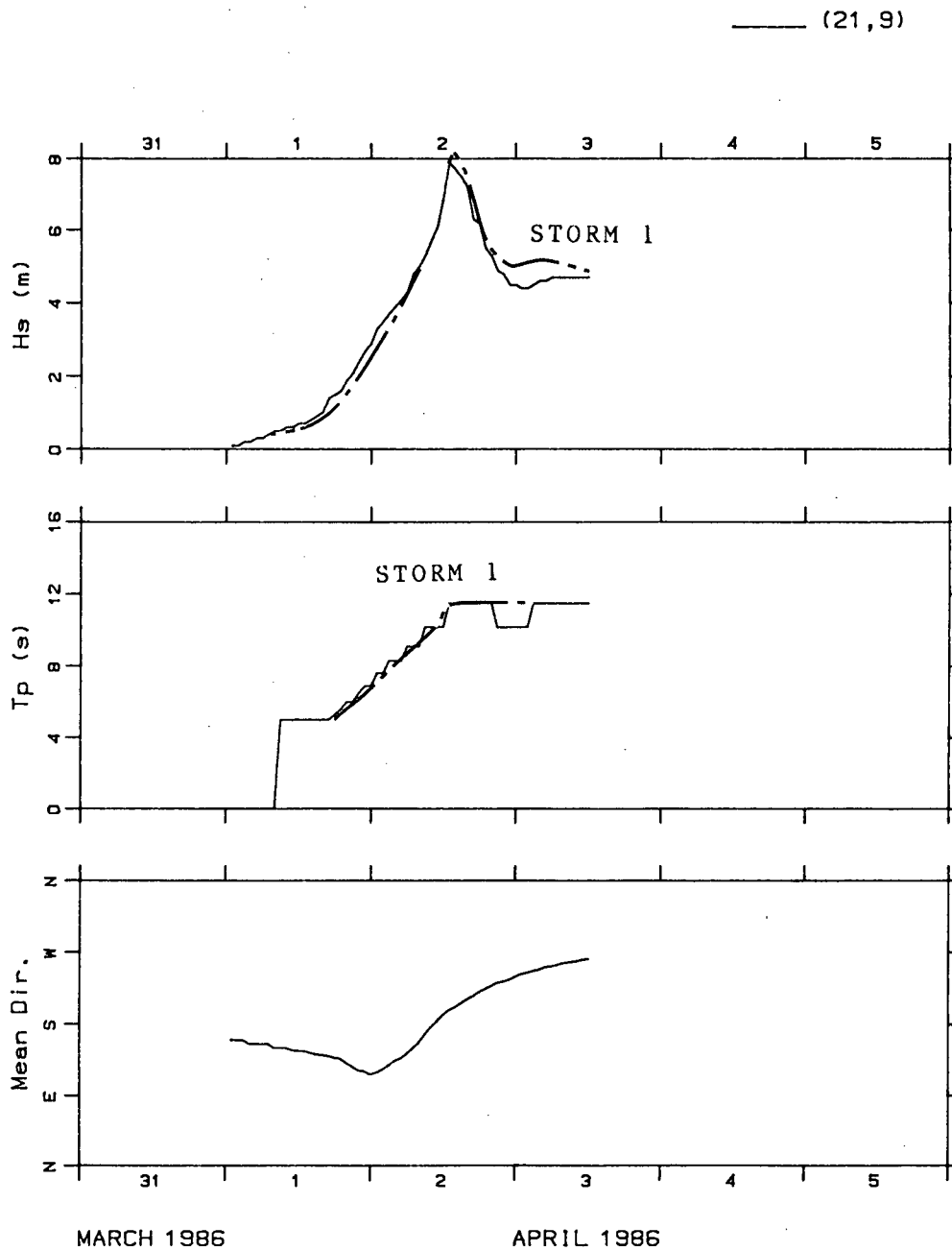
Fig. 5.16   Time-series comparison of H_s and T_p from storms 4 and 1
at the westernmost output site.

5.3 Storm Trajectory

Storm 3 was designed to test the effects of translation of the northward part of the storm trajectory by 5° of longitude to 140°W. Fig. 4.7 shows that this is a reasonable alternate trajectory for both the southwest frontal lows and the southwest cold lows considered in this study. Because the northward portions of the storm 1 and storm 3 paths are convergent, the absolute spatial difference diminishes with increasing latitude. At 42°N, 5° of longitude is a distance of 413 km, but at 59°N it is only 286 km, and this convergence will contribute to a similarity in the sea-states toward the end of the test. Nevertheless, aside from small distortions in the wave field near the coast, the effect is a literal translation of the wave field by 5° towards the coast which is clearly apparent in Fig. 5.17.

Percentage differences in H_s are greatest along the coast. At the Queen Charlotte Sound site, the increase is from 1 m to 3 m on day 02 hour 18 (Fig. 5.17). The most dramatic difference in sea-state near the storm peak is at the special output site due west of the Queen Charlotte Sound site. Here H_s changes from 3.5 m in storm 1 to almost 10 m in storm 3. However, Fig. 5.18 shows that towards the end of the storm sequence on day 03 hour 12, all three sea-state parameters at this site are very nearly the same in the two storm cases. This is consistent with the results of storm 1: considering the final panel of Fig. 5.2, it is clear that in the vicinity of the special offshore output points the spatial gradient in the sea-state is not very large so that a shifting of the H_s field by 5° of latitude can only make about 0.5 to 1.5 m difference.

For the coastal sites, continuity dictates that the gradient in wave height must steepen when the storm track is closer to the coast. This is seen in Fig. 5.17 along Vancouver Island. From the time-series in Queen Charlotte Sound in Fig. 5.19, it appears that the sea-state begins its sharp rise at the coast about 18 hours earlier in storm 3 than in storm 1 (day 02 hour 06 instead of day 03 hour 00). The development of T_p in storm 3 indicates that there is an important local wind-sea component during day 02, which was not well-developed in storm 1, because the coastal winds are somewhat higher when the storm centre is closer to the coast.

At the coast, this scenario produces greater changes than any of the storm intensity tests, including imposition of the deepest central low.
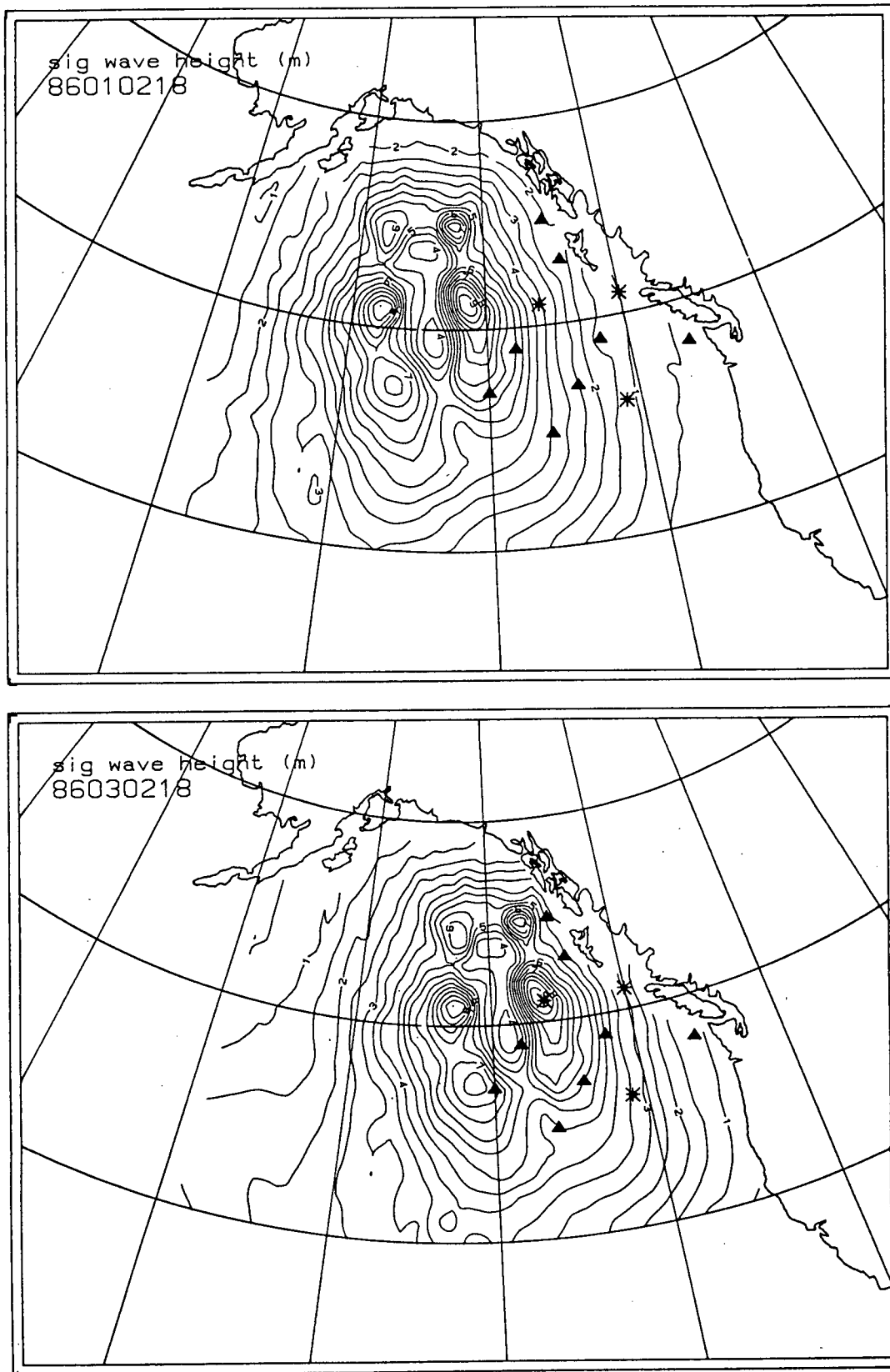
Fig. 5.17   Significant wave height field under maximum winds in storm 1 (upper panel) and in storm 3 (lower panel). The storm trajectory in storm 3 is 5° closer to the coast.

Storm 3
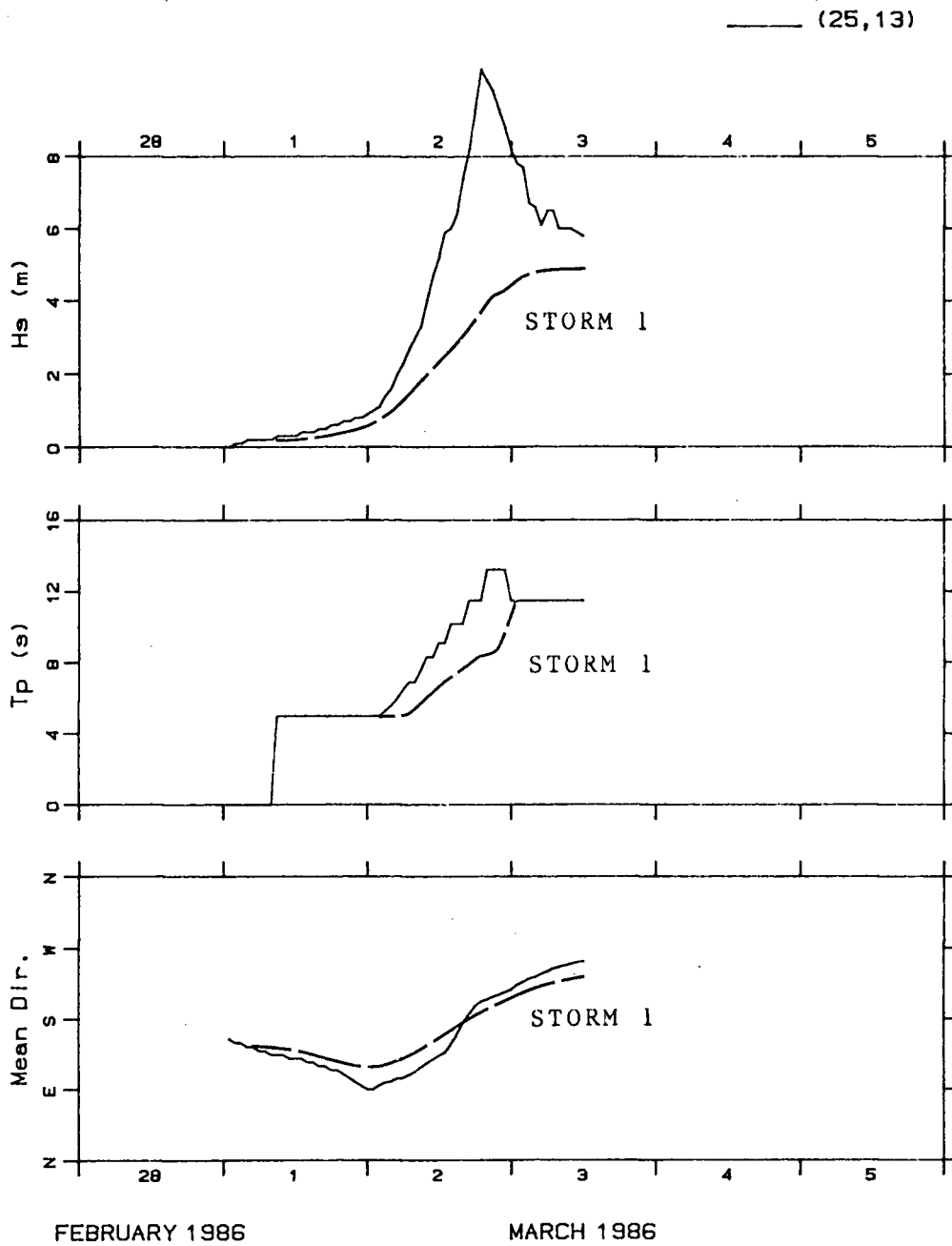
Fig. 5.18 Comparison of the time-series of H_s, T_p and mean direction in storms 3 and 1 at the special output point due west of the entrance to Queen Charlotte Sound.

Storm 3   Queen Charlotte Sound

                                      ———— (31,13)
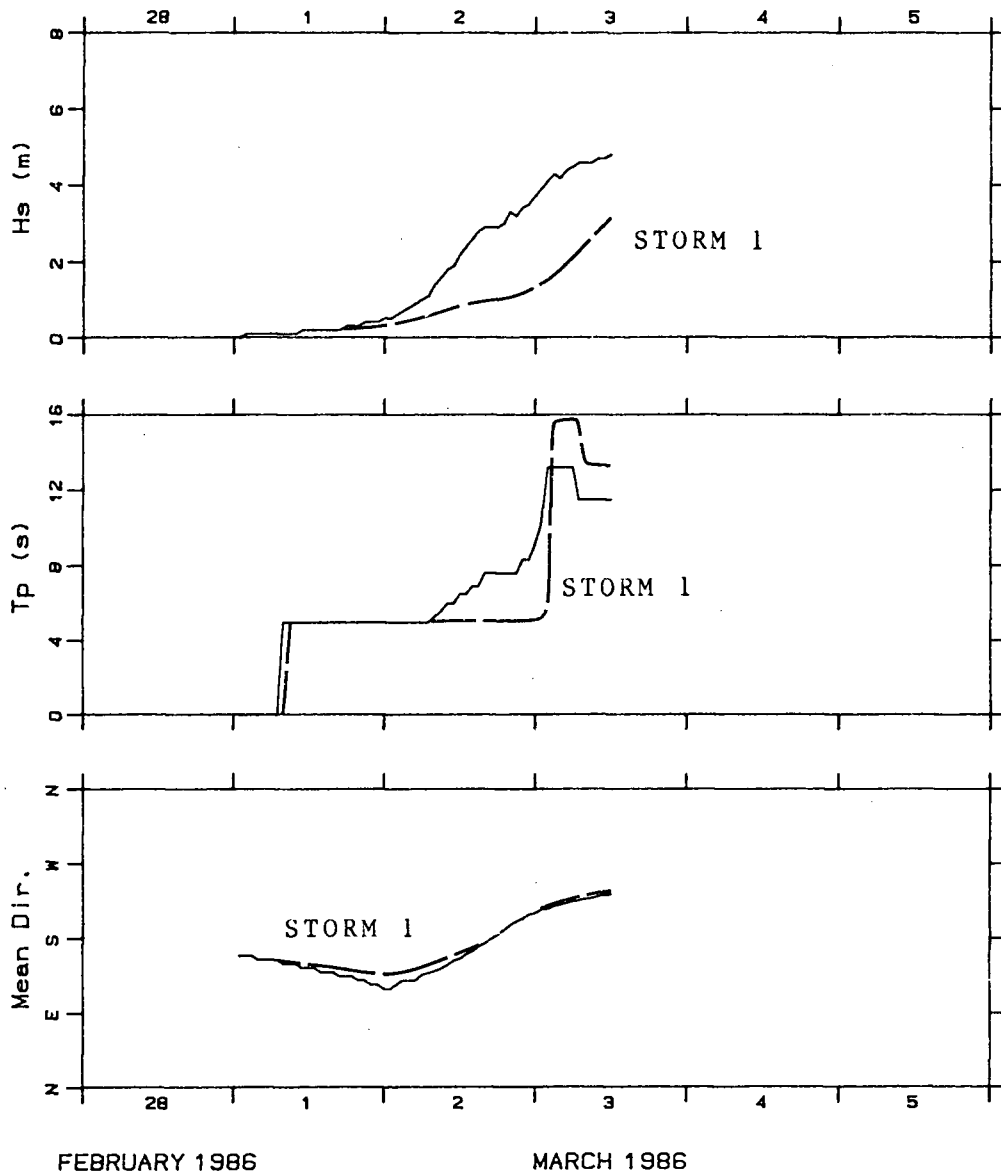
Fig. 5.19   Comparison of the time-series of H_s, T_p and mean
             direction in storms 3 and 1 at the special output point
             in the entrance to Queen Charlotte Sound.

5.4 Advection Rate of the Central Low

In this section only one important case is considered: the stalled low. In Lewis and Moran (1985) there are four examples among the 21 storms in Fig. 4.7 in which a low pressure system became stationary for up to 24 hours, usually north of the Queen Charlotte Islands after the storm peak. Reported sea-states in these storms are invariably high (8 to 10 m local wind sea) and ship sinking was recorded in two of the four storms. Two of these events also had explosive deepening in the development stages.

In the idealized storm 5 example, the storm 1 wind fields are used with a 24 hour insertion of constant wind pattern beginning on day 03 hour 00 centred at $55^{\circ}N$ $145^{\circ}W$. At this time the maximum winds are 50 to 55 knots with a south to north gradient of 10 to 20 knot southerly winds along the B.C. coast.

At day 03 hour 00 the sea-state has developed as shown for storm 1 in Fig. 5.2 at the same time (fifth panel). The conditions 12 and 24 hours later are presented in Fig. 5.20. The maximum H_s has increased from 10 m on day 03 hour 00 to just over 13.5 m 24 hours later. The change in the sea-state pattern during the stall period is shown in Fig. 5.21. The largest difference is an increase of more than 7 m due south of the central low in a region that was weakly developed (4 to 5 m) under the moving storm system.

Along the coast the sea-state increases by more than 2 m by the end of the 24 hour stall (Fig. 5.21). At the offshore special output points, the change is 1 m or less for those sites west of $132^{\circ}W$ and 2 m for the two southerly sites that are east of this longitude. Fig. 5.22 shows the net difference in H_s at the end of storm 5 and the base storm (storm 5 day 04 hour 12 less storm 1 day 03 hour 12). At this point, the two storms are the same and have been for 12 hours: the only difference is the preceding storm history. In the northwest half of the Gulf of Alaska, the storm 5 sea-state is generally elevated by 1 m over that of storm 1. Because the wind and wave circulation is anticlockwise, this increase in H_s can be attributed largely to the stall. In the southwestern quarter of the study domain, the two scenario sea-states are the same within less than ± 1 m. In the southeast, however, H_s is elevated by 1 to 2 m offshore and somewhat more closer to the coast. Based on the final panel in Fig. 5.2 for day 03 hour 12 in storm 1 and the fact that waves arriving at the coast are from the westsouthwest, most of this predicted increase in H_s arises from propagating swell energy that would also arrive for storm 1 within the extra 24 hours of modelling time that was available in storm 5.
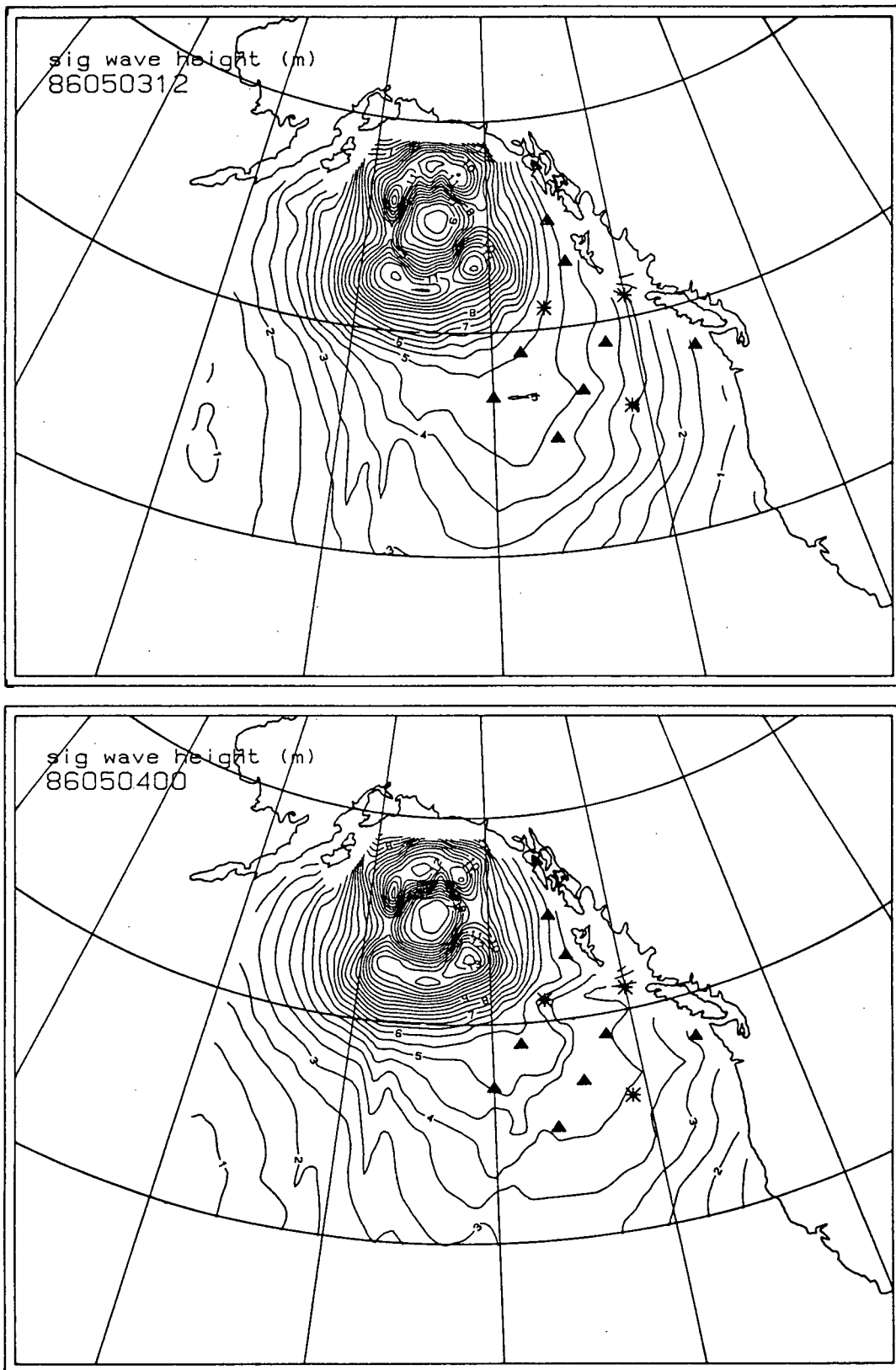
Fig. 5.20   The significant wave height field 12 hours after the
storm stall (upper panel) and 24 hours after the stall
(lower panel). The maximum H_s is 12.5 m on day 03 hour
12 and 13.5 m on day 04 hour 00.
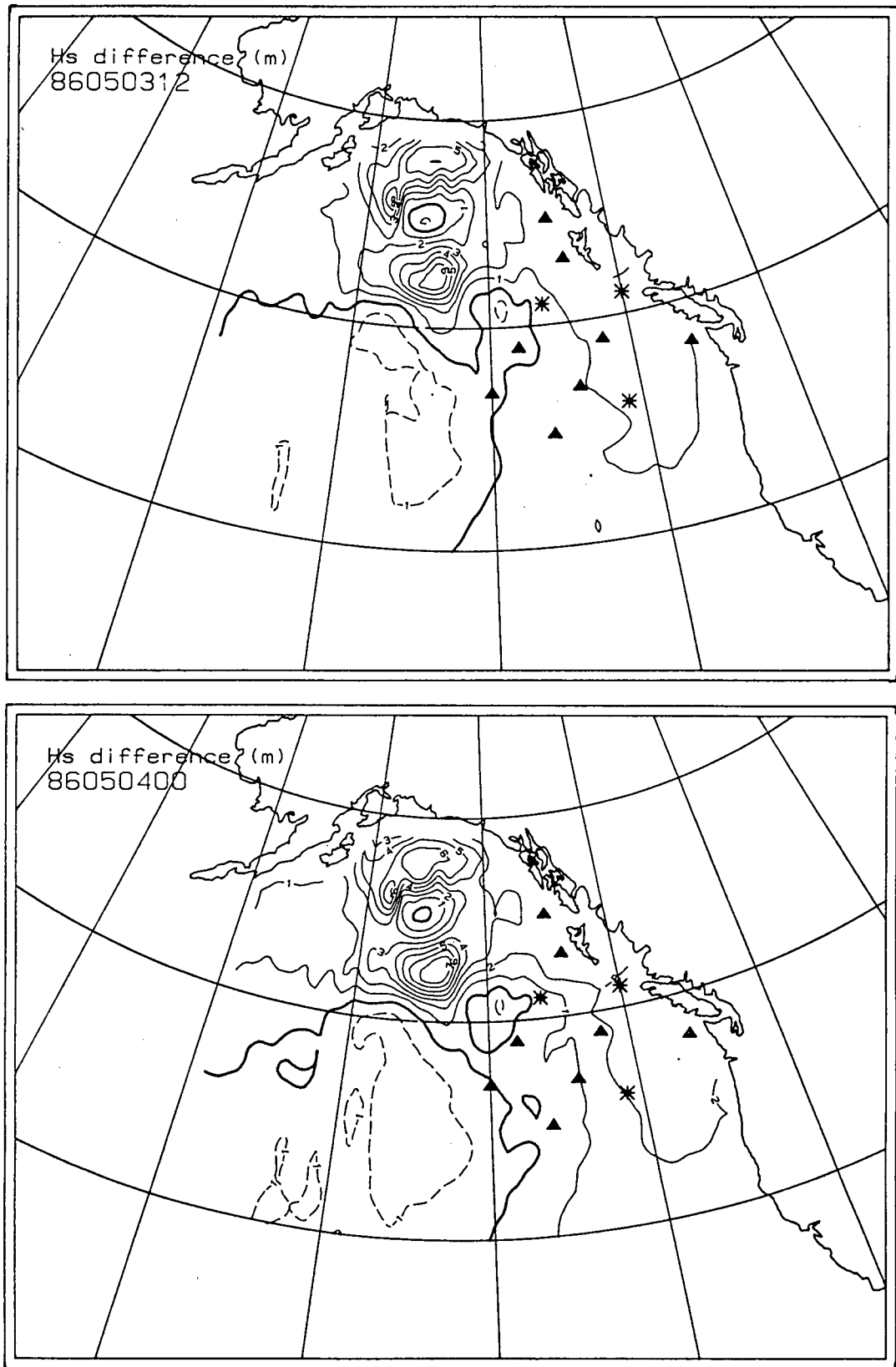
Fig. 5.21   The ΔH_s field calculated as H_s at day 03 hour 00 (the
beginning of the stall) minus H_s 12 hours later (upper
panel) and minus H_s 24 hours later (lower panel).
Maximum differences are on the order of 6 to nearly 8 m
near the storm centre and 1 to 3 m along the B.C. coast.
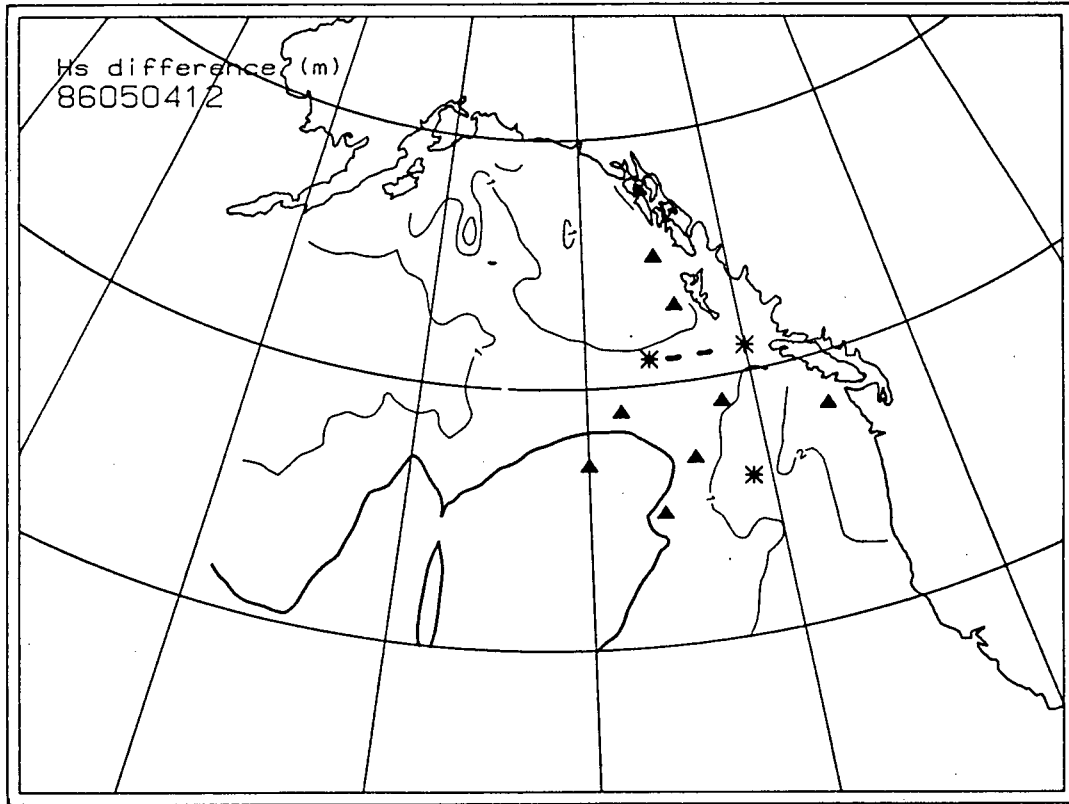
Fig. 5.22 The ΔH_s field calculated as H_s at day 04 hour 12 in storm 5 minus H_s at day 03 hour 12 in storm 1. At these times the storm systems are equivalent and have been for the preceding 12 hours.

The location of the stall will determine which sites receive the most additional wave energy. The more northerly the stall position, the less consequence it will have for the southern coast, and the more impact it will have north of the Queen Charlotte Islands from greater development of local wind-sea in that region and the potential for much more swell energy from the southeast side of a stationary weather system.

5.5 The Idealized Storm of February 5 to 7, 1960

The actual and idealized versions of this storm are illustrated in Fig. 4.9 and 4.10. It has been included to emphasize an important point in wave hindcasting. Even for idealized cases, it cannot be said, without qualification, that any one of the storm parameters is more important than the others. There is ample scope within the natural variability of these factors, if combined in unfavourable ways, to generate a more severe sea-state than that produced by any of the extreme cases already investigated.

Storm 8 has a number of characteristics in common with other test scenarios, but they occur in unique combinations. For example, it has the same minimum central low pressure of 944 mb as storm 6; it has a 12 hour explosive deepening segment preceding P_o(min) that, at -1.7 mb/h, is about the same rate as in storm 2; it has the same trajectory as storm 1 (and all others except number 3).

The important characteristics which make storm 8 more severe than any of the others are threefold:

(1) P_o(min) is reached in the southwest quadrant of the model grid. As a result, the southwesterly swell reaching the southern B.C. coast will be more energetic.

(2) P_o(min) persists for 24 hours as the storm advects eastward and then northward (see Fig. 4.10). This means that the duration of maximum winds is much longer than in the average (storm 1) case.

(3) The central pressure is lower, and hence the winds are stronger, as the storm enters and exits from the study area.

It is more uncertain what the exact effect of differences in the storm speed are. It is slower in the B-C leg of the trajectory which will tend to build the maximum wave field a bit higher, but it is also a little faster in the C-D section which will tend to diminish the sea-state somewhat on the northern coast. Another factor which offsets the promotion of high sea-states, especially for the northern coast, is that the filling process begins 3° of

latitude further south in storm 8 than in any other test case.

Because this storm is much stronger while it is centred in the southerly latitudes of the model grid, the southwesterly swell energy that propagates towards Vancouver Island and Queen Charlotte Sound ought to be considerably greater than in other scenarios: higher H_s and longer T_p. This is confirmed in Fig. 5.23 in Queen Charlotte Sound.

The origin and evolution of the coastal swell energy is illustrated in Fig. 5.24 with 12-hourly H_s fields from storm 8, using the highlighted 7 m contour as a reference. The wave pattern near the southern grid edge at day 02 hour 18 gradually becomes more independent of the active storm centre and propagates to the east from the region centred around $145^{\circ}W$ and to the northeast from areas on the southeastern side of the storm centre. At the same time energy is dispersed with the higher waves travelling faster than the smaller ones, and energy is dissipated through the wave-wave interaction mechanism that cascades energy to higher frequencies where the spectrum may already be saturated.

Based on the H_s pattern on day 03 hour 18 and the westsouthwesterly mean wave direction (Fig. 5.23), the sea-state could be expected to peak at about 8.5 m in Queen Charlotte Sound. By contrast, H_s in storm 6 (with the same trajectory and the same minimum central low pressure) will probably not exceed about 6.5 m at this location. Fig. 5.25 shows the evolutionary pattern of H_s for this less severe storm using the 5 m contour as a reference that is roughly equivalent to the 7 m contour from storm 8 (Fig. 5.24). The similarity of the swell field patterns in these two storms emphasizes, for this particular trajectory, that

(1) the energy content in the swell that will arrive at the coast is almost totally determined by the early storm history, and

(2) the propagation onto the coast, particularly south of the Queen Charlotte Islands, is essentially independent of the later low pressure system evolution.

Storm 8   Queen Charlotte Sound

—————— (31,13)
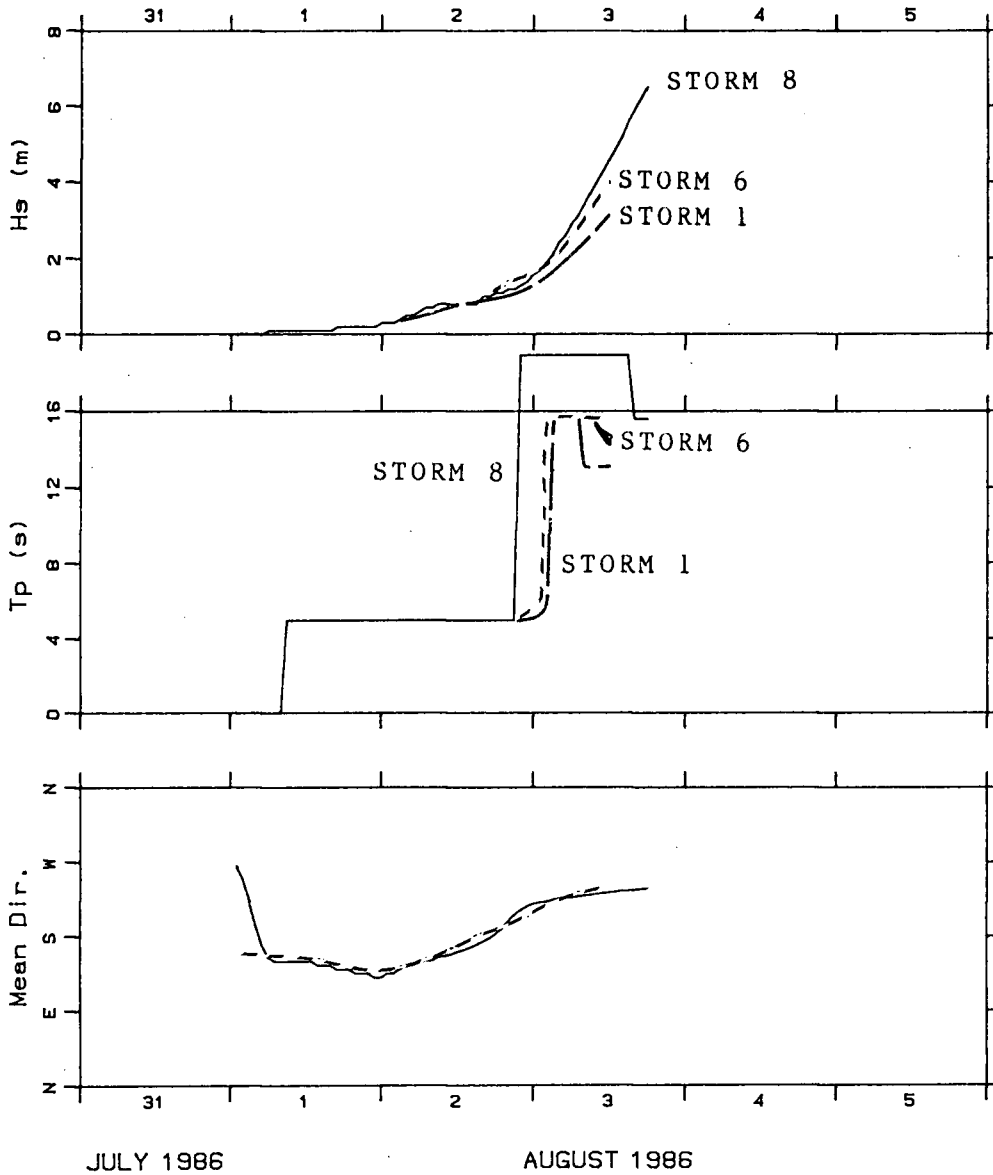
Fig. 5.23   Time-series response of H_s, T_p and mean wave direction
in the entrance to Queen Charlotte Sound for storms 1, 6
and 8.   Aside from the very early spinup period, the
mean direction in all storms is essentially the same.
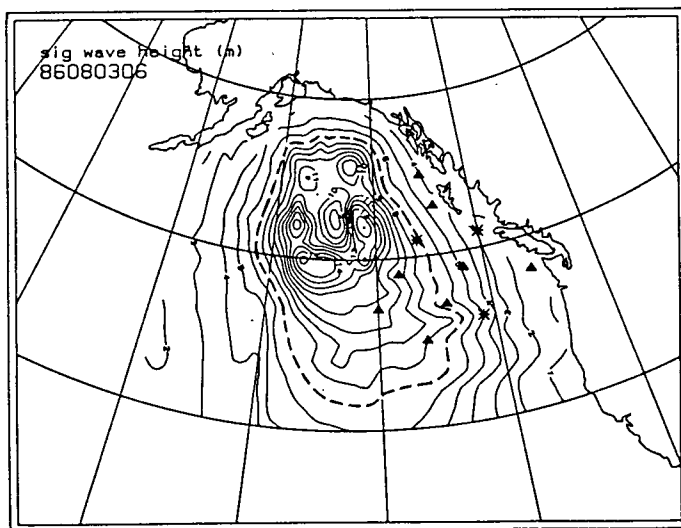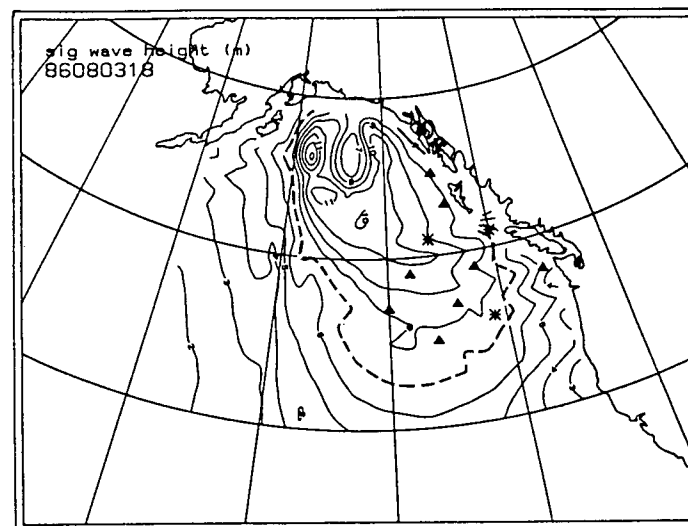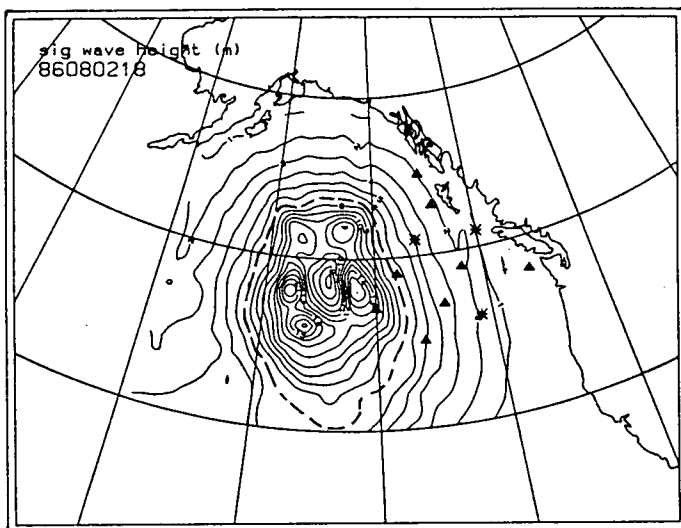
Fig. 5.24

The sea-state pattern in terms of H_s in storm 8 at 12-hourly intervals beginning on day 02 hour 18.

sig wave height (m)
8606021/2

sig wave height (m)
8606031/2

sig wave height (m)
86060300
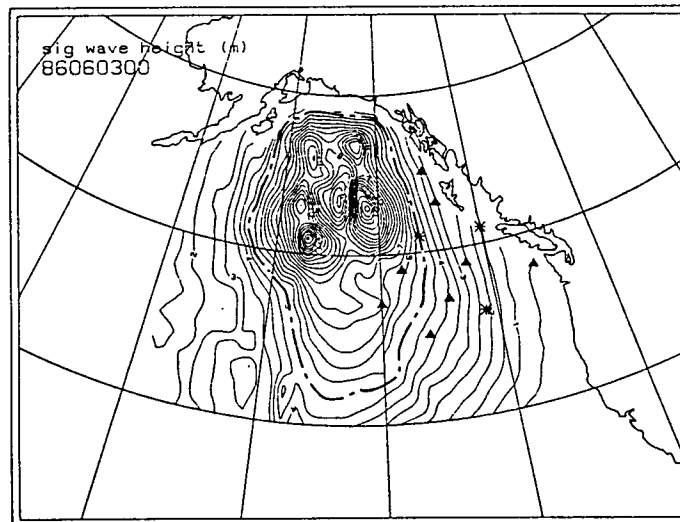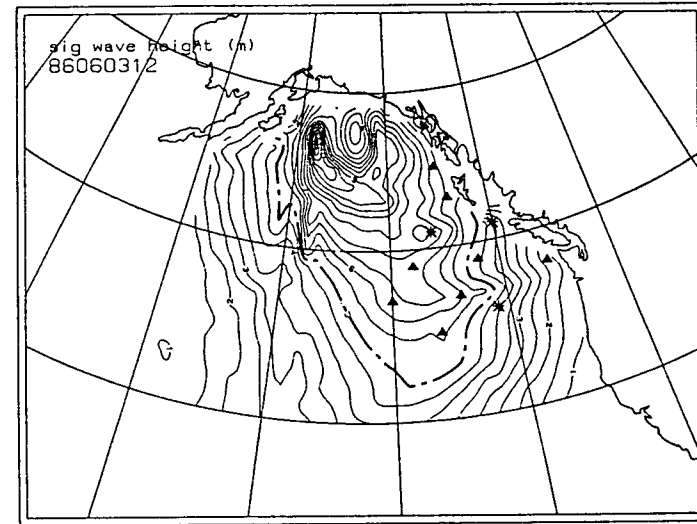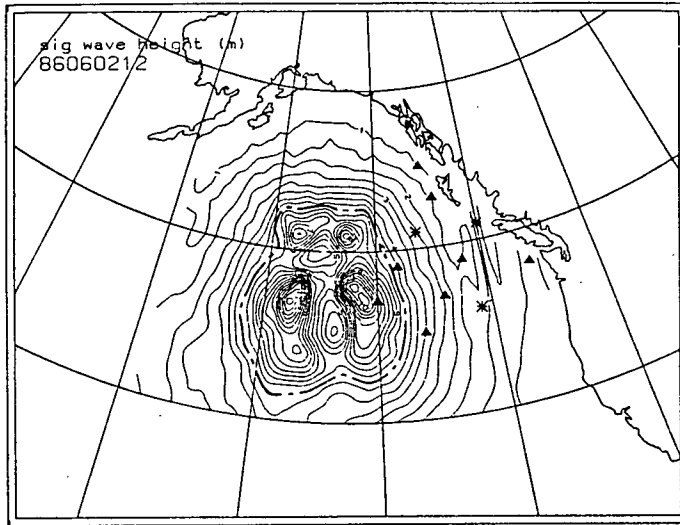
Fig. 5.25

The sea-state pattern in terms of H_s in storm 6 at 12-hourly intervals beginning on day 02 hour 12.

6.0 SUMMARY OF RESULTS AND CONCLUSIONS

This analysis has investigated the sensitivity of hindcast sea-states on the deep ocean west of the coast of British Columbia to variations in meteorological parameters for a particular class of storm trajectory. In this chapter the study findings are summarized and quantified for each storm parameter in turn. Thereafter, general conclusions on the relative effect of each parameter is discussed in terms of deep ocean and coastal sea-state hindcasting.

6.1 Summary of Sensitivity Test Results

To characterize the maximum locally generated sea-state differences, three comparative situations were considered:

(1) the maximum value of H_s in the base (storm 1) case and the corresponding value in the sensitivity case;

(2) the maximum H_s in the sensitivity test and its corresponding base height; and

(3) the greatest ΔH_s at or following the storm peak and the minimum base H_s within this region.

While these comparisons do not necessarily isolate the largest per cent changes, they do characterize the sea-state variations sufficiently to rank the importance of the various pressure parameters for wave hindcasting. All differences are reported as sensitivity storm minus the base storm; hence negative ΔH_s values mean the sensitivity test results are lower than the storm 1 predictions.

The coastal swell variations were considered separately in slightly different terms. The changes between the base H_s and the sensitivity cases were examined at three specific locations: the special output points near Tofino, in the entrance to Queen Charlotte Sound and just north of the Queen Charlotte Islands. At these sites, the difference between hindcast maxima were determined, independent of the time of occurrence of either one, in the way that most model performance characteristics are reported.

6.1.1 Storm Intensity

Radial extent of the low pressure system, the minimum central pressure and the rate of intensification are the key factors considered here.

Radial Extent

The storm size was defined in terms of a constant radius of the 990 mb isobar, and as such it may vary widely from 3° of latitude (334 km) to about 13° (1445 km) with a mean of 8° (890 km). In this study the base value was set at 6° (667 km) and the sensitivity to a change to 8° was investigated. The results are summarized in Table 6.1

Table 6.1
Summary of Sensitivity to Radial Extent

Base Value:	6° of latitude (667 km)
Sensitivity Value:	8° of latitude (890 km)
Per Cent Change:	33% increase in radius
	78% increase in area

Wind Field Variations   near storm centre, decreases ~ 5 to 10 knots

remote from storm centre (in the vicinity of the 990 mb isobar), increases ~ 5 knots
no change in between

Maximum Local Wind-Sea Difference

Maximum Base Value:	10 m on day 03 hour 00 $\Delta H_s = -1$ m (-10%)
Maximum Sensitivity Test:	9 m on day 03 hour 00 $\Delta H_s = -1$ m (-11%)
Maximum Difference:	-2 m on day 02 hour 18 min. base $H_s = 8.5$ m (-24%)
	(very localized under the maximum winds)

Coastal Swell   storm maxima to end of test run

	Base H_s (m)	Sensitivity H_s (m)	ΔH_s (m)	Difference
Tofino	1.3	1.6	0.3	23%
Queen Charlotte Sd	3.1	3.3	0.2	6%
N Queen Charlotte I	4.7	4.7	0.0	0%

Lowest Minimum Central Low Pressure

The minimum central pressure was imposed at 53°N 145°W. In the base case it had the mean P_o(min) value of 958 mb and in the sensitivity test it was reduced to 944 mb. This latter value represents a very intense low pressure system. The sensitivity test results are summarized in Table 6.2.

Table 6.2

Summary of Sensitivity to Lowest Minimum Central Pressure

Base Value:	958 mb at 53°N 145°W
Sensitivity Value:	944 mb at 53°N 145°W
Per Cent Change:	25% deeper relative to $\bar{P}$ = 1015 mb

Wind Field Variations   near storm centre, increases - 10 to 15 knots

   5 knot increase out to about 600 km from storm centre

Maximum Local Wind-Sea Difference

Maximum Base Value:	10 m on day 03 hour 00 ΔH_s = +1.5 m (15%)
Maximum Sensitivity Test:	14 m on day 03 hour 00 ΔH_s = +5 m (36%)
Maximum Difference:	+5 m on day 02 hour 18 min. base H_s = 6.5 m (77%)
	(very localized under the maximum winds)

Coastal Swell   storm maxima to end of test run

	Base H_s (m)	Sensitivity H_s (m)	ΔH_s (m)	Difference
Tofino	1.3	1.7	0.4	31%
Queen Charlotte Sd	3.1	4.0	0.9	29%
N Queen Charlotte I	4.7	5.9	1.2	26%

Highest Minimum Central Low Pressure

The highest value of P_o(min) imposed at 53°N 145°W was 974 mb. In this case, the storm did not intensify very greatly during its passage through the model domain. Its characteristic sea-state differences are presented in Table 6.3.

Table 6.3

Summary of Sensitivity to Highest Minimum Central Pressure

Base Value: 958 mb at 53°N 145°W

Sensitivity Value: 974 mb at 53°N 145°W

Per Cent Change: 28% less deep relative to $\bar{P}$ = 1015 mb

Wind Field Variations near storm centre, decreases ~ 15 to 25 knots

5 to 10 knot increase out to about 600 km from storm centre

Maximum Local Wind-Sea Difference

Maximum Base Value: 10 m on day 03 hour 00 ΔH_s = -5 m (-50%)

Maximum Sensitivity Test: 5 m on day 03 hour 00 ΔH_s = -5 m (-100%)

Maximum Difference: 5 m on day 03 hour 00 min. base H_s = 8 m (-38%)
(very localized under the maximum winds)

Coastal Swell storm maxima to end of test run

	Base H_s (m)	Sensitivity H_s (m)	ΔH_s (m)	Difference
Tofino	1.3	0.5	-0.8	-62%
Queen Charlotte Sd	3.1	1.5	-1.6	-52%
N Queen Charlotte I	4.7	2.7	-2.0	-43%

Rate of Intensification

Occasionally storms that travel at typical rates along their trajectory will include a 12 to 24 hour segment during which the central low pressure falls by 1 mb/h or more. Such a high rate of intensification is called explosive deepening. In the last two years (since the fishing boat losses in November 1984), west coast storms with this character have received more attention from weather forecasters because it is difficult to predict which storms will deepen at these accelerated rates. In many cases, the explosive cyclogenesis rapidly transforms a mild weather system into a severe one.

Correct modelling of the rate of deepening is also important for storm hindcasting in that it affects both the shape (hence fetch) of the wind field and the duration of each wind pattern for up to a day preceding the storm peak. The results of one intensification rate sensitivity test are presented in Table 6.4.

Table 6.4
Summary of Sensitivity to Rate of Intensification

Base Value:	-0.6 mb/h from day 02 hour 06 to day 02 hour 18
Sensitivity Value:	-1.8 mb/h from day 02 hour 06 to day 02 hour 18
Per Cent Change:	200% increase in rate of deepening for the 12 hours preceding the storm peak
Wind Field Variations	none at the storm peak
	up to 25 knots weaker near the storm centre 12 hours before the storm peak

Maximum Local Wind-Sea Difference

Maximum Base Value:	10 m on day 03 hour 00 ΔH_s = 0 m (0%)
Maximum Sensitivity Test:	10 m on day 03 hour 00 ΔH_s = 0 m (0%)
Maximum Difference:	-5 m on day 02 hour 06 min. base H_s = 7 m (-71%)
	-5 m on day 02 hour 12 min. base H_s = 7 m (-71%) (very localized under the maximum winds)

Coastal Swell storm maxima to end of test run

	Base H_s (m)	Sensitivity H_s (m)	ΔH_s (m)	Difference
Tofino	1.3	0.7	-0.6	-46%
Queen Charlotte Sd	3.1	2.2	-0.9	-29%
N Queen Charlotte I	4.7	4.0	-0.7	-15%

6.1.2 Storm Trajectory

As clearly illustrated in Fig. 4.7, within the class of storms considered in this analysis, the northward leg of the storm trajectory can vary widely. The average path along 145°W can easily be deflected 5° of longitude closer to the coast, and this was the sensitivity case that was tested. The results are summarized in Table 6.5.

In the more general hindcasting context, this is a very important parameter. The results are sensitive to its specification and it is quite difficult to determine with certainty, especially for storms that are not well-mapped by satellite imagery. Those weather systems that cross the coast are likely to be more accurately tracked as they near the coast by the more dense and systematic land-based meteorological reporting network.

Table 6.5

Summary of Sensitivity to Storm Trajectory

Base Value:	northern trajectory along 145°W
Sensitivity Value:	northern trajectory along 140°W
Per Cent Change:	26% less distance to coast at 49°N
	42% less distance to coast at 55°N

Wind Field Variations   none in relation to the storm centre

along the coast, peak winds strengthen by ~5 knots on the south coast and ~10 knots on the north coast at day 02 hour 18

change in direction is negligible

Maximum Local Wind-Sea Difference

Maximum Base Value:	10 m on day 03 hour 00 $\Delta H_s = -4$ m (-40%)
Maximum Sensitivity Test:	10 m on day 03 hour 00 $\Delta H_s = +6$ m (60%)
Maximum Difference:	+6 m on day 03 hour 00 min. base $H_s = 3.5$ m (171%)
	-5 m on day 02 hour 18 min. base $H_s = 8$ m (-63%)
	(very localized under the maximum winds)

Coastal Swell   storm maxima to end of test run

	Base H_s (m)	Sensitivity H_s (m)	ΔH_s (m)	Difference
Tofino	1.3	3.3	2.0	154%
Queen Charlotte Sd	3.1	4.8	1.7	55%
N Queen Charlotte I	4.7	8.2*	3.5*	74%*
	4.7	5.8	1.1	23%

*due to local wind sea

6.1.3 Storm Advection Rate

The most significant change that can occur in the storm advection rate is associated with low pressure systems that stall (i.e. become stationary in space) without change in any other pressure characteristics. Typically stalls last 24 hours and occur somewhere in the northern Gulf of Alaska after the storm has peaked and begun to diminish in intensity. Table 6.6 summarizes the results of this sensitivity test.

Table 6.6
Summary of Sensitivity to Storm Advection Rate

Base Value:	37 km/h from 53°N to 59°N along 145°W
Sensitivity Value:	16 km/h from 53°N to 59°N along 145°W
Per Cent Change:	57% slower on average
Wind Field Variations	none in space except as a function of time after day 03 hour 12
Coastal winds	up to 5 knots stronger from Queen Charlotte Sound to northern Queen Charlotte Islands
Deep ocean	25 to 30 knots stronger due W of Queen Charlotte I except 10 to 35 knots weaker near storm centre 15 to 25 knots stronger due W of Queen Charlotte Sd 5 to 15 knots stronger due W of Vancouver Island more rapid direction change with longitude

Maximum Local Wind-Sea Difference

Maximum Base Value: 10 m on day 03 hour 00 ΔH_s = 0 m (0%)

Maximum Sensitivity Test:12.5 m on day 03 hour 12 ΔH_s = 6.2 m (50%)
(up to end of base)

Maximum Difference: 7 m on day 03 hour 12 min. base H_s = 3 m (233%)
(very localized under the maximum winds; this difference will increase as the stall continues)

Coastal Swell storm maxima to end of test run at 0312 (and 0412)

	Base H_s (m)	Sensitivity H_s (m)	ΔH_s (m)	Difference
Tofino	1.3 (3.8)	1.4 (3.9)	0.1 (0.1)	8% (3%)
Queen Charlotte Sd	3.1 (4.8)	3.0 (3.7)	-0.1 (-1.1)	-3% (-23%)
N Queen Charlotte I	4.7 (5.5)	4.4 (5.8)	-0.3 (0.3)	-6% (5%)

6.1.4 Comparison of Maximum Errors

Based on the sea-state differences noted in Tables 6.1 through 6.6 and encapsulated in Table 6.7, there are clear distinctions to be made on the relative importance of each sensitivity parameter. The one which causes the most sea-state change over the widest area is the storm trajectory. Differences in excess of 150% in both local wind-sea and swell resulted from a large (but not the maximum realizable) shift in the path of the central low pressure. Applying a linear scaling to per cent change as a function of distance, the trajectory must be correct to within 1° of longitude to reduce H_s errors to about 10%. This is a physical distance of about 70 km near $50^{\circ}N$, but corresponds to less than 1 cm at the scale of a meteorological surface analysis chart. It seems unrealistic, therefore, to expect this degree of accuracy, especially in historical surface pressure data.

Greater changes in H_s may be caused by extreme changes in the storm advection rate (i.e. by a stalled storm system), but these are restricted to local wind-sea under the stalled system and to any increased swell the evolves from this area.

The minimum central pressure was varied within virtually its historical limits. Intensifying $P_o(min)$ by 25% (-14 mb) created H_s increases of roughly the same percentage except in very localized pockets under the maximum winds. Reducing the intensification by 28% (+16 mb) generated sea-states that are about 50% lower. It is then reasonable to expect that a 5 mb over-intensification will not change H_s by more than 10%; however, the equivalent under-estimate of the depth of $P_o(min)$ can lead to underestimating H_s by about 20%. Errors of ± 5 mb are very possible over the deep ocean since $P_o(min)$ must be inferred from measurements from a reporting network consisting of a very few meteorological buoys, ships-of-opportunity, lighthouses and other land stations. It is most unlikely that any of these data sources will be close to a storm centre since ships' captains will try to avoid severe wind and wave conditions and the distribution of the remaining part of the network is so sparse.

Assuming that the minimum central pressure value is a given, the changes in the rate of intensification to that value can have at most two consequences. Since the wind-sea will respond to the local wind, the duration of a given wind speed and direction will be shorter for more rapidly deepening storms, and the resulting swell energy will be diminished. Significant pressure errors of this type would not normally arise unless surface pressure charts

Table 6.7

Maximum Sea-State Variability Attributable to Pressure Parameter Sensitivity Tests

Sensitivity Parameter	Local Wind-Sea Difference			Swell
	Max. From Base	Max. From Sensitivity	Max. ΔH_s	Max. ΔH_s*
Radial Extent (R)	-10%	-11%	-24%	0 to 23%
Minimum Central Pressure minimum P_0(min)	15%	36%	77%	26 to 31%
maximum P_0(min)	-50%	-100%	-38%	-43 to -62%
Rate of Intensification	n/a	n/a	-71%	-15 to -46%
Trajectory	-40%	60%	-63 to 171%	55 to 154%
Storm Advection Rate	n/a	50%	233%	-23 to 8%

n/a: no applicable comparison   * independent of time

are very inaccurate or unless they are only available at widely spaced intervals during storm development.

The storm size, according to the definition used in this study, has the least effect on the hindcast results. Small adjustments in the radius (±25%) will have an impact of not more than ±10% in the wave field maxima, although greater per cent changes are possible in low level coastal swell energy.

6.2 Conclusions

6.2.1 The Meteorological Perspective

Two conclusions are apparent from the results of this study:

(1) With the advent of routine satellite images of cloud formations, it is expected that significant improvements in the accuracy of storm trajectory positioning will have occurred. Since this is a most sensitive parameter for wave modelling, better wave hindcasting results, on average, should be found when satellite data are used in preparing the surface pressure charts.

(2) Any degradation in the surface pressure monitoring network at sea (especially decommissioning of weather ships, poor maintenance or removal of meteorological buoys which normally provide the most reliable guidance to meteorologists) will tend to result in less accurate pressure field specification.

6.2.2 Wave Hindcasting Perspective

This study demonstrates that ADWAVE (and presumeably other models that embody the same elements of the physics of wave generation) produces sea-states that are locally in balance with the wind in the sense that the H_s field under the active storm centre and the strongest winds is largely independent of the preceding storm history. As a result, peak sea-states in the deep open ocean will not depend strongly on any arbitrary wind field errors that precede or follow the storm peak. The wave field's "memory" of a wind field error will have two forms:

(1) Through the temporal interpolation from (say) 6-hourly wind maps (corresponding to available surface pressure charts) to the wave model time step, an error in a single wind field influences almost a full 12 hours of wave hindcasting.

(2) Swell energy that propagates freely at off-wind angles will perpetuate any error that occurred in its generation.

Nested wave model grids present an added dimension of complexity to an assessment of the effects of wind errors. In such a case, the nested grid is linked to the coarser surrounding one through the supply of boundary spectra from the coarse run to the finer nested one.

In deep water coarse grid hindcast modelling, the boundary conditions are invariably set to zero energy flux. Usually the open water boundaries are sufficiently well-removed from points of interest that the approximation is quite adequate unless significant swell energy can propagate into the model domain from remote storm systems that are not being modelled. On the other hand, nested grids are usually of small overall physical dimensions and in these cases boundary conditions will often be as important, and at times more important than the local wind forcing.

In shallow water, where nested grids are usually applied, refraction, shoaling and bottom friction and/or percolation are additional source/sink terms that are excluded from deep water applications. Refraction, in particular, depends on correct boundary specification of the partition of the total energy (H_s) as a function of period (frequency) and direction.

6.2.3 Engineering Applications Perspective

In terms of extreme value analysis of the long-term wave climate for coastal design applications, the importance of swell can be largely discounted since the annual extreme event (for example) will almost certainly be a local wind-sea dominated sea-state at its peak. In that case, the pressure parameters of ranked importance will be

(1) the trajectory of P_o and hence the location of $P_o(min)$,

(2) the value of $P_o(min)$, and

(3) the advection rate of P_o.

The rate of deepening is expected to be much less important so long as $P_o(min)$ is as correct as possible. Thus, with due consideration of the pitfalls, with reanalysis of the key surface pressure fields, and with incorporation of as much measured wind data as possible in a kinematic analysis, it is quite feasible to hindcast a set of extreme wave events using a spectral model such as ADWAVE to within engineering standards. Because the data requirements are relatively small, the demand for man-time and computer resources can be met within the economic constraints of most major projects.

In many cases climatological statistics of wind-sea and of swell rather than, or in addition to, long return period extreme values are required. These situations include planning, construction and operation of fixed coastal installations such as harbours, exposed berthing facilities and breakwaters; and many aspects of offshore hydrocarbon exploitation such as pipeline installation, tanker and other tender vessel routing and operation, certain phases of concrete gravity-base production platform construction, rig towing, and dredging for construction and maintenance of artificial islands. In each case the efficiency of planning and executing each of these activities is enhanced by informed understanding of the normal wave climate: joint distribution of height, period and direction, persistence statistics and short-term extreme value expectations. Unless many sites are involved or decision-making time-frames are very short, collection of wave measurements will be preferrable to wave hindcasting from both cost and accuracy points of view. For example, one year of wind and wave hindcasting would require many man-months to prepare wind input and about 1500 hours of computer CPU time (using a very fast micro-computer as was done in this study) to generate the digital wind fields, to prepare a deep water wave hindcast and to examine some of the results. A subsequent shallow water nested application would require at least as much computer time as well.

Therefore, considering only the number of sources of significant errors that may be introduced into digital wind fields, it does not seem prudent to attempt hindcasting site-specific nearshore wave climatological data until wind data can be generated with much greater reliability. In this respect, the most promising development, the realization of which is still in the future, is the ability to objectively incorporate real-time remotely-sensed (satellite) wind data into the numerical analysis and prognosis procedures of the national weather service. In the next decade or so, when there are enough satellites with the appropriate scatterometer or passive microwave sensors, it should be possible to archive wind data instead of surface pressures, thereby gradually to remove the reliance on pressure data for wave hindcasting and to begin the modelling process with actual data-based digital surface winds.

7.0 REFERENCES

Bouws, E., H. Günther, W. Rosenthal and C.L. Vincent, 1985. Similarity of the Wind Spectrum in Finite Depth Water. J. Geophys. Res., 90(C1), 975-986.

Cardone, V.J., W.J. Pierson and E.G. Ward, 1975. Hindcasting the Directional Spectra of Hurricane Generated Waves. Offshore Technology Conference, Paper OTC 2332.

Cardone, V.J., A.J. Broccoli, C.V. Greenwood and J.A. Greenwood, 1980. Error Characteristics of Extratropical-Storm Wind Fields Specified From Historical Data. J. Petrol. Tech., 8, 872-880.

Clancy, R.M., J.E. Kaitala, and L.F. Zambresky, 1986. The Fleet Numerical Oceanography Center Global Spectral Ocean Wave Model. Bull. Am. Meteor. Soc., 67(5), 498-512.

Coté, L.J., J.O. Davis, W. Marks, R.J. McGough, E. Mehr, W.J. Pierson, J.F. Ropek, G. Stephenson and R.C. Vetter, 1960. The Directional Spectrum of a Wind Generated Sea as Determined From Data Obtained by the Stereo Wave Observation Project. Meteorological Papers, New York University, College of Engineering, 2(6).

Delage, Y., 1985. Surface Turbulent Flux Formulation in Stable Conditions for Atmospheric Models. Mon. Wea. Rev., 113.

Det norske Veritas, 1982. Rules for the Design and Inspection of Offshore Structures, Appendix A: Environmental Conditions. Oslo, Reprint 1982, A11.

Dobrocky Seatech, 1986. Technical report prepared for the Environmental Studies Revolving Fund, Ottawa.

Golding, B., 1983. A Wave Prediction System for Real-Time Sea State Forecasting. Quart. J. R. Met. Soc., 109, 393-416.

Garratt, J.R., 1977. Review of Drag Coefficients Over Oceans and Continents. Mon. Wea. Rev., 105, 915-929.

Günther, H., W. Rosenthal and K. Richter, 1979a. Application of the Parametrical Surface Wave Prediction Model to Rapidly Varying Wind Fields During JONSWAP 1973. J. Geophys. Res., 84(C8), 4855-4864.

Günther, H., W. Rosenthal, T.J. Weare, B.A. Worthington, K. Hasselmann and J.A. Ewing, 1979b. A Hybrid Parametrical Wave Prediction Model. J. Geophys. Res., 84(C9), 5727-5737.

Hasselmann, K., T.P. Barnett, E. Bouws, H. Carlson, D.E. Cartwright, K. Enke, J.A. Ewing, H. Gienapp, D.E. Hasselmann, P. Kruseman, A. Meerburg, P. Mueller, D.J. Olbers, K. Richter, W. Sell and H. Walden, 1973. Measurements of Wind-Wave Growth and Swell Decay During the Joint North Sea Wave Project (JONSWAP). Deutsche Hydrographische Zeitschrift, Reihe A., Nr. 12.

Hasselmann, K., D.B. Ross, P. Mueller and W. Sell, 1976. A Parametric Wave Prediction Model. J. Phys. Oceanogr., 6, 200-228.

Hasselmann, D.E., M. Dunckel and J.A. Ewing, 1980. Directional Wave Spectra Observed During JONSWAP 1973. J. Phys. Oceanogr., 10(8), 1264-1280.

Hodgins, D.O., P.H. LeBlond, D.S. Dunbar and C.T. Niwinski, 1985. A Wave Climate Study of The Northern British Columbia Coast, Volume II. Technical report prepared for Fisheries and Oceans, Canada by Seaconsult Marine Research Ltd., Vancouver.

Hodgins, D.O. and S. Nikleva, 1986. On the Impact of New Observing Sites on Severe Sea State Warnings for the B.C. Coast. Unpublished technical report prepared for Fisheries & Oceans Canada by Seaconsult Marine Research Ltd., Vancouver.

Hodgins, D.O. and S. Hodgins, 1986. An Evaluation of Wave Forecasting Models and Forecast Wind Fields in the Canadian Context. Draft report prepared for the Environmental Studies Revolving Fund, Ottawa.

Hodgins, D.O., C.T. Niwinski and D.T. Resio, 1986. Comparison and Validation of Two Shallow-Water Spectral Wave Models. Draft report prepared for The Environmental Studies Revolving Funds, Ottawa by Seaconsult Marine Research Ltd.

Hsu, S.A., 1986. A Mechanism for the Increase of Wind Stress (Drag) Coefficient With Wind Speed Over Water Surfaces: A Parametric Model. J. Phys. Oceanogr., 16(1), 144-150.

Janssen, P.A.E.M., G.J. Komen and W.J.P. de Voogt, 1984. An Operational Coupled Hybrid Wave Prediction Model. J. Geophys. Res., 89(C3), 3635-3654.

Kitaigorodskii, S.A., 1983. On the Theory of the Equilibrium Range in the Spectrum of Wind-Generated Gravity Waves. J. Phys. Oceanogr., 13(5), 816-827.

Komen, G.J., 1984. The Wave Modelling (WAM) Project: Proposal for the Development and Operational Implementation of a Third Generation Ocean Wave Model. First draft issued by Chairman WAM Group, De Bilt, The Netherlands.

Large, W.G. and S. Pond, 1981. Open Ocean Momentum Flux Measurements in Moderate to Strong Winds. J. Phys. Oceanogr., 11(3), 324-336.

LeBlond, P.H., 1984. Final Report of the Investigation on the Storm of October 11-12, 1984 on the West Coast of Vancouver Island. Ministry of the Environment, Victoria, B.C.

Lewis, C.J. and M.D. Moran, 1985. Severe Storms Off Canada's West Coast: A Catalogue Summary for the Period 1957 to 1983. Canadian Climate Centre Unpublished Report No. 85-7.

Longuet-Higgins, M.S., D.E. Cartwright and N.D. Smith, 1961. Observations of the Directional Spectrum of Sea Waves Using the Motions of a Floating Buoy, in Ocean Wave Spectra. Prentice-Hall, Englewood Cliffs, 111-132.

MacLaren Plansearch, 1985. Evaluation of the Spectral Ocean Wave Model (SOWM) for Supporting Real-Time Forecasting in the Canadian East Coast Offshore. Unpublished technical report prepared for the Meteorological Services Research Branch, Atmospheric Environment Service, Downsview, Ont.

MEDS, 1984. Historical Wave Measuring Stations, Station Locations Summary. Dept. of Fisheries and Oceans, Marine Environmental Data Service. Updated 28-09-84.

Pearson, F., 1984. Map Projection Methods. Sigma Scientific, Inc., Blacksburg, Virginia.

Pierson, W.J. and L. Moskowitz, 1964. A Proposed Spectral Form for Fully-Developed Wind Sea Based on the Similarity Theory of S.A. Kitaigorodskii. J. Geophys. Res., 69, 5181-5190.

Pierson, W.J., L.J. Tick and L. Baer, 1966. Computer Based Procedures for Preparing Global Wave Forecasts and Wind Field Analyses Capable of Using Wave Data Obtained by a Spacecraft. Sixth Naval Hydrodynamics Symposium, Office of Naval Research, Washington, D.C., 499-532.

Resio, D.T., 1981. The Estimation of Wind-Wave Generation in a Discrete Spectra Model. J. Phys. Oceanogr., 11, 510-525.

Resio, D.T., 1982. Wave Prediction in Shallow Water. Proc. 14th Annual Offshore Technology Conference, OTC 4242, Vol. 2, 147-152.

Resio, D.T., 1985. Wave Transformations Related to Nonlinear Fluxes. Manuscript submitted to ASCE J. of Waterway, Port, Coastal and Ocean Engineering.

Resio, D.T. and C. L. Vincent, 1979. A Comparison of Various Numerical Wave Prediction Techniques. Proc. 11th Annual Offshore Technology Conference, OTC 3642, 2471-2478.

St. Denis, M. and W.J. Pierson, 1953. On the Motion of Ships in Confused Seas. Trans. SNAME, 61, 280-357.

Sarpkaya, T. and M. Isaacson, 1981. Mechanics of Wave Forces on Offshore Structures. Van Nostrand Reinhold Co., New York.

Seaconsult, 1986a. Unpublished report prepared for Mobil Oil Canada, Ltd.

Seaconsult, 1986b. Unpublished report prepared for Esso Resources Canada Ltd.

Seakem, 1985. A Wave Climate Study of the Northern British Columbia Coast. Technical report prepared for Marine Environmental Data Services Branch, Department of Fisheries and Oceans, Ottawa by Seakem Oceanography Ltd., Sidney, B.C.

U.S. Army, 1977. Shore Protection Manual, Vol. I. U.S. Government Printing Office, Washington.

Yamada, T. 1976. On the Similarity Functions A, B, and C of the Planetary Boundary Layer. J. Atmos. Sci., 23, 781-793.